KUNGL
VETENSKAP
OCH
KONST
TEKNISKA
HÖGSKOLAN

Partial Discharges Studied with Variable Frequency of the Applied Voltage

Hans Edin

Partial Discharges Studied with Variable Frequency of the Applied Voltage

Hans Edin

Abstract

This thesis concerns partial discharge (PD) diagnostics with variable frequency of applied voltage in the frequency range 1 mHz - 400 Hz. The exploration of a new type of spectroscopy that combines partial discharge analysis and dielectric response is demonstrated. A question addressed is if and how the PD activity varies with the frequency of the applied voltage. The nature of an existing frequency dependence could be useful in the classification of different defects and to judge the degree of progressive ageing.

A Variable-Frequency Phase Resolved Partial Discharge Analysis (VF-PRPDA) technique is developed for the applied voltage frequency range 1 mHz - 400 Hz. The VF-PRPDA technique is combined with a system for high voltage dielectric spectroscopy that allows simultaneous measurements. The VF-PRPDA technique is used for studying the frequency dependence of PD. The PD activity is for example measured by integrated measures like total charge per cycle and total number of discharges per cycle. Statistical measures like mean, standard deviation, skewness, kurtosis etc. are applied to measure the frequency dependence of the phase distributions.
High voltage dielectric spectroscopy is supplemented with harmonic analysis for studying non-linear dielectric response currents.

The VF-PRPDA technique is demonstrated on defined objects like point-plane gaps and artificial voids, but also on an insulated stator bar and a paper insulated cable. Surface discharges on insulating surfaces are studied in an environment with a controlled relative humidity and temperature. The adsorption of moisture on the insulating surface alters the surface conductivity of the surface and the frequency dependence of the PD activity.
The influence of temperature upon the PD activity is studied for an oil paper insulated cable.
The results of the measurements show that the partial discharge activity in general is frequency dependent over the frequency range 1 mHz - 400 Hz. The reasons behind the frequency dependence are linked to surface- and bulk- conducting mechanisms, frequency dependent field distributions and statistical effects of the supply of start electrons.
An algorithm is developed that relates the phase resolved PD current measured with the PRPDA technique to the non-linear current measured with dielectric spectroscopy. The algorithm is experimentally verified by simultaneous measurements of PRPDA and dielectric spectroscopy on defined objects. The results explain the contribution of PD to the apparent capacitance and loss. Moreover, the harmonics of the fundamental current component yield information about, for example, polarity dependent discharge sources.

Key words: diagnostic methods, partial discharges, phase resolved, variable frequency, dielectric spectroscopy, dielectric response, harmonics, insulation

Acknowledgement

I thank Yngve Eriksson and Jan Olov Brännvall for making many things in the workshop.

The financial support from ELEKTRA is gratefully acknowledged.

To my mother and father and the rest of my family I express my deepest thanks and love for the support you have given me during these 30 years.

Finally, but not least, I express my deepest love and gratitude to my wife Ulrika for your patience and understanding. To my daughter Rebecka: you are not something partial - you are complete.

Hans Edin
Stockholm 2001

List of symbols

Symbol name	Symbol	Unit
Angular frequency	ω	$[\text{rad}\cdot\text{s}^{-1}]$
Average phase resolved PD current	$\overline{q}(\varphi)$	$[\text{C}]$
Capacitance, in general	C	$[\text{F}]$
Capacitance, geometrical	C_0	$[\text{F}]$
Capacitance, complex, general	$\tilde{C}, C', C''$	$[\text{F}]$
Capacitance, apparent	C'_{App}, C''_{App}	$[\text{F}]$
Capacitance, PD contribution	$\Delta C'_{PD}, \Delta C''_{PD}$	$[\text{F}]$
Capacitance, linear part	C'_{Lin}, C''_{Lin}	$[\text{F}]$
Capacitance of test object	C_T	$[\text{F}]$
Capacitance of coupling capacitor	C_K	$[\text{F}]$
Capacitance of balancing capacitor	C_B	$[\text{F}]$
Capacitance, feedback	C_{FB}	$[\text{F}]$
Capacitance, calibration	C_{Cal}	$[\text{F}]$
Capacitance, in detection impedance	C_{Det}	$[\text{F}]$
Capacitance, in a-b-c model	C_a, C_b, C_c	$[\text{F}]$
Charge, in general	q, q_i, q_j, q_m, Q	$[\text{C}]$
Charge, average discharge magnitude	$\overline{Q}$	$[\text{C}]$
Charge, average negative discharge magnitude	$\overline{Q}^-$	$[\text{C}]$
Charge, average positive discharge magnitude	$\overline{Q}^+$	$[\text{C}]$
Charge, calibration	q_{Cal}	$[\text{C}]$
Charge, detected	q_{Det}	$[\text{C}]$
Charge, maximum discharge magnitude	Q_{Max}	$[\text{C}]$
Charge, maximum negative discharge magnitude	Q_{Max}^-	$[\text{C}]$
Charge, maximum positive discharge magnitude	Q_{Max}^+	$[\text{C}]$
Charge, total per cycle	Q_{Tot}	$[\text{C}]$
Charge, total negative per cycle	Q_{Tot}^-	$[\text{C}]$
Charge, total positive per cycle	Q_{Tot}^+	$[\text{C}]$
Conductance, DC	G_{DC}	$[\Omega^{-1}]$
Conductivity, DC, bulk	σ_{DC}	$[\Omega^{-1}\text{m}^{-1}]$
Conductivity, surface	σ_s	$[\Omega^{-1}]$
Current, in general	i, I	$[\text{A}]$
Current, dielectric response	i_{DR}	$[\text{A}]$
Current, linear with voltage	i_{Lin}	$[\text{A}]$
Current, partial discharge	i_{PD}	$[\text{A}]$

Dirac's delta function	$\delta(t)$	$[s^{-1}]$
Distance	d	[m]
Distribution,*		
charge per cycle vs. phase	$H_{qs}(\varphi) = \overline{q}(\varphi)$	[C]
maximum charge vs. phase	$H_{qm}(\varphi)$	[C]
mean charge vs. phase	$H_{qn}(\varphi)$	[C]
number of discharges per cycle vs. phase	$H_n(\varphi)$	[-]
number of neg. dischg. vs. charge magnitude	$N_q^-(q)$	[-]
number of pos. dischg. vs. charge magnitude	$N_q^+(q)$	[-]
Distribution, normalised phase	$h(\varphi)$	[-]
Electric field, in general	E	[V/m]
Electric field in gas filled cavity	E_g	[V/m]
Electric field in bulk	E_b	[V/m]
Field enhancement factor	f_E	[-]
Fourier coefficients	a_n, b_n, c_n	[]
Fourier coefficients from PD pattern	a_n^{PDP}, b_n^{PDP}	[]
Frequency	f	[Hz]
Gain	G	[-]
Harmonic content	HC_n	[-]
Impedance, detection	Z_{Det}	$[\Omega]$
Impedance, filter	Z_{Filt}	$[\Omega]$
Indices	i, j, k, m, n, p	[-]
Inductance, in general	L	[H]
Inductance, in detection impedance	L_{Det}	[H]
Inverter gain	k_{Inv}	[-]
Kurtosis	Ku	[-]
Legendre coefficients	c_n	[]
Legendre polynomial	$P_n(x)$	[-]
Loss angle	δ	[Degrees, rad]
Loss tangent	$\tan \delta$	[-]
Mean value	m_1	[Degrees, rad]
Moments, central of order k	μ_k	$[Degrees^k, rad^k]$

Moments of harmonic base functions	α_{kn}, β_{kn}	[Degrees^k, rad^k]
Moments, standard of order k	m_k	[Degrees^k, rad^k]
Number of applied voltage periods	N_P	[-]
Number of discharges per cycle	N_{Tot}	[-]
Number of negative discharges per cycle	N_{Tot}^-	[-]
Number of positive discharges per cycle	N_{Tot}^+	[-]
Partial discharge pattern	$n(\varphi_j, q_m)$	[-]
Permittivity of vacuum ($8.854 \cdot 10^{-12}$)	ε_0	[Fm^{-1}]
Permittivity, complex, general	$\widetilde{\varepsilon}, \Delta\varepsilon', \varepsilon', \varepsilon''$	[Fm^{-1}]
Permittivity, complex, relative	$\widetilde{\varepsilon}_r, \Delta\varepsilon_r', \varepsilon_r', \varepsilon_r''$	[-]
Permittivity, apparent, relative	$\Delta\varepsilon_{App}', \Delta\varepsilon_{App}''$	[-]
Permittivity, PD contribution, relative	$\Delta\varepsilon_{PD}', \Delta\varepsilon_{PD}''$	[-]
Permittivity, complex, relative, of bulk material	$\varepsilon_{Bulk}', \varepsilon_{Bulk}''$	[-]
Phase angle	$\varphi, \varphi_i, \varphi_j$	[Degrees, rad]
Phase lag	$\Delta\varphi_{lag}$	[Degrees, rad]
Power loss	P	[W]
Power, reactive	Q	[VAr]
Pressure	p	[bar]
Resistance, in general	R	[Ω]
Resistance, in a-b-c model	R_a, R_b, R_c	[Ω]
Resistance, in detection impedance	R_{Det}	[Ω]
Resistance, protection	R_P	[Ω]
Resistance, surface	$R_{\square}$	[Ω]
Skewness	Sk	[-]
Standard deviation	σ_{std}	[Degrees, rad]
Temperature	T	[°C]
Thickness of gas layer	d_g	[m]
Thickness of bulk layer	d_b	[m]
Time, in general	t, t_i, t_j	[s]
Time, inception delay	Δt_{inc}	[s]
Time lag	Δt_{lag}	[s]
Time, period	T	[s]
Time, recover	τ_{rec}	[s]
Variance	μ_2	[Degrees^2, rad^2]

Voltage, in general	V	[V]
Voltage, applied amplitude	V_0	[V]
Voltage, partial discharge inception	V_{inc}	[V]
Voltage, inverter output	V_{Inv}	[V]
Voltage, calibration step	ΔV_{Cal}	[V]
Voltage, charging	V_{Chg}	[V]
Voltage, across discharge gap	V_g	[V]
Voltage, breakdown	V_b	[V]

*) Phase distributions for positive and negative voltage half-cycle have superscript $V+$, and $V-$ respectively, e.g. $H_{qs}^{V+}(\varphi)$ for charge per cycle vs. phase under positive voltage polarity. Distributions of positive and negative discharge polarity have superscript $PD+$, and $PD-$ respectively, e.g. $H_n^{PD-}(\varphi)$ for number of pulses per cycle vs. phase with negative discharge polarity. The moments derived of each distribution are supplied with superscripts after the same convention.

List of acronyms and abbreviations

ABB	ASEA Brown Boveri
AC	Alternating Current
ADC	Analog to Digital Converter
ASEA	Allmänna Svenska Elektriska Aktiebolaget
CBM	CaBle Model
DAP	Data Acquisition Processor
DC	Direct Current
DFT	Discrete Fourier Transform
DS	Dielectric Spectroscopy
DTU	Technical University of Denmark
GUI	Graphical User Interface
HF	High Frequency
HLQ	Harmonic Loss Quantity
HV	High Voltage
ICM	Insulation Condition Monitoring
IDA	Insulation DiAgnostics
IEC	International Electrotechnical Commission
IV	Insulating Vulcanized
KTH	Kungl Tekniska Högskolan (Royal Institute of Technology)
LF	Low Frequency
LFD	Low Frequency Dispersion
LLD	Low Level Discrimination
PA	Poly-Amide
PD	Partial Discharge
PE	Poly-Ethylene
PET	Poly-Ethylene-Terephthalate
PI	Poly-Imide
PILC	Paper InsuLated Cable
PP	Poly-Propylene
PRPD	Phase Resolved Partial Discharge
PRPDA	Phase Resolved Partial Discharge Analysis
PSA	Pulse Sequence Analysis
RH	Relative Humidity
SMPD	Swarming Micro Partial Discharges
VF-PRPDA	Variable Frequency PRPDA
XLPE	Cross(X)-Linked Poly-Ethylene

x

Contents

1 Introduction

1.1 Background

The electrical insulation is one of the most important parts in high-voltage components and its qualities determine the reliability of the whole equipment. The electrical insulation system is designed to sustain the electrical stress caused by the applied voltage, the temperature variations, the mechanical stress, etc. However, even if the insulation system of course fulfils all the required tests before installation and use, it may not maintain the same qualities during the many years it is set to operate. There may be built-in imperfections from the manufacturing process that has not been observed or that was not indicated during the commissioning tests, or the insulation may be deteriorated by unexpected environmental conditions or occasions.

Diagnostic methods are commonly applied in the area of maintenance of power apparatus. Frequent questions raised by the utilities concern the remaining life of a particular equipment and the risk of failure within a certain time. The needs for a condition based maintenance strategy is of great importance in, for example, replacing old cables in a cable network or rewinding the stator in a large electric machine. The driving force is to keep a reliable equipment at a low cost as possible.

The field of non-destructive diagnostic for high-voltage electrical insulation was long confined to methods such as dielectric loss-tangent measurements at power frequency and measurements of partial discharge (PD) activity [1]. However, the progress in electronics and computerised measurement equipment has rendered many new methods, some of which have become established and other are still questionable. However, two modern diagnostic methods that have become such established diagnostic tools that they are at least briefly covered in textbooks on high-voltage engineering [1] are dielectric spectroscopy and phase resolved partial discharge analysis (PRPDA). In this project, both dielectric spectroscopy and PRPDA have been used with variable frequencies to investigate partial discharges.

The field of diagnostics started 1992 at KTH with a project to diagnose Cross-Linked Polyethylene Cables that suffered by water-trees [2, 3, 4]. The method applied was High-Voltage Dielectric Spectroscopy [5] performed in the low-frequency range, i.e. from 1 mHz - 1000 Hz. The method of dielectric spectroscopy has also been applied on oil-paper insulated high-voltage equipment such as power transformers [6] and oil impregnated paper cables [7]. The main aspect to apply dielectric spectroscopy on oil impregnated paper insulation is to measure the content of moisture within the paper, which is related to the quality of the paper-insulation and an assessment of the degradation process. The author made a contribution to this field in a master thesis [8].

In 1996 the field of diagnostics at the department was extended to also include diagnostics of electrical insulation that was infested by partial discharges (PD). PDs are localised discharges that only partially over-bridge the region of high- and low-voltage. PD appears

in regions that are over-stressed or have a lower local breakdown-strength than the main insulation. Examples of common PD-sources are: voids, cavities, delaminations, electrical trees, etc. embedded in solid insulation; surface discharges along insulating surfaces that are tangentially over-stressed; and corona discharges from protrusions in gases or liquids.

In this project, the combination of variable frequency and high-voltage diagnostics was applied for insulation systems that suffered by PD. In particular the behaviour of the PD-activity at frequencies below power frequency was unexplored and had become of practical interest in the field of applicability of low-frequency diagnostic methods.

Two measuring methods were of interest: first an extension of an existing measurement system for phase resolved acquisition of PD to cover the frequency range 1 mHz - 400 Hz and secondly to investigate the behaviour of the PD-current with dielectric spectroscopy, extended to also include analysis of the harmonics caused by the non-linear PD-current.

1.2   Motivation and aim for this study

1.2.1   Variable frequency PD analysis

The insulation of a high-voltage equipment is in principle a capacitance between the high- and low-voltage side of the equipment, e.g. the insulation between the high-voltage conductor and the screen of a high-voltage cable. The reactive power, Q needed to generate a test voltage of amplitude, V_0 and angular frequency ω on a capacitive object with capacitance $C(\omega)$ is given by $Q \approx \omega C(\omega) V_0^2$. For example, to generate 10 kV at 50 Hz on a cable with a capacitance of 1 μF requires 31.4 kVAr, but at 5 mHz only 31.4 VAr. From this behaviour it becomes clear that a decreased frequency yields a similar reduction in power and size of the supply equipment. The interest for low-frequency test-methods goes back to the early 1960s [9], but has rendered an increased interest during the last decades [10].

The applicability of low-frequency methods on PD-infested insulation raises the general question: does an investigation performed at a frequency that differ from the normal operating frequency yield results of relevance, since the actual stress and other conditions may be different at different frequencies? If this question can be answered with yes, then one may conclude that quality assessments can be performed by measurements performed at a frequency different than the power frequency. On the other hand, if the answer is no, then one may make use of the information that are given by the frequency dependence.

Furthermore, the frequency dependence of the PD-activity may be used as an extra dimension for classification of different discharge sources. Discharge sources that have similar PD-patterns at power frequency may have different patterns at other frequencies.

The frequency dependence of PD could be used as a probe for local dielectric properties like surface conduction. An increased surface conductivity due to progressive PD-activity is commonly reported [11, 12]. This increased surface conductivity is a consequence of the by-products caused by the deterioration due to the PDs. Surface conductivities as well as

bulk conductivities have a stronger influence on, for example, the electric field distributions at low frequency than at higher frequencies [9]. Hence, in the long-term behaviour of PD it might be possible to resolve the ageing status by measuring the frequency dependence of the PD-activity.

The measurement and analysis method adopted for study the frequency dependence of partial discharges in the frequency range 1 mHz - 400 Hz was Phase Resolved Partial Discharge Analysis (PRPDA), i.e. a system that acquires and store single discharge magnitudes with respect to the phase of the applied voltage. The commercial ICM system [13] existed for the frequency range 30 Hz - 400 Hz, but was modified to also cover lower frequencies.

The purpose was to apply the Variable Frequency-PRPDA (VF-PRPDA) technique to different PD-infested objects for investigating the frequency dependence of the PD-activity. Some canonical objects like point-plane gap and different cavities were investigated. Band-gaps were deliberately introduced between layers of tapes to cause partial discharges. An old asphalt/mica machine insulation was investigated and showed a non-trivial frequency dependence. Surface discharges were extensively investigated with VF-PRPDA and by the adsorption of moisture on the surface in order to investigate the influence of the surface conductivity. A paper insulated cable (PILC) was studied and the influence of the temperature on the PD-activity was investigated.

1.2.2   Simultaneous measurement of PD and Dielectric Spectroscopy

A common method used for diagnosis of PD infested insulation systems is to measure the voltage dependence of the dielectric loss-tangent, tan-δ and the capacitance. An increase in the loss-tangent at a certain voltage ('tip-up') is often accepted as the inception of partial discharges. The severity of the PD-activity is then related to the inception voltage in relation to the nominal voltage and to the degree of the tip-up. However, the loss-tangent and capacitance measurement technique yields an integrated measure of the partial discharge current compared to the PRPDA technique where the single discharge magnitudes are detected.

Dielectric spectroscopy is the technique for measuring the complex capacitance, or the complex permittivity if the geometrical capacitance is known, of the insulation for a range of frequencies [5]. The loss-tangent is the ratio of the imaginary part to the real part of the complex capacitance.

The non-linear current of partial discharges has been shown to contribute both to the real- and imaginary-part of the complex capacitance [14], a contribution that depends on the PD-magnitudes and the phase of occurrence.

The hypothesis was that the current of partial discharges that was measured with the PRPDA system in principle was the same current as measured with dielectric spectroscopy, but interpreted in two different ways, and the purpose was to show that these two approaches were compatible. An algorithm was developed that related the PD-current measured with PRPDA to the non-linear part of the complex capacitance measured with

dielectric spectroscopy. In order to verify the relation it was required to construct a system that allowed simultaneous measurement of PRPDA and dielectric spectroscopy over the frequency range 1 mHz - 400 Hz. Simultaneous measurement is of particular importance if the PD-activity fluctuates in time.

A complete description of the non-linear PD-current requires that harmonics of the fundamental frequency are included in the dielectric spectroscopy. These harmonics can be used to illuminate the finer details of the phase resolved PD-current as could be obtained with the PRPDA system. The harmonics in the dielectric spectroscopy current were equally well achieved from the PRPDA acquired data.

The similarity of the two methods was demonstrated on artificial cavities and voids, but also applied to a paper insulated cable (PILC).

Furthermore, dielectric spectroscopy supply much of the information about the insulation that may be required to understand the frequency dependence of the PD-activity, e.g. the frequency dependence of the permittivity surrounding any voids embedded in solid dielectrics, and any bulk-conductivity that could influence the recharging of the voids at low frequencies.

1.3   Outline of the thesis

This thesis is composed of the eight publications listed in section 1.5 and the following chapters, which provide further analysis and complementary information of this subject.

Chapter 1 gives a background to the project and the subject as a whole with particular emphasis on the aim of this thesis. Further, it gives an outline of the thesis, i.e. a 'reading instruction'. It also contains a list of publications and the degree of responsibility the author has in each publication.

A review of the research previously performed on partial discharges at variable frequency below 50 Hz is given in Chapter 2. It also contains a brief review of previous work on relating the partial discharges to integrated measures like loss-tangent and capacitance 'tip-up', that can be achieved with bridge-techniques or dielectric spectroscopy.

Chapter 3 contains a brief description of common partial discharge sources and how their appearance can be recognised with a phase resolved detection technique. It is discussed how different mechanisms like initial electron statistics, frequency dispersion in bulk permittivities, bulk- and surface- conduction, etc., will force the partial discharge activity to become frequency dependent.

Chapter 4 gives the theory that has been derived for the relation between the phase resolved partial discharge current and the current measured with dielectric spectroscopy. It is further described how the harmonics within the dielectric response current can be used either directly for a re-synthesisation of the average PD-current, or as a direct measure of symmetry or anti-symmetry between different polarities of the phase resolved PD-current.

Different measures of phase location, spread, skewness, etc. of the phase resolved PD-current are defined in Chapter 5. The measures used are the statistical moments or operators like mean, standard deviation, skewness, etc. The phase-distributions on which the statistical operators are applied are formed by all discharges of a certain polarity. This formation is new and is to prefer instead of the common method to form the distribution by breaking with respect to applied voltage polarity.

In Chapter 6 the measuring systems are described. It is described how an existing system for phase resolved PD measurements are modified to be used in the applied voltage frequency range 1 mHz - 400 Hz. Furthermore, the system developed for simultaneous measurements of dielectric spectroscopy with harmonic analysis and PRPDA (or dielectric spectroscopy only) is described. The simultaneous system is also documented in paper VIII.

The analysis programs designed to analyse the acquired data are described in Chapter 7. The programs are designed as Graphical User Interfaces in MATLAB®. Two programs have been developed; one for investigating the acquired phase resolved partial discharge patterns and another for analysing the acquired dielectric spectroscopy data.

The obtained experimental methods have been applied on well-defined samples like artificial voids and sharp points, and on commercial electrical insulation. The well-defined samples have been used in investigating the principle relations between PRPDA and dielectric spectroscopy.

Chapter 8 contains results from measurements on a 'cable-model', i.e. a cylindrical structure of PET tapes wrapped around a copper tube with band-gaps deliberately introduced that serves as a source for partial discharges.

In Chapter 9, an old asphalt/mica insulated stator-bar is studied. The results showed a similar behaviour as the cable-model, this indicated that delaminations within the insulation caused partial discharges. The frequency dependence of the stator-bar showed a non-trivial behaviour: a statistical effect increased the total charge per cycle when the frequency was reduced from 100 Hz to 10 Hz. For frequencies below 1 Hz a monotonous decay of the total charge per cycle indicated that the surface conduction around the cavities decreased the field within the cavity.

An extensive work has been spent on investigating the influence of surface conductivity on the frequency dependence of surface discharges. The results from these investigations are presented in Chapter 10 and Paper VII. The surface discharge experiments were performed in a controlled atmosphere and the surface conduction was altered by the adsorption and desorption of moisture from the ambient atmosphere of which relative humidity was controlled. The surface conductivity was measured by measuring the charging and discharging currents for a certain charging time.

A paper insulated cable has been investigated with the simultaneous measurements of VF-PRPDA and dielectric spectroscopy and the results are presented in Chapter 11. The temperature of the cable was varied in the range from 20 °C to 60 °C.

In Chapter 12 the conclusions from this thesis are summarised and future directions are pointed out in Chapter 13.

1.4   Main contributions

The author has developed a measurement system that allows simultaneous measurements of Phase Resolved Partial Discharge Analysis (PRPDA) and Dielectric Spectroscopy with the frequency of applied voltage variable in the range 1 mHz - 400 Hz. The variable frequency PRPDA method is new and also the simultaneous measurement strategy.

The application of variable frequency on PD analysis is almost unexplored in the field of PD diagnostics, and the results in this project shows that much information about the PD-mechanisms can be obtained by using a variable frequency technique. It has further been shown that in many cases the situation at lower frequencies, e.g. 0.1 Hz and 1 Hz, is different than at power frequency 50 Hz.

The system for dielectric spectroscopy has included harmonic analysis of the fundamental frequency of the current. The harmonics is a direct consequence of the non-linear current caused by the partial discharge activity, and is an unexplored tool in the analysis of partial discharge currents. The introduction of the harmonics yields a more complete picture of the phase resolved PD-current, in addition to the fundamental components that yields the contribution of the PD-current to the 'loss' and the 'capacitance'.

An algorithm has been developed that can calculate the influence of PD on the dielectric spectroscopy current. The algorithm starts with the acquired PD-pattern obtained with the PRPDA technique, and calculates the non-linear current as measured by dielectric spectroscopy.

It has been shown that the average phase resolved PD-current could be measured with a PRPDA-system as well as with dielectric spectroscopy including harmonic analysis.

The method with variable low frequency partial discharge analysis has been demonstrated on objects with known discharge sources and on commercial insulation like machine insulation and oil impregnated paper cables.

The influence of surface conductivity on surface discharges has been investigated by altering the relative humidity of the ambient atmosphere. The effect of the surface conductivity is clearly visible in the frequency dependence of the PD activity.

1.5 List of publications

The following publications are included in this thesis:

I   J. T. Holbøll and H. Edin, "PD-Detection vs. Loss Measurements at High Voltages with Variable Frequencies", 10th International Symposium on High-Voltage Engineering (ISH), Montreal, Canada, 1997, pp. 4.421 - 4.425.

II   J. T. Holbøll, U. Gäfvert and H. Edin, "Time-Domain PD-detection vs. Dielectric Spectroscopy", Conference on Electrical Insulation and Dielectric Phenomena (CEIDP), Minneapolis, USA, 1997, pp. 498 - 503.

III   H. Edin and U. Gäfvert, "Harmonic Content in the Partial Discharge Current Measured with Dielectric Spectroscopy", Conference on Electrical Insulation and Dielectric Phenomena (CEIDP), Atlanta, USA, 1998, pp. 394 - 398.

IV   H. Edin, "The Influence of Dielectric Polarisation on the Measured PD Charge in a Two-Layer Dielectric System", Nordic Insulation Symposium (Nord-IS), Lyngby, Denmark, 1999, pp. 433 - 441.

V   J. Giddens, H. Edin and U. Gäfvert, "Statistical Analysis of Partial Discharges for The Frequency Range 1 mHz to 400 Hz", Nordic Insulation Symposium (Nord-IS), Lyngby, Denmark, 1999, pp. 141 - 148.

VI   J. Giddens, H. Edin and U. Gäfvert, "Measuring System for Phase-Resolved Partial Discharge Detection at Low Frequencies", 11th Int. Symp. on High-Voltage Engineering (ISH), London, United Kingdom, 1999, pp. 5.228 - 5.231.

VII   H. Edin, S. Jayaram and U. Gäfvert, "Influence of Relative Humidity on Surface Discharges Over the Frequency Range 0.1 Hz to 100 Hz", Submitted to IEEE Transaction on Dielectrics and Electrical Insulation.

VIII   H. Edin and U. Gäfvert, "Simultaneous Measurement of Phase Resolved Partial Discharges and Dielectric Spectroscopy", Submitted to IEEE Transaction on Dielectrics and Electrical Insulation.

The entire work was initialised and supervised by Uno Gäfvert.

In papers I and II Joachim Holbøll was the main author and the papers were written in the early part of this project. The work was performed during Joachim Holbøll's time as guest researcher at KTH. The author presented paper II at the conference.

The author is fully responsible for paper III and IV. The results from paper IV was developed during the authors time as guest researcher at the Technical University of Denmark (DTU) during the spring 1997.

Paper V and VI were written by Juleigh Giddens Herbig, but the results were obtained by the author and J. Giddens Herbig (supervised by the author).

The author is fully responsible for paper VII and VIII. The results in paper VII were developed by the author in collaboration with Shesha Jayaram during her time as guest researcher at KTH in 1999.

2 Literature review

2.1 Variable low-frequency diagnostic of PD infested insulation

The following section is a brief review of research previously performed with variable low-frequency diagnostic methods on PD-infested electrical insulation. The review cover investigations performed with pulse-measuring techniques as well as integrated methods like the Schering bridge or dielectric spectroscopy.

One of the original papers on the subject of high-voltage testing of electrical insulation with frequencies lower than power frequency is a paper by Bhimani from 1961 [15]. The main idea was to replace 60 Hz (USA) tests with a low-frequency test in order to reduce the supply power and thereby reduce the weight and the size of the equipment. Previously, DC voltage tests had been performed with the same motivation but it had been found that testing with DC voltage did not stress the insulation in the same way as with 60 Hz. The deviations occur for heterogeneous (laminated) insulation systems like machine insulation where differences in permittivity and conductivity between different layers made the field distribution frequency dependent. At DC voltage and at very low frequencies the field distribution was found to be dominated by the conductivities in conjunction to at power frequency where the field distribution was determined by the permittivities. Gas-filled voids were also stressed in a way different from 60 Hz, and was not necessarily detected at rated test voltage, or it could occur that the insulation was damaged due to the abnormal stress. The compromise between DC and 60 Hz was to choose the lowest possible frequency that still stressed the insulation capacitively as for 60 Hz. The lowest possible frequency that would yield a field distribution that was to 99.5 % capacitive for the most common insulating materials was determined to be around 0.1 Hz.

Virsberg and Kelen at the ASEA Research Laboratory discussed the problem with a frequency dependent field distribution and analysed the situation for a two-layer heterogeneous dielectric system in a Cigré report from 1964 [9]. Their analysis indicated that the field distribution was still determined by the permittivities at 0.1 Hz if the volume resistivity of none of the materials in the heterogeneous system was lower than 10^{11} Ωm.

The benefits with the power supply reduction with low-frequency methods is particularly useful for large capacitive objects such as machine insulation [9, 15], but low-frequency test methods was early adopted also on power-cables in 1968 by Haga and Yoneyama [16]. They investigated the breakdown strength of oil-impregnated paper cables at different applied voltage frequencies, and also the frequency dependence of the dielectric properties with different moisture content. Furthermore, they also performed tan-δ tip-up tests at different frequencies and found that the tip-up curves were similar at 0.1 Hz and 50 Hz.

The interest of low-frequency methods in the beginning was mainly for performing over-potential testing to ensure that the insulation could take this over-voltage. However, partial discharge investigations at low frequencies was performed already by Bhimani in 1961, and was taken up in England by Hilder et al 1973 [17]. They developed a low-frequency

generator that could operate from 0.01 Hz to power frequency. This generator was used in 1977 by Miller and Black [18] in their studies of the applied voltage frequency dependence of partial discharge magnitude distributions. In their further research, they supplied this information with discharge energy and loss-tangent measurements on machine insulation in 1979 [19].

The activities in England continued by Burnley, Ellison and Exon; who developed a generator and a bridge for variable low frequency capacitance and loss-tangent measurements [20]. This technique was supplemented by measurements of charge-transfer oscillograms by Burnley and Exon in 1991 [21].

Low-frequency methods applied on XLPE cables with different defects that caused PD was adopted by Haga et al in Japan 1983, of which some results were published in English in 1988 [22].

In 1996 a variable low-frequency high-voltage generator was developed by Kalkner et al at the Technical University of Berlin [23]. They applied the technique for dissipation factor measurements on water-tree infested XLPE insulation [23], but also for PD-measurements at variable frequencies [24].

At KTH a system for high voltage dielectric spectroscopy have been developed for diagnosis of water-tree infested XLPE cables. The results achieved in that project have recently been summarised in [25] with further references to the subject of diagnosis of water-tree infested XLPE cables. The development of the high-voltage dielectric spectroscopy system started in 1993 with the experience from Gäfvert and Nettelblad [26] and has today resulted in a commercialised system [27].

With the beginning in 1996 the author with co-workers have developed measurement system for Variable-Frequency PRPDA (VF-PRPDA) analysis and for simultaneous measurement of VF-PRPDA and dielectric spectroscopy. The development of these systems and the findings obtained by using them are the scope of this thesis.

2.2 PD and high voltage dielectric spectroscopy

High voltage dielectric spectroscopy is an extension of the classical methods based on the Schering bridge technique to measure the capacitance and the dielectric loss [1]. Much of the early work has therefore been spent on relating the partial discharge intensity to the non-linear behaviour with increasing voltage of the loss-tangent and capacitance.

Dakin [28] described in 1959 how partial discharges influenced bridge-measurements of loss-tangent (then named dissipation factor) and capacitance; and demonstrated the results on a polystyrene capacitor in series with an air gap, but explained also the loss-tangent and capacitance tip-up for mica generator insulation. In 1966, Bartnikas [29], developed a model from which the pulsed corona power loss measured with a Schering-bridge could be computed from the knowledge of discharge parameters such as the sparking voltage of a gap. A refined model was presented in 1969 [30] and was experimentally demonstrated on a discharge gap filled with helium. In 1978 Kelen [14] made use of Fourier analysis in a critical analysis on how partial discharges influence loss-tangent measurements. Kelen

verified his results on a pulse-pair model and made comments about the harmonics caused by the partial discharge current. In 1982 Burnley and Exon [31] made use of a Fourier expansion of the PD-current in their work to obtain the link between the three common PD measurement methods: single discharge measurements, bridge techniques and charge-transfer oscillograms. However, they obtained the same relations as Dakin [28] and similar to what is presented in this thesis, but they did not make any further use of the harmonics of the PD-current.

High voltage dielectric spectroscopy with harmonic analysis was performed on Micadur® stator bars within ABB during 1992 and 1993 [32]. They found a strong correlation between the loss-tangent tip-up and the occurrence of harmonics in the current, of which the third harmonic was most pronounced. In the same report they also demonstrated that for Micadur® insulation the test could be equally well performed at 2 Hz as at 50 Hz.

A measure of the harmonic distortion of the dielectric response current named Harmonic Loss Quantity (HLQ) was in 1998 introduced by Goffeaux et al [33], and was used as a measure of the quality of machine insulation.

Moreover, Fourier analysis of the phase resolved partial discharge current has been applied as a tool for PD defect recognition by Hücker and Kranz [34] (1995), but without relating this current to integrated measures like loss-tangent tip-up.

In this project it is shown that much of the information given by a PRPDA pattern can be obtained with dielectric spectroscopy, in particular if the harmonics of the current are considered. The demonstration of this relation required the development of a system for simultaneous measurement of VF-PRPDA and dielectric spectroscopy.

3 Basic concepts

This chapter contains a brief description of the common partial discharge sources that may occur in defects and at highly stressed points in high voltage equipment. It continues with a short discussion about two PD mechanisms that yields principally different phase-angle resolved PD currents. The last section is devoted for a qualitative discussion about some basic mechanisms that yield a frequency dependent PD activity.

An overview about the basics of PD related phenomena and its measurements can be found in the books by Kreuger [35] and Bartnikas and McMahon (eds.) [36].

3.1 Occurrence of partial discharges

Partial discharges are by definition only confined to a part of the electrical insulation system. The type of discharge is often divided into three groups due to their different origin.

1) Corona discharges, i.e. discharges in gases (or liquids) caused by a locally enhanced field from sharp points on the electrodes. Corona is often harmless, but by-products like ozone and nitric acids may chemically deteriorate closely lying materials.

2) Internal discharges,

a) Cavity discharges, i.e. discharges from gas-filled voids, delaminations, cracks, etc. within solid insulation. A refined classification could be made to cavities that are on one side bounded by the metallic electrode, and to cavities that are completely surrounded by the insulating material. Voids may have its origin from cast insulation like epoxy spacers in SF_6 bus bars, from dried out regions in oil-impregnated paper-cables, from gas-bubbles in plastic insulation, etc. Delaminations occur in laminated insulation like the stator-bar insulation of large electrical machines that often is composed of mica based tapes with a binding enamel like epoxy. Cracks could for example occur in mechanically stressed insulation, e.g. in loose stator bars that are vibrating.

b) Treeing discharges, i.e. current pulses within an electrical tree. The electrical tree may start from a protrusion on the electrode or from imperfections like contaminating particles embedded in the solid insulation.

3) Surface discharges, i.e. discharges on the surface of an electrical insulation where the tangential field is high, e.g. the porcelain- or polymeric housing of high-voltage devices. Other common sources of surface discharges are terminations of cables or the end-windings of stator windings.

PD from a particular source, like a void in solid dielectrics, may start like a cavity discharge that on a later stage introduce electrical trees, and then transfer to treeing

discharges. Another example could be corona discharges from an edge in a termination, which origins as a source for corona discharges, but that at a later stage start to propagate as surface discharges.

3.2 Phase dependency

3.2.1 Corona discharges from a point in air

The canonical case for external PD due to corona is a point in air. The corona process under alternating voltage has been extensively investigated [37], and only remarks about the phenomenon that is relevant here is discussed. A point-plane arrangement with the needle on high potential will cause discharges first at negative polarity when the applied voltage amplitude is increased. These discharges are of a relatively small magnitude but of a high repetition rate and are named Trichel-pulses. At a higher voltage amplitude streamers will start to appear around the peak of the positive voltage. These streamers are of a magnitude much larger than the Trichel-pulses under negative polarity but has a much lower repetition rate and are more fluctuating. However, as long as the frequency is low, the gap spacing short and the applied voltage not much higher than the inception voltage then the discharge activity is symmetric around the peaks of respective polarity. This behaviour is due to the fact that the effect of charges created from previous discharges is negligible during this conditions and that the recurrence of the discharges is only controlled by voltage magnitude and polarity.

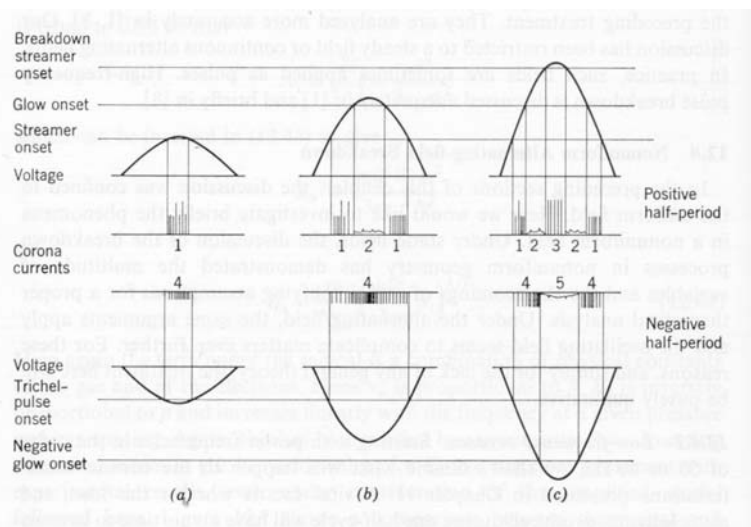*Figure 3.1 Corona discharge modes under applied voltage at 50 Hz and three different amplitudes above inception voltage, [37, p.382]. The symmetry around the applied voltage peaks is a clear indication that the discharge mechanism is voltage controlled. The number on the current wave refers to the corona mode: 1. Streamers. 2. Glow. 3. Breakdown streamers. 4. Trichel pulses. 5. Negative glow.*

13

3.2.2   Discharges in dielectric bounded cavities

The canonical discharge source for internal discharges is a void embedded in a dielectric material. The charges liberated by the first discharge are drifted in the applied field to the walls of the void where they are deposited. The field within the void is then the sum of the field from the applied voltage (Laplacian field) and the field caused by the deposited space (surface-) charges (Poissonian field). The consecutive discharges follow the total field within the void and the next discharge occurs when the field again is above the critical field. This process yields that discharges may occur even when the applied voltage is zero because the Poissonian field from deposited charges may be high enough. The Poissonian field component cause a shift of the discharge activity from the peaks of the applied voltage to the rising-parts of the voltage, Figure 3.2, i.e. the discharge process follows the electrical field and not the applied voltage.
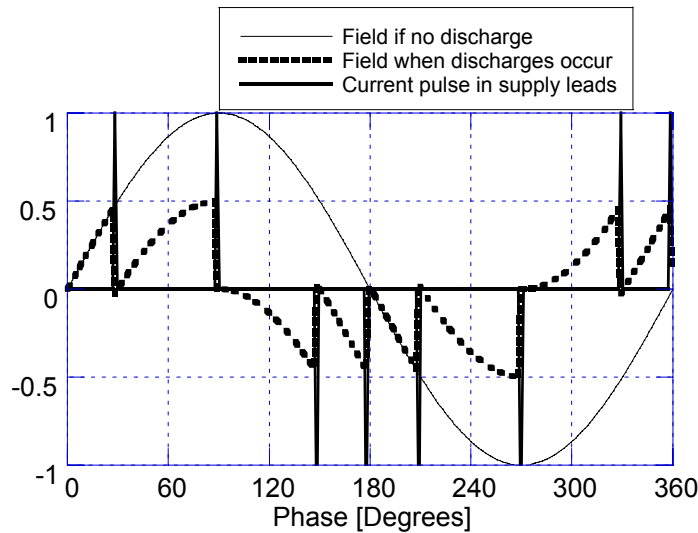
Figure 3.2 Field in void when no discharge occurs, when discharges occur and the current pulse in the supply leads, arbitrary units. The inception voltage is 50 % of applied voltage and equal on both polarities.

The shift of the discharge sequences from symmetrical around the peaks to the rising voltage polarity and around the zero-crossings, is also observed for other defects than voids, e.g. discharges caused by electrical trees [38] and surface discharges [39, 40].

14

3.3 Frequency dependent mechanisms

In this section, a qualitative discussion of some basic mechanisms that yield a frequency dependent PD activity is presented. The discussion concerns the statistical time lag, the dispersion in bulk permittivity and the influence of bulk conductivity and surface conductivity.

As will be seen by the examples below, dielectric spectroscopy can give many of the parameters about the insulation system that may be required to know, in order to achieve an understanding of the frequency dependence of PD.

3.3.1 Statistical time lag

There are at least two conditions that should be fulfilled if a partial discharge should occur, i.e. the applied voltage or electric field should be high enough and a seed-electron (start electron) must be present at a suitable position to yield a critical avalanche that develops into a partial discharge [41].

The time between the fulfilment of the voltage condition, i.e. when the PD inception voltage is reached, until the seed-electron condition is achieved is the statistical time lag, Δt_{lag}.

For PD under AC voltages there are two kinds of this statistical time lag. The first time lag is the inception delay Δt_{inc} [41], i.e. the time between the application of the AC voltage with an amplitude larger than V_{inc} and the occurrence of the first discharge. This time may be long, in particular for small voids and voltages close to inception. Niemeyer [41] develops a relation between Δt_{inc}, the void size, pressure, over-voltage ratio and the background radiation. Niemeyer gives as an example that for a spherical void of 1 mm in diameter, filled with air of normal pressure and stressed with a voltage of two times its theoretical inception voltage it will take roughly 1000 seconds until the first discharge. For laboratory experiments of a more fundamental nature, the irradiation of voids by a gamma radiation source will reduce this inception delay significantly [42].

However, even if Δt_{inc} is shorter than for the example above it will ultimately interpreted as a reduced amount of charge per cycle when PD measurements are performed by the PRPDA technique.

The second statistical time lag that occurs is the time between voltage level fulfilment and the discharge occurrence, when previous discharges have occurred. This time lag is often short because there are many more free electrons available after the first PD. The appearance of this time lag at AC voltages yields a corresponding phase lag, $\Delta \varphi_{lag}$ (3.1) and discharges at an over-voltage; thus, fewer discharges per cycle, but of a larger amplitude. This second time lag is reflected in the PRPDA pattern if it is longer than some per cents of the applied voltage period.

$$\Delta \varphi_{lag} = \frac{\Delta t_{lag}}{T} \cdot 360° \qquad (3.1)$$

The influence of both kinds of statistical time lag on, for example the total charge per cycle, will become less with decreasing frequency.

A recognition of the inception delay (the first time lag) is not possible with the PRPDA technique, but is for example directly seen with the Pulse-Sequence Analysis (PSA) technique by Hoof and Patsch [43] or in this thesis by simultaneous measuring the PD current with dielectric spectroscopy and storing all acquired samples of all periods for post-processing.

3.3.2   Dispersion in permittivity

The electrical field in gas-filled voids and cavities embedded in an otherwise solid dielectric is enhanced compared to the external field. For example, the field in a spherical void embedded in a homogeneous dielectric with the relative permittivity $\varepsilon'_r(\omega)$ and stressed by a homogenous field has the field enhancement factor f_E [44],

$$f_E = \frac{3\varepsilon'_r(\omega)}{1+2\varepsilon'_r(\omega)} \tag{3.2}$$

In a delamination the field enhancement factor is more close to $\varepsilon'_r(\omega)$, Figure 3.3.

$$E_g = f_E E_b = \frac{3\varepsilon'_r(\omega)}{1+2\varepsilon'_r(\omega)} E_b \qquad\qquad E_g = f_E E_b = \varepsilon'_r(\omega) E_b$$
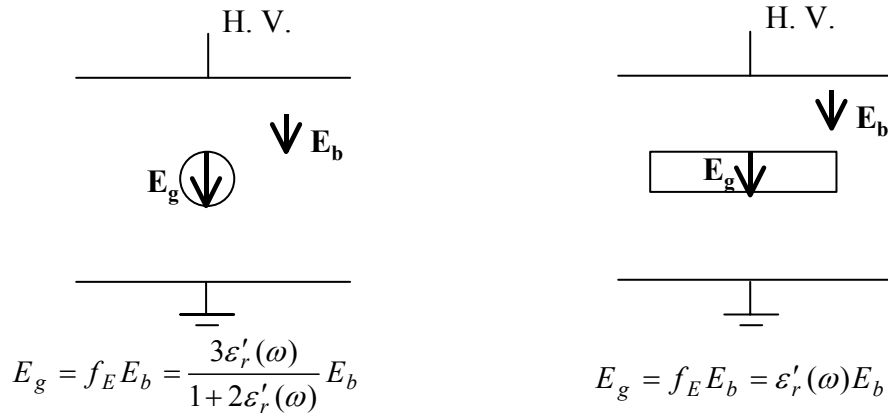
Figure 3.3 Field enhancement in a spherical void and a delamination caused by the difference in permittivity between the gas, $\varepsilon'_r \approx 1$ and the solid dielectric, $\varepsilon'_r(\omega)$. E_g is the field in the gas filled cavity and E_b is the field in the bulk material.

The dispersion of the permittivity yields that the field enhancement factor for a cavity varies with applied voltage frequency, which is one source to a frequency dependent inception voltage, V_{inc}. Many insulation materials or systems are dispersive at low frequencies, i.e. below 50 Hz, e.g. oil impregnated pressboard (transformer insulation) and porcelain as shown by Gäfvert and Nettelblad [26].

3.3.3　Influence of bulk conductivity

The influence of a non-zero bulk conductivity may become relevant at low frequencies as demonstrated for the laminate in Figure 3.4.
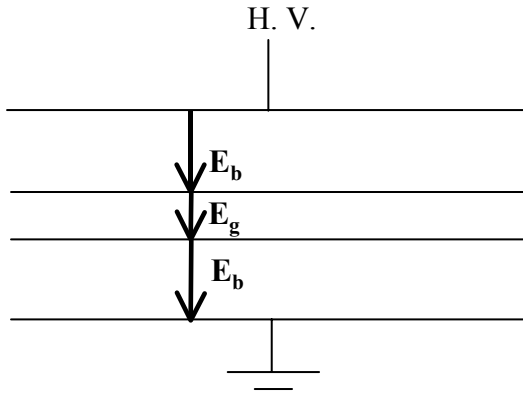
Figure 3.4 Laminate with an air-filled delamination.

The material is assumed to have a pure permittivity ($\varepsilon_r'' = 0$), here frequency independent for simplicity, and a DC-conductivity σ_{DC}, i.e. the complex permittivity may be written as,

$$\widetilde{\varepsilon}_r(\omega) = \varepsilon_r' - j\frac{\sigma_{DC}}{\omega\varepsilon_0} \tag{3.3}$$

The voltage across the delamination is obtained from the continuity equation of the displacement field, i.e.

$$\varepsilon_g E_g = \widetilde{\varepsilon}_r(\omega)E_b \tag{3.4}$$

$$V_g = \frac{V_0}{1 + \dfrac{1}{\varepsilon_r' - j\dfrac{\sigma_{DC}}{\omega\varepsilon_0}} \cdot \dfrac{d_b}{d_g}} \xrightarrow{\omega\to 0} \frac{V_0}{1 + \dfrac{j\omega\varepsilon_0}{\sigma_{DC}} \cdot \dfrac{d_b}{d_g}} \tag{3.5}$$

As indicated in (3.5), when the frequency tends to zero (low frequencies) the voltage across the gap is determined by the conductivity and in the limit $\omega = 0$, the air-gap is charged to the (then DC) voltage V_0. The conductivity will at low frequencies also determine the recharging time-constant of cavities after a previous discharge, see Chapter 11.

The situation with a pure DC-conductivity is an over-simplification for many insulating systems and is only used to indicate the trend with decreasing frequency.

3.3.4 Influence of surface conductivity

The importance of the surface conductivity at low frequencies will be indicated for a spherical void, Figure 3.5.
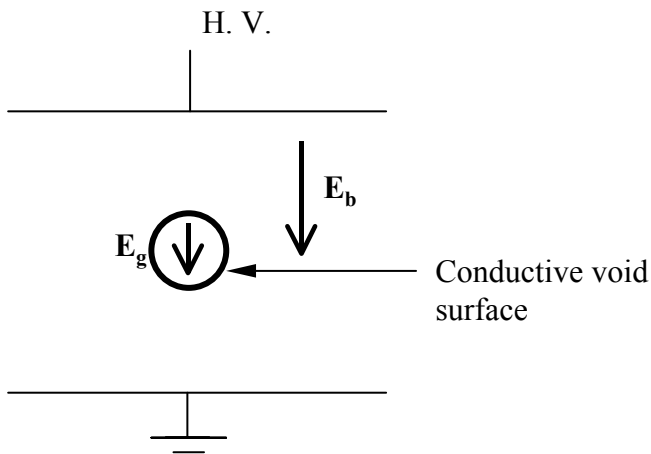
Figure 3.5 Spherical void with a non-zero surface conductivity.

At low enough frequencies the surface conductivity will prevent any build-up of field in the void and as such no partial discharges will occur, i.e. the surface conductivity has a screening effect on the field.

The decay time of charges deposited on a spherical void wall has been studied analytically by McAllister [45], where it is shown that the decay time decrease with increasing surface conductivity and decreasing permittivity of the bulk material.

4 Partial discharges and dielectric spectroscopy

4.1 Introduction

In this section the relation between the sequence of partial discharges, i.e. the partial discharge current, and the dielectric spectroscopy current will be developed. This analysis explains how the PD-current contributes to the loss- and capacitive- components of the dielectric response current. Furthermore, the harmonic analysis of the non-linear PD-current yields relations that are useful for classification of discharge sources.

4.2 Linear response current

The dielectric response current for a material or system can in frequency domain be measured after the application of a sinusoidal voltage with frequency f, and amplitude V_0,

$$V(t) = V_0 \sin(\omega t),$$
(4.1)

where $\omega = 2\pi f = 2\pi / T$ is the angular frequency and T is the period.

The dielectric response current for a linear, homogeneous and time-invariant insulation material or system from the excitation by (4.1) can be written as [46],

$$i_{Lin}(t) = \omega V_0 \left(C'_{Lin}(\omega)\cos(\omega t) + \left(C''_{Lin}(\omega) + \frac{G_{DC}}{\omega} \right)\sin(\omega t) \right),$$
(4.2)

or if the geometrical capacitance C_0 is known,

$$i_{Lin}(t) = \omega C_0 V_0 \left(\varepsilon'_r(\omega)\cos(\omega t) + \left(\varepsilon''_r(\omega) + \frac{\sigma_{DC}}{\omega \varepsilon_0} \right)\sin(\omega t) \right)$$
(4.3)

$C'_{Lin}(\omega)$ and $C''_{Lin}(\omega)$ represents the real and imaginary part of a complex capacitance, and similarly are $\varepsilon'_r(\omega)$ and $\varepsilon''_r(\omega)$ the real and imaginary part of a (relative) complex permittivity, i.e.

$$\widetilde{C}_{Lin}(\omega) = C'_{Lin}(\omega) - jC''_{Lin}(\omega) = \left(\varepsilon'_r(\omega) - j\varepsilon''_r(\omega) \right)C_0 = \widetilde{\varepsilon}_r(\omega)C_0$$
(4.4)

In common terms is the capacitance referred to only $C'_{Lin}(\omega)$ and $C''_{Lin}(\omega)$ to the (dielectric) loss. However, the dielectric power loss measured in [W/m^3] is given by

$$P = \omega \left(C''_{Lin}(\omega) + \frac{G_{DC}}{\omega} \right) V_0^2 = \omega \left(\varepsilon''_r(\omega) + \frac{\sigma_{DC}}{\varepsilon_0 \omega} \right) C_0 V_0^2 \qquad (4.5)$$

which is proportional to $C''_{Lin}(\omega)$ or $\varepsilon''_r(\omega)$.

G_{DC} is the DC-conductance and σ_{DC} is the DC-conductivity of the insulation material.

The ratio of the in phase component to the quadrature component of the linear current defines the loss-tangent, *tan δ(ω)*, i.e. the tangent of the loss-angle, *δ(ω)*,

$$\tan \delta(\omega) = \frac{C''_{Lin}(\omega) + G_{DC}/\omega}{C'_{Lin}(\omega)} = \frac{\varepsilon''_r(\omega) + \sigma_{DC}/\omega\varepsilon_0}{\varepsilon'_r(\omega)} \qquad (4.6)$$

A graphical interpretation of the current phasors is shown in Figure 4.1, where the loss component is in phase with the applied voltage, and the capacitive component is in quadrature to the applied voltage. The loss-angle is the angle between the capacitive phasor and the total current phasor.
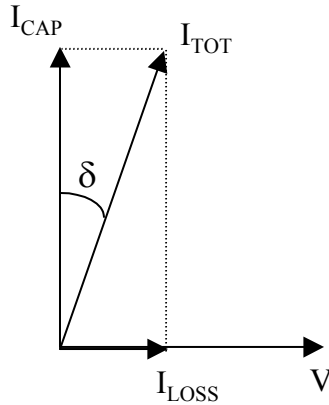
Figure 4.1 A phasor diagram of the in phase and quadrature component of the linear dielectric response current when excited by a harmonic voltage.

The functional dependency on ω indicates that the complex permittivity is frequency dependent, i.e. the material is dispersive. In this project, the dispersion of the insulation system is of interest in the way that it sometimes can explain the frequency dependence of the partial discharge activity, see Chapter 3. For example, the electric field in a void embedded in an otherwise homogeneous dielectric is dependent on the permittivity of the dielectric. If the permittivty is frequency dependent, then, for example, the inception voltage is also frequency dependent.

The absolute value, the frequency dependence, and the voltage dependency for non-linear materials, of the complex permittivity has been extensively used as a measure of the dielectric properties of electrical insulation, but also as a tool to trace indications of any

progressive deterioration, see for example the monographs by Jonscher [46, 5], Bartnikas and Eichhorn (eds.) [47] and Hedvig [48].

Practical applications of dielectric spectroscopy for diagnosis of the electrical insulation of power apparatus have been on water-tree infested XLPE cables, e.g. at KTH [25] and detection of moisture in oil impregnated paper insulation such as cable insulation and transformer insulation, e.g. Haga and Yoneyama [16], Gäfvert et al [49] and Neimanis [7].

A composite or effective complex capacitance is measured if the insulation system is a combination of different materials. This composite complex capacitance can be determined from the complex capacitances of the ingoing materials, see Edin [8] or Gäfvert [6]. A practical application of a composite structure composed of oil and pressboard is the power transformer. The knowledge of the construction of the transformer together with material properties has shown to be a fruitful tool in the analysis of dielectric response measurements of power transformers [49].

In the forthcoming sections of this chapter the current of partial discharges will be included in the total dielectric response current. The manifestation of the non-linear PD-current in the dielectric spectroscopy will be related to the PRPDA pattern.

4.3 Partial discharges in the dielectric response current

4.3.1 Fourier series analysis

Partial discharges may occur for a given system above a certain voltage, i.e. the PD inception voltage. The current of partial discharges, $i_{PD}(t)$, is the sequence of the single discharges that occur during the alternations of the applied voltage. The partial discharge current may be described as the sum of the individual current impulses,

$$i_{PD}(t) = \sum_i q_i \delta(t - t_i) \tag{4.7}$$

where q_i is the charge contained in discharge number i occurring at time t_i after the voltage application. The index i run over all discharges during the application of voltage. The generalised delta function, $\delta(t)$ is Dirac's delta function or delta distribution [50, p.260]. This representation does not consider the exact temporal variation of the current impulse within the nano-second region; it is merely a representation of the charge transported in the current impulse in the sense,

$$q_i = \int_{t_i -}^{t_i +} q_i \delta(t - t_i) dt \tag{4.8}$$

The fluctuating PD-current is in most cases only quasi-periodic with the applied voltage period. However, it will be assumed later that the reproducibility of a PD-pattern makes the PD-current in average periodic.

Nevertheless, a Fourier-series expansion of the PD-current can be performed on each applied voltage period,

$$i_{PD}(t) = \frac{a_{0k}}{2} + \sum_{n=1}^{\infty} \left(a_{nk} \cos(n\omega t) + b_{nk} \sin(n\omega t) \right),$$ (4.9)

$$t \in \left[(k-1)T, kT \right], \quad k = 1, 2, 3, ..., N_{P-1}, N_P,$$

where N_P is the total number of periods of voltage application. It should be observed that the Fourier coefficients a_{nk} and b_{nk} in general varies from period to period.

The individual harmonics for each period of the applied voltage can be computed from (4.7) by the following Fourier integrals [50, p. 272],

$$a_{nk} = \frac{2}{T} \int_{(k-1)T}^{kT} \sum_i q_i \delta(t - t_i) \cos(n\omega t) dt$$ (4.10)

and

$$b_{nk} = \frac{2}{T} \int_{(k-1)T}^{kT} \sum_i q_i \delta(t - t_i) \sin(n\omega t) dt$$ (4.11)

Reversing the order between the integration and the summation, and using the integration properties of the delta function [50, p. 260] yields,

$$a_{nk} = \frac{\omega}{\pi} \sum_i q_i \cos(n\omega t_i) = \frac{\omega}{\pi} \sum_i q_i \cos(n\varphi_i)$$ (4.12)

and

$$b_{nk} = \frac{\omega}{\pi} \sum_i q_i \sin(n\omega t_i) = \frac{\omega}{\pi} \sum_i q_i \sin(n\varphi_i)$$ (4.13)

where, $\varphi_i = \omega t_i$ and $t_i \in \left[(k-1)T, kT \right]$

A PRPDA system acquires the single discharges with respect to the phase of the applied voltage. This method keeps the magnitude of the individual discharges but their absolute time of occurrence and the consecutive order in which they appear is lost. However, an average measure of the PD-current is obtained from the PD-pattern (φ-q-n pattern), with

$$\bar{q}_j(\varphi_j, \omega, V_0) = \frac{1}{N_P} \sum_m n(\varphi_j, q_m) q_m(\varphi_j, \omega, V_0) \tag{4.14}$$

where j and m represents the discrete phase- and amplitude channels. With the ICM system the numbers of phase- and amplitude- channels are the same and equal to 256.

In the further analysis it is a fundamental assumption that the average Fourier coefficients,

$$\bar{a}_n = \frac{1}{N_P} \sum_{k=1}^{N_P} a_{nk} \tag{4.15}$$

and

$$\bar{b}_n = \frac{1}{N_P} \sum_{k=1}^{N_P} b_{nk} \tag{4.16}$$

can be computed from the average PD-current or average phase distribution of charges (4.14).

Hence,

$$\bar{a}_n = a_n^{PDP} = \frac{\omega}{\pi} \sum_{j=1}^{256} \bar{q}_j(\varphi_j, \omega, V_0) \cos(n\varphi_j) \tag{4.17}$$

and

$$\bar{b}_n = b_n^{PDP} = \frac{\omega}{\pi} \sum_{j=1}^{256} \bar{q}_j(\varphi_j, \omega, V_0) \sin(n\varphi_j) \tag{4.18}$$

The current flowing towards the electrodes after the application of a voltage across the samples may be of a different origin. In this project, if not else stated, it is assumed that at low voltage the only current is the linear dielectric response current. The only non-linear current component that is included here comes from the onset of partial discharges above the PD inception voltage. However, the dielectric response current could in general include other non-linear components, e.g. from water-tree infested regions as shown by Bulinski et al [51] or from non-linear field gradings in terminations.

The apparent dielectric response current, $i_{DR}(t)$ that is flowing after the application of an alternating voltage higher than the inception voltage of PD is the sum of the linear response current, $i_{Lin}(t)$ (4.2) and the average partial discharge current, $\overline{i_{PD}(t)}$, i.e. (4.9) with the average Fourier coefficients (4.17, 4.18) inserted.

$$i_{DR}(t) = i_{Lin}(t) + \overline{i_{PD}(t)} =$$

$$\frac{\omega}{2\pi} \sum_{j=1}^{256} \overline{q}_j(\varphi_j, \omega, V_0) +$$

$$+ \omega \left(C'_{Lin}(\omega) + \frac{a_1^{PDP}}{\omega V_0} \right) V_0 \cos(\omega t) + \omega \left(C''_{Lin}(\omega) + \frac{G_{DC}}{\omega} + \frac{b_1^{PDP}}{\omega V_0} \right) V_0 \sin(\omega t) + \quad (4.19)$$

$$+ \sum_{n=2}^{\infty} \left(a_n^{PDP} \cos(n\omega t) + b_n^{PDP} \sin(n\omega t) \right)$$

The apparent dielectric response current has been divided into three parts that will be further discussed. The first term is the DC component that is zero only if there is equal amount of positive and negative charge in the PD-current. The second part (terms three and four) is the sum of the linear dielectric response current and the fundamental components of the PD-current and the third part contains the harmonic components of the PD-current.

One measure of the distortion of the current is the harmonic content, HC_n (4.20) of the nth harmonic component of the apparent dielectric response current,

$$HC_n = \frac{\sqrt{a_n^2 + b_n^2}}{\sqrt{\sum_{n=1}^{\infty} a_n^2 + b_n^2}} \approx \frac{\sqrt{a_n^2 + b_n^2}}{\sqrt{a_1^2 + b_1^2}} \quad (4.20)$$

where the last approximation is valid when the current is dominated by the displacement current.

4.3.2 DC component

The DC term in the dielectric response current (4.19) is non-zero only if a unipolar charge transport is present. In PD context the origin of this current could be for example corona discharges from a sharp point on one of the electrodes. If the measurement system for dielectric spectroscopy is based on an integrating device like an electrometer, as in this project, then a unipolar current will cause a ramp at the output of the electrometer that finally brings the electrometer to saturation and ultimately destroy the measurement. The cure to overcome this problem is to use a mixed capacitive and resistive feedback element in the electrometer or, if possible, to replace the electrometer with a current amplifier.

4.3.3　The fundamental components

In traditional dielectric spectroscopy measurements the fundamental components of the current are measured and then related to the complex capacitance or complex permittivity. A direct application of such a strategy when the voltage is so high that partial discharges occurs will cause that an apparent complex capacitance is measured. The real and imaginary part of this apparent capacitance is influenced by the partial discharge current in the way described by (4.19). The real and imaginary part of the apparent capacitance and loss are defined as

$$C'_{App}(\omega) = C'_{Lin}(\omega) + \Delta C'_{PD}(\omega) = C'_{Lin}(\omega) + \frac{a_1^{PDP}}{\omega V_0} =$$
$$C'_{Lin}(\omega) + \frac{1}{\pi V_0} \sum_{j=1}^{256} \bar{q}_j(\varphi_j, \omega, V_0) \cos(\varphi_j) \tag{4.21}$$

and

$$C''_{App}(\omega) = C''_{Lin}(\omega) + \frac{G_{DC}}{\omega} + \Delta C''_{PD}(\omega) = C''_{Lin}(\omega) + \frac{G_{DC}}{\omega} + \frac{b_1^{PDP}}{\omega V_0} =$$
$$C''_{Lin}(\omega) + \frac{G_{DC}}{\omega} + \frac{1}{\pi V_0} \sum_{j=1}^{256} \bar{q}_j(\varphi_j, \omega, V_0) \sin(\varphi_j) \tag{4.22}$$

Expressions similar to above was early developed by Dakin [28] and Bartnikas [29], and their results were further examined by Kelen [14] on a pulse-pair model and machine insulation, and also developed by Burnley and Exon [31] in conjunction with a model for void discharges.

However, in this project the storing facilities supplied with a PRPDA system has been used to put these relations in new light, in particular when PRPDA patterns can be acquired simultaneously with the measurements of the dielectric response current.

To what extent the partial discharge current influence the apparent capacitance and the apparent loss is governed by how the partial discharges are distributed in the phase of the applied voltage, i.e. by the integral of the products of $\bar{q}(\varphi)$ with *cos(φ)* and *sin(φ)*.

A pulse-pair model is discussed and experimentally demonstrated by Kelen [14] and in this project [52]. When the PD pulse-pair is located at the zero-crossings of the applied voltage they will only contribute to C'_{App}, but when the pulse-pair is displaced an angle α from the zero-crossings towards the peaks, a successive shift from C'_{App} to C''_{App} will occur. Finally, at $\alpha = 90°$ the pulse-pair will only contribute to C''_{App}. Further examinations of the contributions to C'_{App} and C''_{App} have been presented in [52, 53, 54, 55].

4.3.3.1 Symmetry relations for the fundamental components

From the above relations, (4.21) and (4.22), it becomes clear that any phase distribution of charge that is symmetric around the peaks of the applied voltage will only make contribution to C''_{App} and not to C'_{App}. The opposite situation occurs if the discharge activity is symmetrically distributed around the zero-crossings of the applied voltage. It should be noticed that these relations holds even if the total charge during the two half-cycles are different, i.e. $\sum_{j=1}^{256} \overline{q}_j(\varphi_j, \omega, V_0)$ is non-zero.
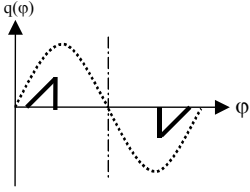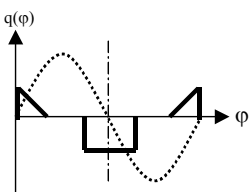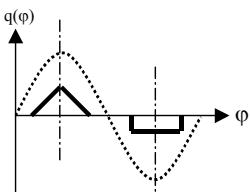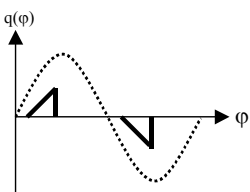
A PD-current, $\overline{q}(\varphi)$ that is evenly distributed around the expansion origin, i.e. $\overline{q}(\varphi) = \overline{q}(-\varphi)$ contributes only to the capacitive component; whereas a contribution only to the loss appears when $\overline{q}(\varphi)$ is odd around the expansion origin, i.e. $\overline{q}(\varphi) = -\overline{q}(-\varphi)$.

4.3.4 Information given by the harmonics of the PD-current

The PD-current has a direct influence on the fundamental components of the current and thereby makes a contribution to the apparent capacitance and the apparent loss. However, a more detailed analysis of the phase resolved PD-current requires that the harmonics of the fundamental component of the current are included.

Some features of the phase resolved PD-current are directly obtained from the Fourier coefficients without making a direct summation of the Fourier series and making a visual observation. Some of the most striking features are summarised in Table 4.1. The concept of Fourier analysis is used by Hücker and Kranz [34] as a tool for PD source classification, but without relating the components to dielectric spectroscopy measurements.

Table 4.1 Features of $\overline{q}(\varphi)$ directly obtained from the Fourier coefficients

Appearance	Observation	Influence on the Fourier coefficients
1) 	$\overline{q}(\varphi)$ is odd around origin, $\overline{q}(\varphi) = -\overline{q}(-\varphi)$	$a_n \equiv 0, \forall n$
2) 	$\overline{q}(\varphi)$ is even (symmetric) around origin, $\overline{q}(\varphi) = \overline{q}(-\varphi)$	$b_n \equiv 0, \forall n$
3) 	$\overline{q}(\varphi)$ is symmetric around the peaks of the applied voltage but may be different at different polarities.	$a_n = 0, n\ odd;\ sp.\ a_1 = 0$ $b_n = 0, n\ even$
4) 	The behaviour of $\overline{q}(\varphi)$ is such that $\overline{q}(\varphi) = -\overline{q}(\varphi + \pi)$	$a_n = 0, b_n = 0, \forall\ even\ n$

Case 1) and 2) follows directly from the property that an odd and even function is expanded only with odd and even base functions. Case 4) is shown before case 3), because some of the results from this proof are required for a proof of case 3). The Fourier coefficients a_n and b_n of $\overline{q}(\varphi)$ can be computed by (4.23).

$$c_n = \frac{a_n - ib_n}{2} = \frac{1}{2\pi} \int\limits_0^{2\pi} \overline{q}(\varphi) e^{-jn\varphi} d\varphi \qquad (4.23)$$

The following property is useful,

$$e^{-jn(\varphi+\pi)} = e^{-jn\pi} \cdot e^{-jn\varphi} = (-1)^n \cdot e^{-jn\varphi} \qquad (4.24)$$

and the proof follows as

$$c_n = \frac{1}{2\pi} \int\limits_0^{\pi} \overline{q}(\varphi) e^{-jn\varphi} d\varphi + \int\limits_{\pi}^{2\pi} \overline{q}(\varphi) e^{-jn\varphi} d\varphi = \{\varphi = \psi + \pi \; in \; second \; integral\} =$$

$$= \frac{1}{2\pi} \int\limits_0^{\pi} \overline{q}(\varphi) e^{-jn\varphi} d\varphi + \frac{1}{2\pi} \int\limits_0^{\pi} \overline{q}(\psi + \pi) \cdot (-1)^n e^{-jn\psi} d\psi = \qquad (4.25)$$

$$= \left\{ \begin{array}{l} \varphi = \psi \; in \; second \; integral, \\ and \; \overline{q}(\varphi) = -\overline{q}(\varphi + \pi) \end{array} \right\} = \frac{1}{2\pi} \int\limits_0^{\pi} \overline{q}(\varphi)\left(1 - (-1)^n\right) e^{-jn\varphi} d\varphi = \left\{ \begin{array}{l} 0, \; n \; even \\ \neq 0, \; n \; odd \end{array} \right.$$

Since c_n is zero when n is even it follows that both a_n and b_n is zero when n is even.

The proof of case 3) follows from the observation that each polarity of $\overline{q}(\varphi)$ can be treated independently of the other and written as the sum of an odd function, $u(\varphi)$ and an even function, $g(\varphi)$, Figure 4.2. Furthermore, $u(\varphi)$ has the property of case 4) and yields that $a_n = 0$ for all n and $b_n = 0$ for all even n. The even function $g(\varphi)$ has $b_n = 0$ for all n. Additionally, $g(\varphi) = g(\varphi+\pi)$ which in a way similar to the proof for case 3) yields that a_n and is zero when n is odd. Finally, the properties of case 4) is the combined properties of $u(\varphi)$ and $g(\varphi)$.
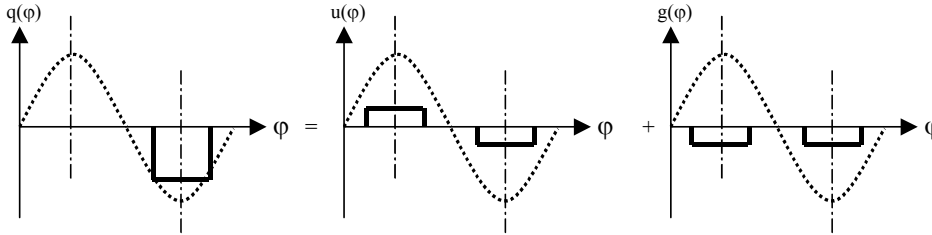

Figure 4.2 Separation of $\overline{q}(\varphi)$ into an odd and even function.

Three different situations will be demonstrated in the following sections, i.e. corona discharges from a point-plane gap, corona discharges from two reversed point-plane gaps and discharges in an artificial cavity.

4.4   Point-plane gap

The point-plane gap is the canonical geometry for studying partial discharges in a non-uniform field, i.e. corona discharges, and is extensively discussed in the literature, see for example Kuffel et al [1], Nasser [37] or Loeb [56].

In this section the geometry with the point at high potential and the plate at ground will be used as a demonstration of case 3 in Table 4.1 above.

At rising point potential corona discharges will first appear at negative polarity. These discharges are commonly referred to as Trichel pulses [37] and are of a constant magnitude and a high repetition rate. The repetition rate increase with voltage magnitude and the corona current is therefore maximum at the negative voltage peak. The corona discharges are symmetrically distributed in phase around the negative peak of the applied voltage and is a consequence of that no accumulation of space charge remains in the gap after a time much shorter than the applied voltage period. With increasing voltage magnitude the point-plane gap may enter different modes of both positive and negative discharges [37]. However, this demonstration is restricted to voltage amplitudes were pure Trichel pulses appear.

The point-plane gap used is schematically illustrated in Figure 4.3 a). The point is a needle with a tip-radius around 50 μm and is 10 mm above the grounded plane. The average discharge current $\bar{q}(\varphi)$ acquired with the PRPDA system after the application of an alternating voltage with a magnitude of 2.8 kV (less than 10 % above the inception voltage) and frequency 40 Hz is shown in Figure 4.3 b). $\bar{q}(\varphi)$ has the well-recognised symmetric distribution around the negative voltage peak. The charge shown in Figure 4.3 a) is measured in series with a coupling capacitor and the sign has been reversed to yield the same sign as the current measured in series with the point-plane gap, Figure 4.4 a).
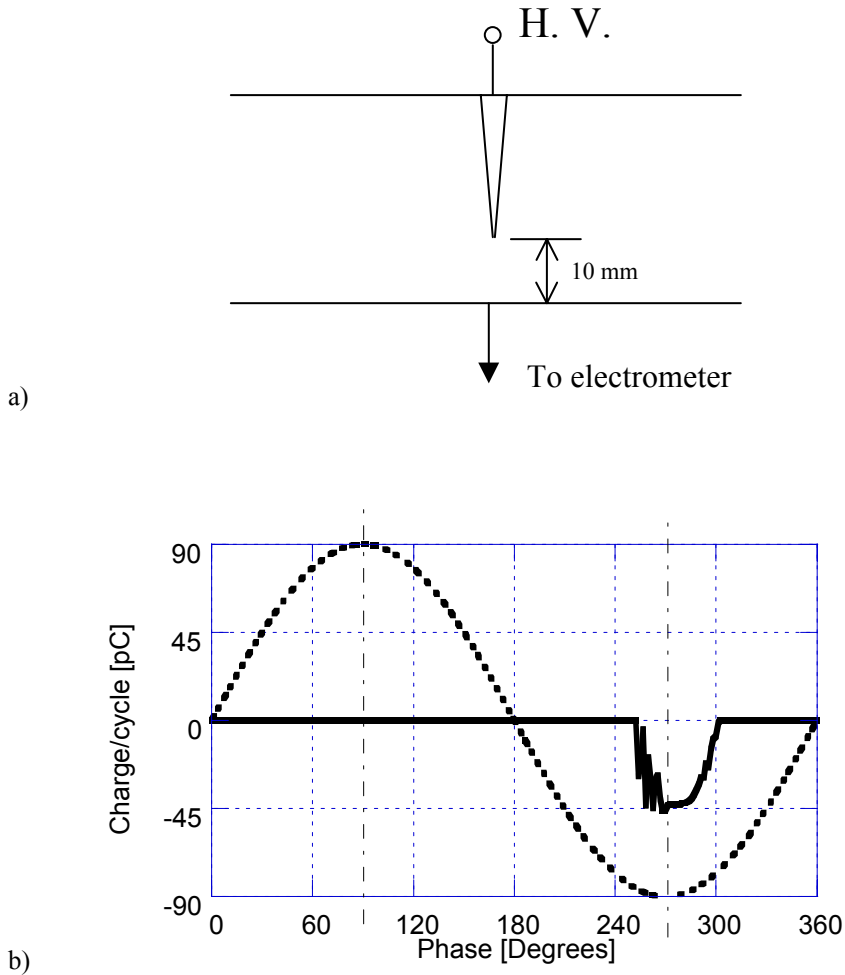
a)

b)

Figure 4.3 a)Point-plane gap with the point on high potential. Point-plane distance = 10 mm b) $\overline{q}(\varphi)$ obtained with the PRPDA system, V = 2.8 kV$_{peak}$ and f = 40 Hz.

The corona current simultaneously measured with the dielectric spectroscopy system as with the acquired PRPD data is shown in Figure 4.4 a). The data has been compensated for the ramping output of the electrometer due to the unipolar charge transport. Moreover, the current has been presented as the charge *dq* within the time-interval *dt*, i.e. *dq = i(t)dt*, where *dt* in time corresponds to one channel *dφ* in phase, as for the PRPD data shown in Figure 4.3 b).
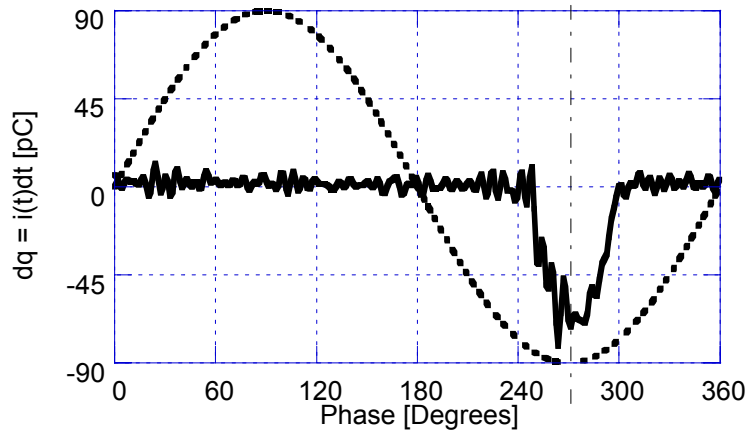
a)
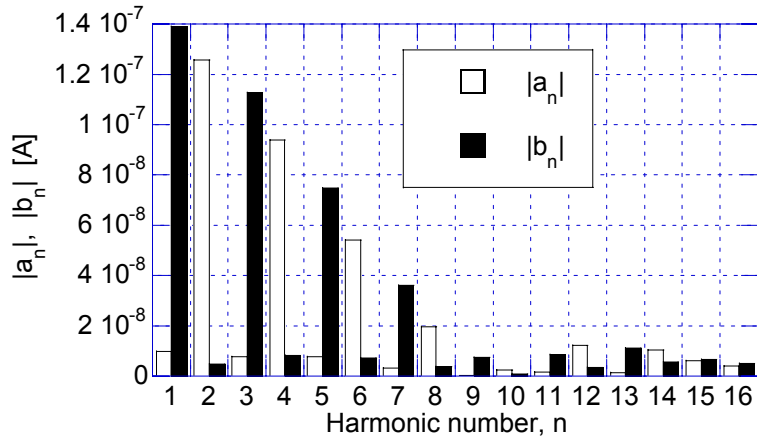
b)

Figure 4.4 a) The point-plane corona current measured with dielectric spectroscopy. b) The first 16 Fourier coefficients, a_1, b_1, ..., a_{16}, b_{16} of the current.

The absolute values of the first 16 Fourier coefficients of the corona current are shown in Figure 4.4 b). The behaviour is that all a_n with an odd index n and all b_n with an even index n are small, i.e. zero in theory. This is consistent with the relations developed for case 3 in Table 4.1 Features of $\bar{q}(\varphi)$ directly obtained from the Fourier coefficients above. The special case $a_1 = 0$ imply that no contribution enters in the apparent capacitance.

4.5   Two reversed point-plane gaps

An object with two point-plane gaps similar to the one shown in Figure 4.3 a), but with the points on opposite polarity is shown in Figure 4.5 a). This object behaves similarly on positive and negative polarity, and $\bar{q}(\varphi)$ becomes an odd function around origin (case 1), symmetric around the peaks of the applied voltage (case 3) and has the similarity property of case 4. $\bar{q}(\varphi)$ measured with the PRPDA system is shown in Figure 4.5 b) and the polarity independence and similarity properties are apparent.

The same current is simultaneously measured with the dielectric spectroscopy system and the result is shown in Figure 4.6 a). The dielectric spectroscopy current is the current after the out-balancing of the capacitive current. The current has been presented as the charge *dq* within the time interval *dt* in the same way as described in section 4.4.

The resemblance is good between the phase resolved PD current presented in Figure 4.5 b) and the same current measured with dielectric spectroscopy, Figure 4.6 a).

The basic features of the harmonics can be obtained from any of the two representations of the PD-current. However, here they have been taken from the dielectric spectroscopy current and are shown in Figure 4.6 b). It is clearly seen that the b_n components dominate, which is consistent with the odd functionality, case 1 in Table 4.1. In addition, the existence of mainly the odd harmonics, i.e. *n = 1, 3, 5, ...*, is caused by the symmetry between the two polarities, case 4 in Table 4.1. The b_1 component is the fundamental component of the PD-current in phase with the applied voltage and yields that only the apparent dielectric loss will be influenced.
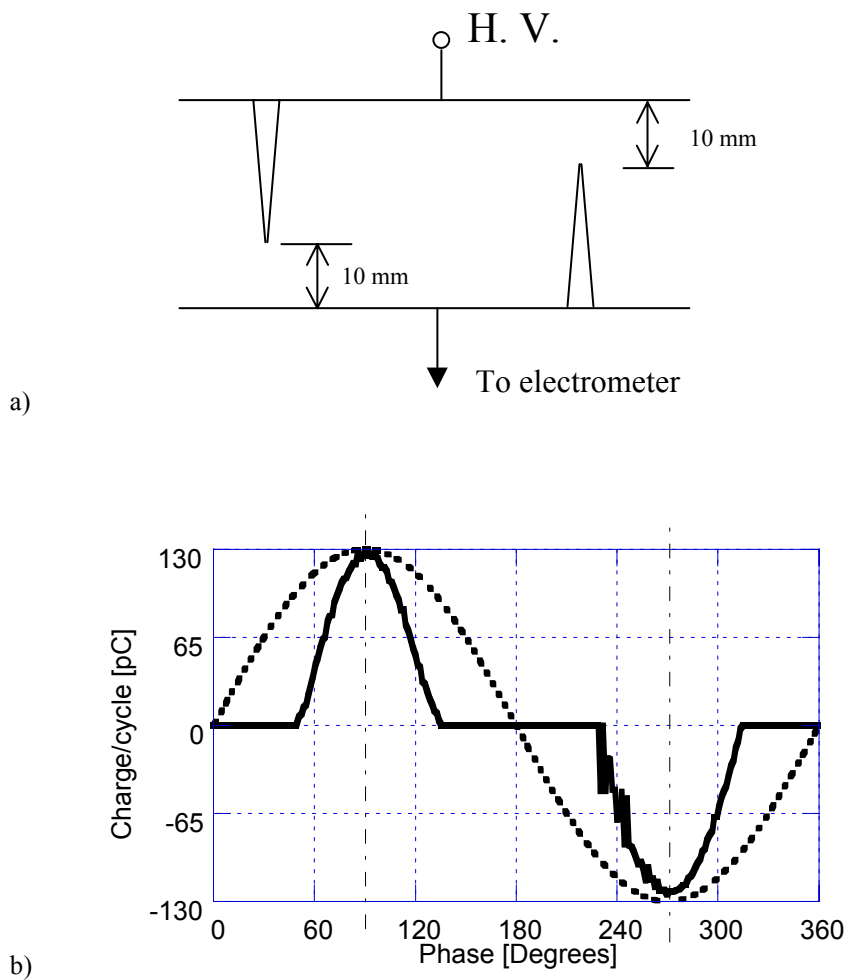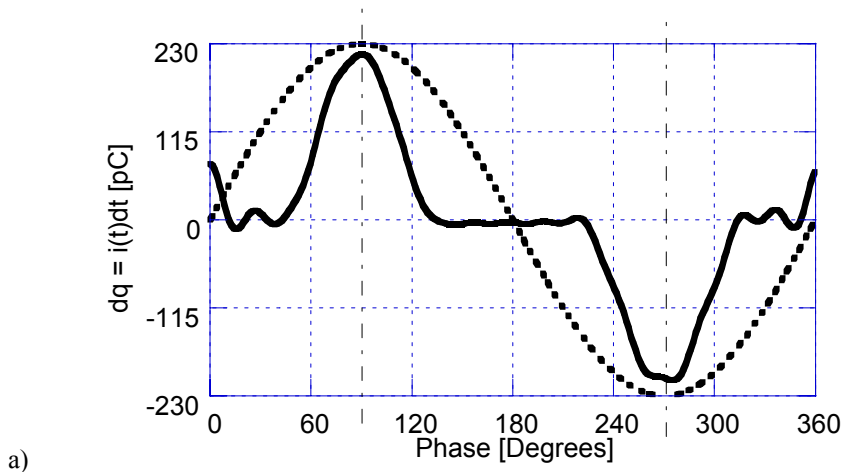
a)

b)

Figure 4.5 a)Two needle corona gap, one on each electrode. Distance between needle-tip and plate = 10 mm. b) $\bar{q}(\varphi)$ obtained with the PRPDA system at 3.5 kV$_{peak}$ and 60 Hz.

a)
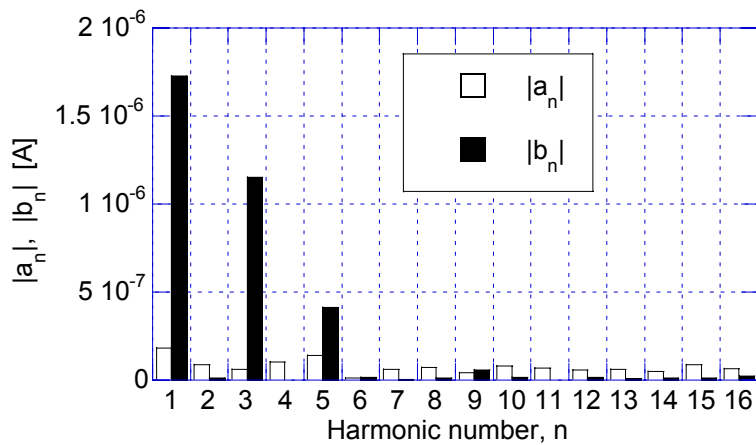
b)

Figure 4.6 a) The two-needle corona current measured with dielectric spectroscopy. b) The first 16 Fourier coefficients, $a_1, b_1, ..., a_{16}, b_{16}$ of the current.

4.6   Artificial cavity

An artificial cavity has been constructed as a punched hole in the middle of a three-layer laminate of polyethylene. The laminate was mounted between two stainless-steel electrodes and the whole arrangement has been cast in epoxy, see Figure 4.7 a). $\bar{q}(\varphi)$ acquired with the PRPDA system at 6 kV_{peak} and 40 Hz is shown in Figure 4.7 b). The PD-current simultaneously measured with the PRPDA data is shown in Figure 4.8 a); the current is

presented as charge, as explained in section 4.4. The absolute values of the Fourier coefficients are shown in Figure 4.8 b).

The same information can in principle be given by the two systems. However, the dielectric spectroscopy current is affected by a small remaining displacement current that has not been out-balanced.

The fundamental current component a_1 is larger than b_1, which is a consequence of that the charge distribution is located more to the zero-crossings than towards the peaks of the applied voltage. Hence, the PD-current contribution to the apparent capacitance will be larger than to the apparent loss.

The higher harmonics are dominated by the odd harmonics; this is due to the close similarity between the discharging polarities and is consistent with case 4 in Table 4.1.

a)
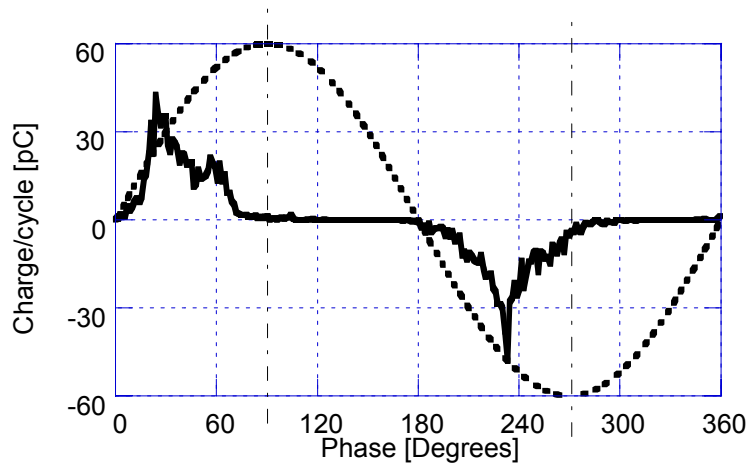
b)

Figure 4.7 a) An artificial cavity between three layers of PE (polyethylene). b) $\bar{q}(\varphi)$ obtained with the PRPDA system at 6 kV_{peak} and 40 Hz.

a)

b)

Figure 4.8 a) The PD-current from the artificial cavity measured with dielectric spectroscopy. b) The first 16 Fourier coefficients, a_1, b_1, ..., a_{16}, b_{16} of the current.
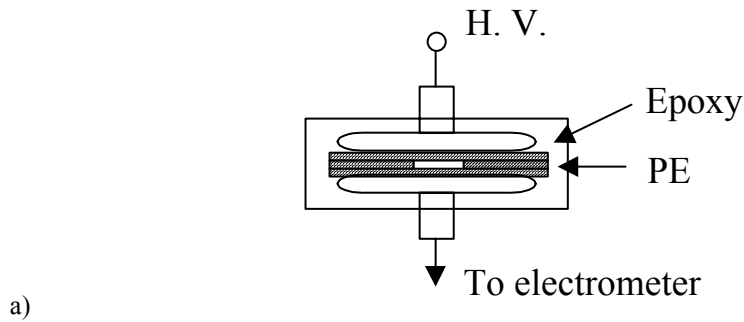
5 Statistical analysis of PRPDA data

5.1 Introduction

In this chapter, the measures that are used to quantify the partial discharge activity are defined and treated.

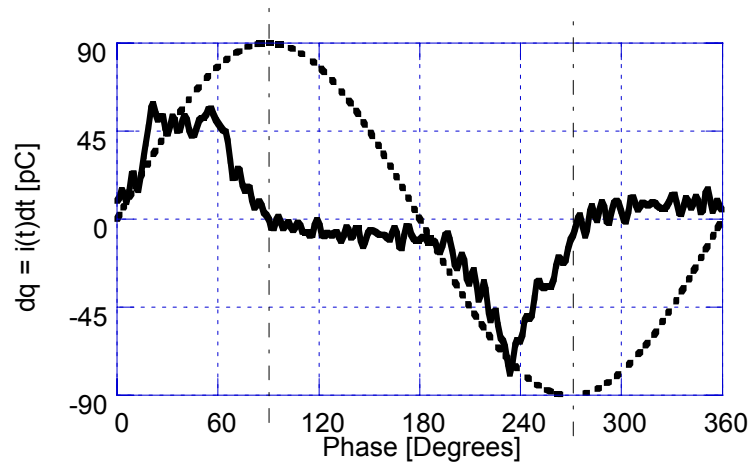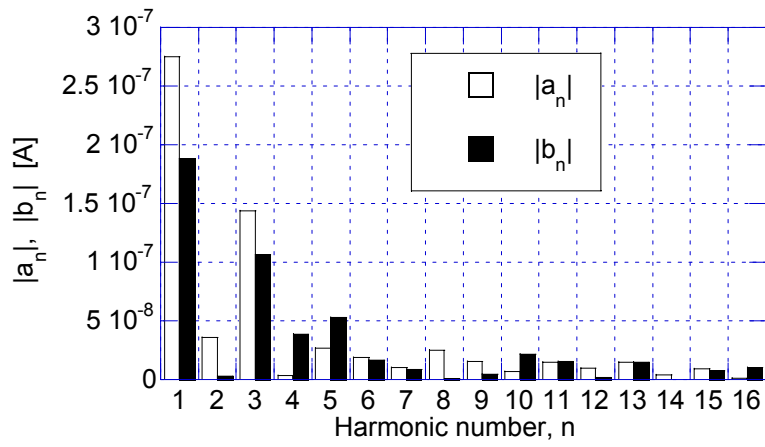All measures given are considered to be dependent on the applied voltage frequency and magnitude.

The first type of measures are the integral measures like total charge per cycle, total number of discharges per cycle, average discharge magnitude, maximum discharge magnitude, etc.

From the PD-patterns (φ-q-n patterns) it is possible to obtain two types of (1-dimensional) distributions, i.e. phase- and magnitude-distributions. The phase distributions resolve the applied voltage phase dependency of the discharge activity without any distinction made to the scatter in magnitude of individual pulses. The magnitude distribution considers the distribution of discharge magnitudes without any correlation to the phase of occurrence.

Different PD-patterns possess different properties that might be typical for a certain type of defect. The differences in the corresponding phase distributions are used in the literature as a tool to discern between different discharge sources, see Kreuger et al [39]. These authors made use of the statistical moments (called statistical operators) to measure different properties of the phase distributions. The statistical moments used in this thesis are the mean, the standard deviation, the skewness and the kurtosis. One feature of the statistical moments is that they are only dependent on the relative magnitude of the discharges. This feature is of interest in the area of recognition of different defects since the measured PD-magnitude is often less useful due to calibration errors, defect location, different insulation system, etc.

The phase distributions used are often separated in two halves with respect to the applied voltage polarity, e.g. by Gulski [57]. However, it is observed in this project [58, 59, 60] that the moments derived from distributions separated by voltage polarity are very sensitive to the discharge activity close to the zero-voltage over-crossings. Therefore, in this project, the separation of the phase distributions is made with respect to discharge polarity and not to applied voltage polarity.

The magnitude distributions could in principle be subjected to a statistical analysis similar to the phase distributions. However, the quantitative analysis is here restricted to the mean discharge magnitude. The frequency dependence of magnitude distributions has previously been studied by Miller and Black [18].

In Chapter 4 it is shown how the average partial discharge current measured with PRPDA appears in a dielectric spectroscopy measurement. The link between the two methods is a Fourier series expansion of the PD current, where the Fourier coefficients can be computed from the average phase resolved PD current. The Fourier coefficients and the moments are derived from the same phase distribution and are therefore different measures of the same distribution. An algorithm is developed that yield a direct way to compute the moments from the Fourier coefficients and vice versa. Furthermore, the information given by a certain number of moments and a certain number of Fourier coefficients are illuminated by comparing reconstructed curves.

5.2 Basic quantities

The basic quantities of a single number that are used in this thesis to quantify the PD activity are listed below.

Q_{Tot} - Total charge per cycle without respect to discharge polarity [C],

$$Q_{Tot} = \frac{1}{N_P} \sum_{i=1}^{256} \sum_{j=1}^{256} \left| q_j n(\varphi_i, q_j) \right| \tag{5.1}$$

Q_{Tot}^+, total positive charge per cycle and Q_{Tot}^-, total negative charge per cycle are defined as (5.1), but by summing over only the positive and negative discharges respectively.

N_{Tot} - Total number of discharges per cycle without respect to discharge polarity [-],

$$N_{Tot} = \frac{1}{N_P} \sum_{i=1}^{256} \sum_{j=1}^{256} n(\varphi_i, q_j) \tag{5.2}$$

N_{Tot}^+, total number of positive discharges per cycle and N_{Tot}^-, total number of negative discharges per cycle are defined as (5.2), but by summing over only the positive and negative discharges respectively.

$\overline{Q}$ - Average (mean) discharge magnitude [C],

$$\overline{Q} = \frac{Q_{Tot}}{N_{Tot}} \tag{5.3}$$

The expressions for $\overline{Q}^+$, the average positive discharge magnitude and $\overline{Q}^-$, the average negative discharge magnitude are similar to (5.3).

Q_{Max} - Maximum discharge magnitude [C],

$$Q_{Max} = \max_{i,j} \left(|q_j(\varphi_i)| \mid n(\varphi_i, q_j) \neq 0 \right) \tag{5.4}$$

The maximum positive discharge magnitude Q_{Max}^+ and the maximum negative discharge magnitude Q_{Max}^- are defined as (5.4) by restricting the maximum search to positive and negative discharge polarity respectively.

5.3 Phase distributions

Four different phase distributions are commonly defined [57], where each distribution may be divided into two different distributions, either with respect to applied voltage polarity [57] or with respect to discharge polarity if possible [59, 61]. Following Gulskis notations [57] the following phase distributions are defined:

$H_{qs}(\varphi)$ - Charge per cycle vs. phase distribution (discharge amount distribution) [C],

$$H_{qs}(\varphi_i) = \frac{1}{N_P} \sum_{j=1}^{256} q_j n(\varphi_i, q_j) \tag{5.5}$$

$H_n(\varphi)$ - Number of pulses per cycle vs. phase distribution (pulse count distribution) [-],

$$H_n(\varphi_i) = \frac{1}{N_P} \sum_{j=1}^{256} n(\varphi_i, q_j) \tag{5.6}$$

$H_{qn}(\varphi)$ - Mean charge vs. phase distribution (mean pulse height distribution) [C],

which are derived from the previous distributions,

$$H_{qn}(\varphi_i) = \frac{H_{qs}(\varphi_i)}{H_n(\varphi_i)} \tag{5.7}$$

$H_{qm}(\varphi)$ - Maximum charge vs. phase distribution (maximum pulse height distribution) [C],

$$H_{qm}(\varphi_i) = \max_{j} \left(|q_j(\varphi_i)| \mid n(\varphi_i, q_j) \neq 0 \right) \cdot \text{sgn}\left(q_j(\varphi_i) \right) \tag{5.8}$$

In principle it is possible to define many more phase-distributions by using different discrimination levels. For example one could study the phase distribution of discharges between two levels, q_1 and q_2, $q_2 > q_1$ or all discharges above q_1 or below q_2. The distributions could also be studied as a function of the discrimination levels. Nevertheless, thousands of distributions could be defined in this way, but in this thesis only a Low Level Discrimination (LLD) will is used, which is set for the ICM-system when performing the

measurements, but an additional LLD may be used in the post-processing of the acquired data if required.

The four phase distributions defined are here shown for a PD-pattern, Figure 5.1, obtained for artificial voids in a cable-like structure, here called the cable-model. $H_{qs}(\varphi)$, $H_n(\varphi)$, $H_{qn}(\varphi)$ and $H_{qm}(\varphi)$ that are derived from the pattern are shown in Figure 5.2 a) - d).
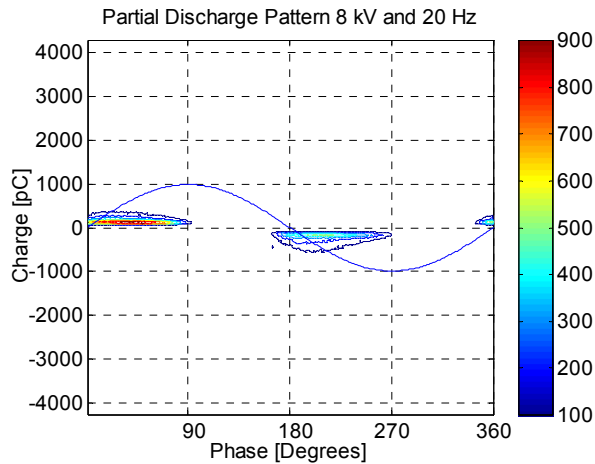

Figure 5.1 PD-pattern obtained for a cable-model at 8 kV and 20 Hz.

The H_{qs} distribution indicates that the main discharge activity occur during rising voltages, which is also shown in H_n. Further, there seems to be a greater amount of charge during negative polarity than during positive. The reason for this could be that a large amount of small discharges under positive voltage polarity are discriminated by the LLD.

The H_{qn} distribution are given as the quote of H_{qs} and H_n, and as seen in Figure 5.2 c) this distribution is not limited to the rising part of the voltage but also to the decaying parts. This behaviour occurs because this is the mean value of the discharges at a given phase, and if there are a few or many discharges do not influence H_{qn}. Gulski [57] frequently makes use of this distribution in his classification method, together with the H_n distribution. However, it might be questionable to what extent H_{qn} is a good distribution for further analysis or not. Because the very few discharges that in this example occurs between 90° - 150°, and 270° - 330° are weighted up to a level equal the main discharge activity that occurs in the phase intervals 0° - 90°, 150° - 270° and 330° - 360°.

The H_{qm} distribution has its maximum close to the voltage peaks; however, it becomes saturated for the few largest negative discharges.

40
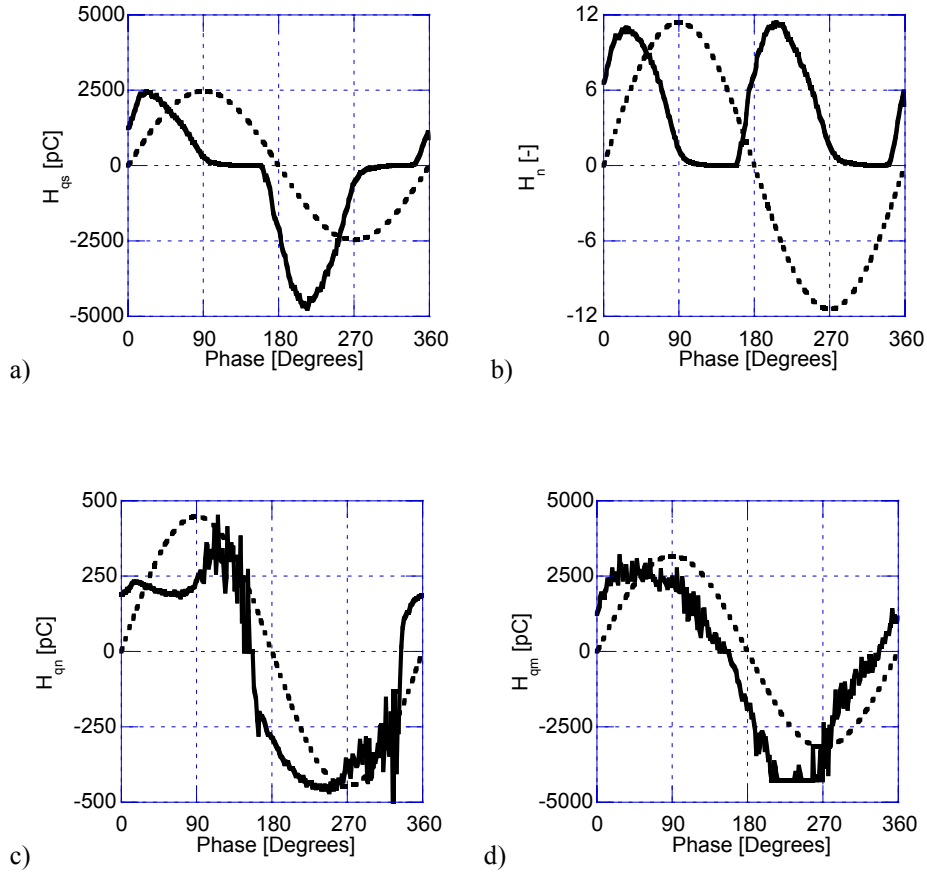
Figure 5.2 a) - d) H_{qs}, H_n, H_{qn} and H_{qm} vs. phase, obtained for a cable model at 8 kV and 20 Hz.

5.3.1 Separating distributions with respect to voltage- and discharge-polarity

The phase distributions defined may be analysed as statistical distributions if the polarity of the discharges is neglected, i.e. taking the absolute value of H_{qs}, H_{qn} and H_{qm}. However, it has become practice [39] to separate the distributions into two different distributions with respect to applied voltage polarity. The distributions obtained in this way are denoted as $H_{qs}^{V+}(\varphi)$, $H_{qs}^{V-}(\varphi)$, $H_n^{V+}(\varphi)$, $H_n^{V-}(\varphi)$, etc., where the super-script notation V+ or V- indicate the applied voltage polarity.

41

However, this method is very sensitive to small changes of the discharge activity around the zero-crossings, Figure 5.3. Thus, by separating the total phase distribution with respect to the applied voltage polarity the obtained distributions may contain discharges of both positive and negative polarity. This method is not recommended, because parameters derived from the distributions will become very sensitive to small (unessential) changes of the discharge activity around the zero-crossings. Instead, if possible, two distributions that contain discharges of only positive and negative discharge polarity are defined. The obtained distributions are denoted as $H_{qs}^{PD+}(\varphi), H_{qs}^{PD-}(\varphi), H_{n}^{PD+}(\varphi), H_{n}^{PD-}(\varphi)$, etc., where PD+ and PD- indicate the partial discharge polarity. This distinction between applied voltage polarity and discharge polarity is also used by Okamoto and Tanaka [61].
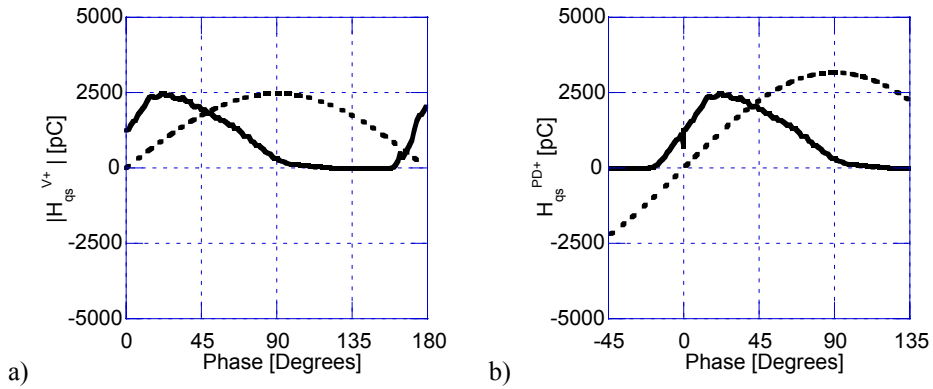

a)   b)

Figure 5.3 A comparison between a) $\left|H_{qs}^{V+}(\varphi)\right|$ *and b)* $H_{qs}^{PD+}(\varphi)$ *obtained from* $H_{qs}(\varphi)$ *in Figure 5.2 a.*

5.3.2 Algorithm for separating distributions with respect to discharge polarity

There are several algorithms that can be used for breaking a phase distribution like $H_{qs}(\varphi)$ into two distributions, one for positive discharges and one for negative discharges. The applicability of the selected algorithm will depend strongly on the pattern, in particular if there is a lot of noise present. However, the algorithm presented here is stable for most of the experimental data presented in this thesis, for example for the cable-model and the stator bar.

The presented algorithm differs from the algorithm used in previous work [58, 59]. In [58, 59] an algorithm that determined a breakpoint between the positive and negative discharges is worked out. This breakpoint is determined from the largest phase-gap with no discharge activity. In general the results presented here differs only slightly from the results in [58, 59].

The present algorithm use a phase window of 180° (128 channels) width and is shifted one channel forward at a time. The total charge within the phase window is computed in each step. The distribution of positive discharges is finally the part of $H_{qs}(\varphi)$ that contains the maximum amount of positive charge and the remaining part is the phase distribution of negative discharges. In Figure 5.4, $H_{qs}(\varphi)$ obtained for a stator bar at 9 kV and 100 Hz is shown, together with the distributions obtained that contain the maximum amount of positive and negative charge, i.e. $H_{qs}^{PD+}(\varphi)$ and $H_{qs}^{PD-}(\varphi)$.
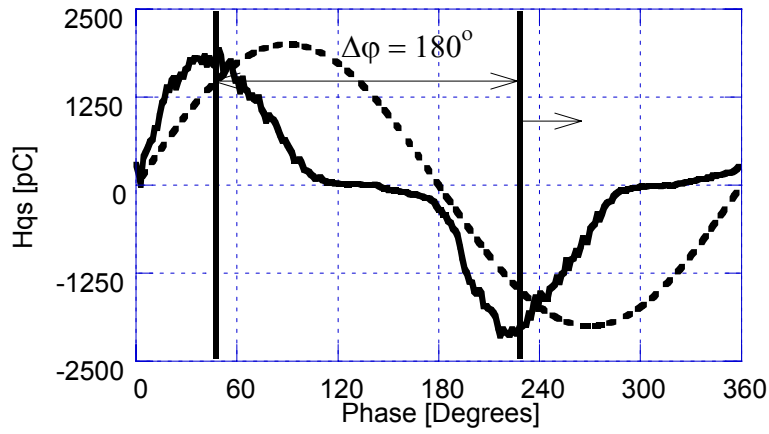
a)
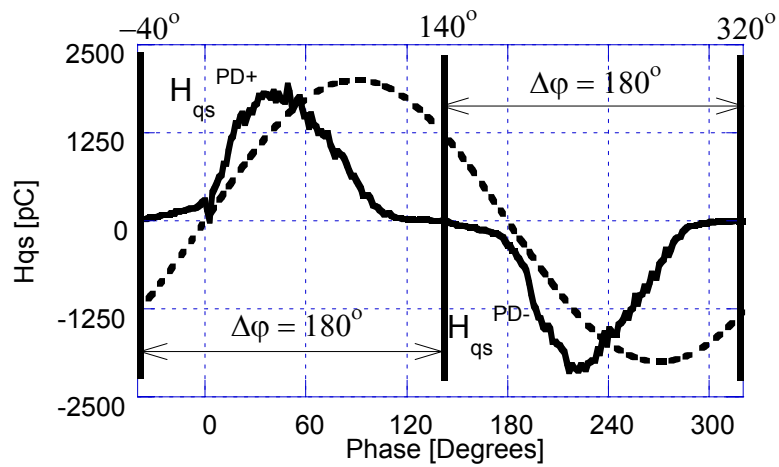
b)

Figure 5.4 The phase distribution of charge, $H_{qs}(\varphi)$. a) The distribution as it normally is shown, together with a moving phase window of 180 degrees width. b) The distribution shown when positive discharges under negative applied voltage polarity have been wrapped -360 degrees. The indicated distributions are the obtained $H_{qs}^{PD+}(\varphi)$ and $H_{qs}^{PD-}(\varphi)$.

5.4 Magnitude distributions

The magnitude distributions are defined as:

$N_q^+(q)$ - Number of positive discharges vs. charge magnitude [-],

$$N_q^+(q_j) = \sum_{i=1}^{256} n(\varphi_i, q_j), 129 \le j \le 256 \qquad (5.9)$$

$N_q^-(q)$ - Number of negative discharges vs. charge magnitude [-],

$$N_q^-(q_j) = \sum_{i=1}^{256} n(\varphi_i, q_j), 1 \le j \le 128 \qquad (5.10)$$

In principle all discharges of each polarity are included in these distributions, but one could for example use magnitude discrimination levels even here. Another approach could be to study the magnitude distributions for only a certain phase interval, $\varphi_1 \le \varphi \le \varphi_2$. Nevertheless, the magnitude distributions in this thesis is confined to the above defined. The magnitude distributions corresponding to the PD-pattern in Figure 5.1 are shown in Figure 5.5 a) and b).
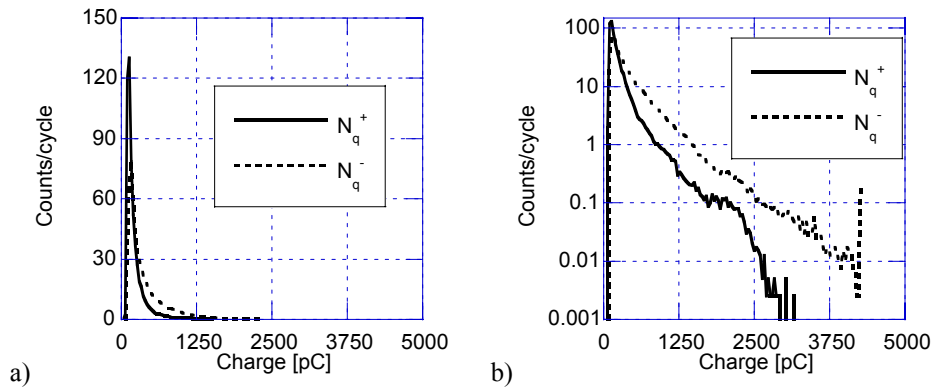
Figure 5.5 Magnitude distributions obtained from the PD-pattern in Figure 5.1, a) Linear scale and b) Logarithmic scale on ordinate axis.

The larger discharges are very few to the number, so few that a logarithmic scale is required to resolve them. The saturation of the negative discharges is apparent. However, the distributions show that the main discharge activity comes from the small discharges.

The measure used to quantify the magnitude distributions is the mean discharge magnitude.

$\overline{Q}^{\pm}$ - mean discharge magnitude of positive and negative discharges respectively [C],

$$\overline{Q}^{\pm} = \frac{\sum_j q_j N_q^{\pm}(q)}{\sum_j N_q^{\pm}(q)} \qquad (5.11)$$

Where the summations are taken over the index j for the appropriate polarity respectively.

5.5 Quantifying phase distributions with statistical moments

Even if the PD-pattern, and the phase- and magnitude-distributions, contain the essential information that can be obtained with the PRPDA - technique it is often fruitful to quantify some important features of the distributions. The list of parameters that could be used could be made long and some of the basic measures have already been given in section 5.2. The measures adopted here are the statistical moments used to quantify statistical distributions [62]. The use of statistical moments to quantify the phase-resolved distributions was early adopted by Tanaka and Okamoto [61], who concerned the skewness (defined below) of the phase-distributions. The idea of the statistical moments (operators) was later adopted by Kreuger et al in the work [39] on recognising different PD-defects by their differing phase-distributions.

The statistical operators are applicable on all distributions mentioned in section 5.3. However, the absolute values must be taken for distributions with negative sign. Furthermore, all distributions are normalised in such a way that their sum is equal to one (5.12), i.e. forming a probability distribution.

$$h(\varphi_i) = \frac{|H(\varphi_i)|}{\sum_i |H(\varphi_i)|} \qquad (5.12)$$

$H(\varphi_i)$ in (5.12) is any of the distributions defined in section 5.3, and i is taking over the interval where the distribution is defined.

The *standard moments*, m_k of order k of a discrete distribution $h(\varphi_i)$ are defined as:

$$m_k = \sum_i \varphi_i^k h(\varphi_i) \qquad (5.13)$$

The first moment, m_1, is the mean value of the distribution and represents the centroid in a mechanical analogy.

$$m_1 = \sum_i \varphi_i h(\varphi_i) \qquad (5.14)$$

Standard moments, accept the mean, are rarely used in practical applications but are sometimes useful in theoretical developments [62]. The moments often used in practice are the central moments, i.e. the moments around the mean,

$$\mu_k = \sum_i (\varphi_i - m_1)^k h(\varphi_i) \qquad (5.15)$$

The second moment, μ_2 is the variance, equal to the square of the standard deviation, σ_{std}. However, the variance is the common parameter in Gulskis analysis [57], but in this thesis the standard deviation is preferred, since it has a less dynamic range and is a more apparent measure of the width of the distribution, since it is directly scaled in phase units (degrees or radians).

$$\sigma_{std} = \sqrt{\mu_2} = \sqrt{\sum_i (\varphi_i - m_1)^2 h(\varphi_i)} \qquad (5.16)$$

The moments of order three and four are less well known, but have found its place in the PD literature, as they are measures of the skewness and the sharpness of distributions.

The skewness is dimensionless and defined as the third central moment divided with the cube of the standard deviation,

$$Sk = \frac{\mu_3}{\sigma_{std}^3} \qquad (5.17)$$

$Sk > 0$ indicates that the distribution has a "tail" to the right of its mean, and oppositely for $Sk < 0$, i.e. a tail to the left. The sign property of the skewness is demonstrated in Figure 5.6 for two similar, but reversed triangular distributions.
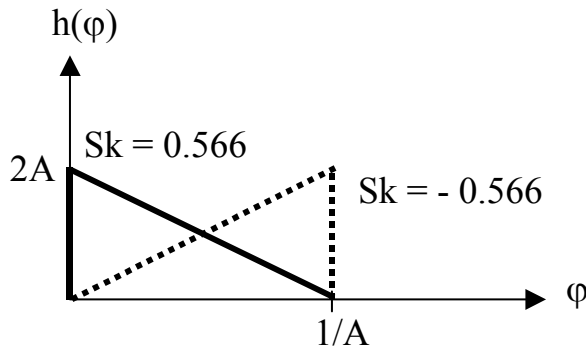

Figure 5.6 Two triangular distributions with the same shape but turned in opposite directions, which yield skewness of equal magnitude but different sign.

The kurtosis is dimensionless and is defined as the fourth central moment divided with the quadruple of the standard deviation, and with a consecutive subtraction of three.

$$Ku = \frac{\mu_4}{\sigma_{std}^4} - 3 \tag{5.18}$$

The subtraction of 3 comes from a comparison with the normal distribution, which has $\mu_4 = 3\sigma_{std}^4$ thus, a kurtosis equal to zero. The kurtosis (called excess in [62]) is a measure of the sharpness of the distribution, compared to a normal distribution. If $Ku > 0$ the distribution is said to be sharper than a normal distribution around the mean and if $Ku < 0$ it is flatter.

Moments of an order higher than four are rarely used other than for more mathematical applications [63]. However, the higher central moments of an odd order are further measures of asymmetry, and the higher even central moments are further measures of sharpness or similar.

The statistical moments are in this thesis only applied on the distribution defined for discharges of positive and negative polarity. The actual discharge polarity is indicated with super-scripts like m_1^{PD+}, m_1^{PD-}, σ_{std}^{PD+}, σ_{std}^{PD-}, etc.

5.5.1 The relation between the standard and central moments

The central moments of order k can be computed from the standard moments of order $\leq k$. The expression is obtained by expanding the factor $(\varphi - m_1)^k$ in (5.15) with the binomial theorem [50] and changing order between the sums. Hence,

$$
\begin{aligned}
\mu_k &= \sum_i (\varphi_i - m_1)^k h(\varphi_i) = \sum_i \sum_{p=0}^{k} \binom{k}{p}(-1)^p m_1^p \varphi_i^{k-p} h(\varphi_i) = \\
&= \sum_{p=0}^{k} \left(\frac{k!}{p!(k-p)!} \cdot (-1)^p m_1^p \sum_i \varphi_i^{k-p} h(\varphi_i) \right) = \\
&= \sum_{p=0}^{k} \left(\frac{k!}{p!(k-p)!} \cdot (-1)^p m_1^p m_{k-p} \right)
\end{aligned}
\tag{5.19}
$$

The standard moments of order $k \geq 2$ are in a similar way obtained from the mean value, m_1 and the central moments of order $\leq k$, thus

$$m_k = \sum_{p=0}^{k} \binom{k}{p} m_1^k \mu_{k-p} = \sum_{p=0}^{k} \frac{k!}{p!(k-p)!} m_1^k \mu_{k-p} \tag{5.20}$$

5.6 The relation between statistical moments and Fourier coefficients

5.6.1 From Fourier coefficients to statistical moments

It has been shown in Chapter 4 that the Fourier coefficients in the Fourier series expansion of the average phase resolved PD-current, $\overline{q}(\varphi) = H_{qs}(\varphi)$ directly reflect some features of the PD-activity. The Fourier coefficients contain information that reflects the type of defect. The statistical moments are used with the same intentions; i.e. they could be used as parameters for classification of discharge type [39].

In this section, the theoretical link between the Fourier coefficients and the statistical moments is derived. The relation is intended for the $H_{qs}(\varphi) = \overline{q}(\varphi)$ distribution because the Fourier coefficients of this distribution can be measured with dielectric spectroscopy, but in principle the relation holds for any distribution.

In the following the distributions are treated as continuous, but the analogy to the discrete situation is straightforward.

The normalised distribution $h_{qs}(\varphi)$ is expanded in a Fourier series,

$$h_{qs}(\varphi) = \frac{a_0}{2} + \sum_{n=1}^{\infty} \left(a_n \cos(n\varphi) + b_n \sin(n\varphi) \right) \tag{5.21}$$

Since $h_{qs}(\varphi)$ in general contain discharges of both positive and negative polarity the distribution must be separated into two parts, for example in the way described in section 5.3.2.

Assume that $h_{qs}(\varphi)$ is naturally separated into two parts with a constant sign within each interval, i.e.

$$\begin{aligned} h_{qs}^{+}(\varphi) &= h_{qs}(\varphi) > 0, \quad \varphi_{+}^{\min} < \varphi < \varphi_{+}^{\max} \\ h_{qs}^{-}(\varphi) &= -h_{qs}(\varphi) > 0, \quad \varphi_{-}^{\min} < \varphi < \varphi_{-}^{\max} \end{aligned}, \tag{5.22}$$

where it is understood that $\varphi_{+}^{\max} = \varphi_{-}^{\min}$.

The moments computed for a given interval is then computed directly on the Fourier series. For the mean, m_1,

$$m_1^\pm = \int\limits_{\varphi_\pm^{\min}}^{\varphi_\pm^{\max}} \varphi h_{qs}^\pm(\varphi)d\varphi = \pm\left[\frac{a_0}{2}\int\limits_{\varphi_\pm^{\min}}^{\varphi_\pm^{\max}}\varphi d\varphi + \sum_{n=1}^{\infty}\left(a_n\int\limits_{\varphi_\pm^{\min}}^{\varphi_\pm^{\max}}\varphi\cos(n\varphi)d\varphi + b_n\int\limits_{\varphi_\pm^{\min}}^{\varphi_\pm^{\max}}\varphi\sin(n\varphi)d\varphi\right)\right] \quad (5.23)$$

The integrals in (5.23) are the mean values of $\cos(n\varphi)$ and $\sin(n\varphi)$ and are only dependent on the integration interval.

The following notations are introduced for the standard moments of the trigonometric functions:

$$\alpha_{kn}^\pm = \int\limits_{\varphi_{\min}^\pm}^{\varphi_{\max}^\pm}\varphi^k\cos(n\varphi)d\varphi \quad (5.24)$$

and

$$\beta_{kn}^\pm = \int\limits_{\varphi_{\min}^\pm}^{\varphi_{\max}^\pm}\varphi^k\sin(n\varphi)d\varphi \quad (5.25)$$

With (5.24) and (5.25) equation (5.23) is simplified to

$$m_1^\pm = \pm\left[\frac{a_0}{2}\alpha_{10}^\pm + \sum_{n=1}^{\infty}\left(a_n\alpha_{1n}^\pm + b_n\beta_{1n}^\pm\right)\right] \quad (5.26)$$

The higher central moments are computed in a similar way,

$$\mu_k^\pm = \int\limits_{\varphi_\pm^{\min}}^{\varphi_\pm^{\max}}\left(\varphi - m_1^\pm\right)^k h_{qs}^\pm(\varphi)d\varphi =$$

$$= \sum_{p=0}^{k}\left((-1)^p\binom{k}{p}m_1^{\pm p}\int\limits_{\varphi_\pm^{\min}}^{\varphi_\pm^{\max}}\varphi^{k-p}h_{qs}^\pm(\varphi)d\varphi\right) =$$

$$= \pm\sum_{p=0}^{k}\left((-1)^p\frac{k!}{p!(k-p)!}m_1^{\pm p}\left(\frac{a_0}{2}\int\limits_{\varphi_\pm^{\min}}^{\varphi_\pm^{\max}}\varphi^{k-p}d\varphi + \sum_{n=1}^{\infty}\left(a_n\int\limits_{\varphi_\pm^{\max}}^{\varphi_\pm^{\max}}\varphi^{k-p}\cos(n\varphi)d\varphi + b_n\int\limits_{\varphi_\pm^{\min}}^{\varphi_\pm^{\max}}\varphi^{k-p}\sin(n\varphi)d\varphi\right)\right)\right)$$

$$(5.27)$$

This final statement is condensed by using (5.24) and (5.25),

$$\mu_k^\pm = \pm \sum_{p=0}^{k} \left((-1)^p \frac{k!}{p!(k-p)!} m_1^{\pm p} \left(\frac{a_0}{2} \alpha_{(k-p)0}^\pm + \sum_{n=1}^{\infty} \left(a_n \alpha_{(k-p)n}^\pm + b_n \beta_{(k-p)n}^\pm \right) \right) \right)$$ (5.28)

5.6.2   From statistical moments to harmonics

The inverse problem, i.e. to find a relation between the harmonics and the statistical moments has at least two solutions. A numerical solution can be obtained by using (5.27) and (5.28) and expressing the equations in matrix form. In principle the equation system obtained has infinite dimension, i.e. a single moment is dependent on all harmonics and vice versa. However, an approximative solution is possible to obtain by truncating the matrix after a certain number of moments.

A more direct attempt is to start with the Fourier integrals that give the Fourier coefficients and performing a Maclaurin expansion of the trigonometric functions. The next step is to reverse the order of summation and integration. The result is a sum that contains the standard moments of $h_{qs}(\varphi)$.

$$a_n = \frac{1}{\pi} \int_{\varphi_+^{\min}}^{\varphi_-^{\max}} h_{qs}(\varphi) \cos(n\varphi) d\varphi = \frac{1}{\pi} \int_{\varphi_+^{\min}}^{\varphi_-^{\max}} h_{qs}(\varphi) \sum_{k=0}^{\infty} (-1)^k \frac{(n\varphi)^{2k}}{(2k)!} d\varphi =$$

$$= \frac{1}{\pi} \sum_{k=0}^{\infty} \left(\frac{(-1)^k n^{2k}}{(2k)!} \int_{\varphi_+^{\min}}^{\varphi_-^{\max}} \varphi^{2k} h_{qs}(\varphi) d\varphi \right)$$ (5.29)

and

$$b_n = \frac{1}{\pi} \int_{\varphi_+^{\min}}^{\varphi_-^{\max}} h_{qs}(\varphi) \sin(n\varphi) d\varphi = \frac{1}{\pi} \sum_{k=0}^{\infty} \left(\frac{(-1)^k n^{2k+1}}{(2k+1)!} \int_{\varphi_+^{\min}}^{\varphi_-^{\max}} \varphi^{2k+1} h_{qs}(\varphi) d\varphi \right)$$ (5.30)

$h_{qs}(\varphi)$ is both positive and negative and the integrals in (5.29) and (5.30) must be separated into two parts, one for each polarity,

$$a_n = \frac{1}{\pi} \sum_{k=0}^{\infty} \left(\frac{(-1)^k n^{2k}}{(2k)!} \left(\int_{\varphi_+^{\min}}^{\varphi_+^{\max}} \varphi^{2k} h_{qs}^+(\varphi) d\varphi - \int_{\varphi_-^{\min}}^{\varphi_-^{\max}} \varphi^{2k} h_{qs}^-(\varphi) d\varphi \right) \right) =$$

$$= \frac{1}{\pi} \sum_{k=0}^{\infty} \left((-1)^k n^{2k} \left(\sum_{p=0}^{2k} \frac{1}{p!(2k-p)!} \left(m_1^{+2k} \mu_{2k-p}^+ - m_1^{-2k} \mu_{2k-p}^- \right) \right) \right)$$ (5.31)

and similarly for b_n,

$$b_n = \frac{1}{\pi} \sum_{k=0}^{\infty} \left((-1)^k \, n^{2k+1} \left(\sum_{p=0}^{2k+1} \frac{1}{p!(2k+1-p)!} \left(m_1^{+2k+1} \mu_{2k+1-p}^{+} - m_1^{-2k+1} \mu_{2k+1-p}^{-} \right) \right) \right) \tag{5.32}$$

The standard moments in (5.31) are replaced by the central moments with the relation (5.20).

This method works, in principle, but the rate of convergence is severely bad, in particular for higher harmonics, and is not useful in practice because the number of moments required to yield a reasonable good estimation of a_n and b_n is too large. For example, the artificial distribution $H(\varphi) = \sin(\varphi) + (1/3) \cdot \sin(3\varphi) + (1/5) \cdot \sin(5\varphi) + (1/7) \cdot \sin(7\varphi)$ is shown in Figure 5.7 a), and the relative error of b_1, b_3 and b_5 computed by () is shown as a function of the order of moments used. The relative error increase dramatic in the beginning but converges finally to a reasonable error. However, for b_7 the error grows too fast that the computer can not handle the numbers.
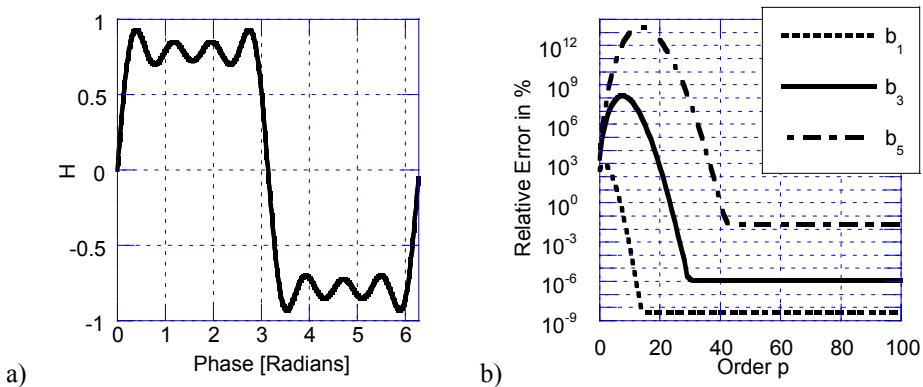

Figure 5.7 a) $H(\varphi) = \sin(\varphi) + (1/3) \cdot \sin(3\varphi) + (1/5) \cdot \sin(5\varphi) + (1/7) \cdot \sin(7\varphi)$ *b) The relative error of b_1, b_3 and b_5 in per-cent as a function of the order of moments included.*

5.6.3 Reconstruction of distributions from the moments

The reconstruction of a distribution from the Fourier coefficients is straightforward; it is the summation of the Fourier series (5.21) with the Fourier coefficients inserted. This procedure is straightforward because the function sequence *{cos(nφ)}* and *{sin(nφ)}* constitute a set of orthogonal base functions and the Fourier coefficients are given by orthogonality relations.

The statistical moments are not given by an orthogonality relation and as such they can not be directly used to reconstruct a distribution. One way to overcome the problem is to use relation (5.23) and (5.28) in matrix form and solving for the Fourier coefficients and

performing the summation (5.21). Another approach is presented here makes use of the orthogonal Legendre polynomials [50, p. 230].

The reconstruction method is presented as a demonstration and not as a complete theory.

The standard representation of the Legendre polynomials, $P_n(x)$, $n = 0, 1, 2, 3, ...$ is defined on the interval $-1 \leq x \leq 1$, but can in principle be modified to any other interval by suitable substitutions.

A continuous function $h(x)$ may be expanded in a series of Legendre polynomials,

$$h(x) = \sum_{n=0}^{\infty} c_n P_n(x) \tag{5.33}$$

The Legendre coefficients, c_n are given from the orthogonality relation [50, p.230],

$$c_n = \frac{\int_{-1}^{1} h(x) P_n(x) dx}{\int_{-1}^{1} P_n^2(x) dx} = \frac{2n+1}{2} \cdot \int_{-1}^{1} h(x) P_n(x) dx \tag{5.34}$$

The explicit expression of the Legendre polynomials is a sum [50, p.230],

$$P_n(x) = 2^{-n} \sum_{k=0}^{[n/2]} (-1)^k \binom{n}{k} \cdot \binom{2n-2k}{n} \cdot x^{n-2k}, \ n = 0, 1, 2, ..., \tag{5.35}$$

where first four are,

$$P_0(x) = 1, \ P_1(x) = x, \ P_2(x) = (3x^2 - 1)/2, \ P_3(x) = (5x^3 - 3x)/2, ... \tag{5.36}$$

The c_n:s are obtained by (5.34). For c_3 the integral yields,

$$c_3 = \frac{7}{2} \cdot \int_{-1}^{1} h(x) P_3(x) dx = \frac{7}{2} \cdot \int_{-1}^{1} h(x)(5x^3 - 3x)/2 dx =$$

$$= \frac{7}{2} \cdot \frac{1}{2}\left(5\left(m_3^+ + m_3^-\right) - 3\left(m_1^+ + m_1^-\right)\right) \tag{5.37}$$

In the last expression in (5.37) it is recognised that the integral can be expressed by the standard moments. Two moments are used, one for positive x values and one for negative. Although, this is not generally required in a pure mathematical application, and is merely used to connect the moments to the two discharge (or voltage) polarities for a PD-distribution.

The generalization of (5.37) to c_n is straightforward (5.38) and it becomes clear that all c_n, n odd, can be calculated from the n first odd standard moments, m_n, and when n is even, c_n can be calculated from the n first even standard moments. The standard moments can be achieved from the central moments by (5.20) if required.

$$c_n = (2n+1)2^{-n-1} \sum_{k=0}^{[n/2]} (-1)^k \binom{n}{k} \cdot \binom{2n-2k}{n} \cdot \left(m_{n-2k}^+ + m_{n-2k}^- \right), n = 0, 1, 2, ... \qquad (5.38)$$

Example: The standard moments for the distribution $h(x) = sin(\pi x)$ is computed and used in the reconstruction algorithm, (5.33) with (5.38). The reconstructed curve with the knowledge of two, four and six moments of each polarity is shown in Figure 5.8. The reconstructed curve with four moments is almost perfect, whereas the straight line achieved with 2 moments just yields a trend.
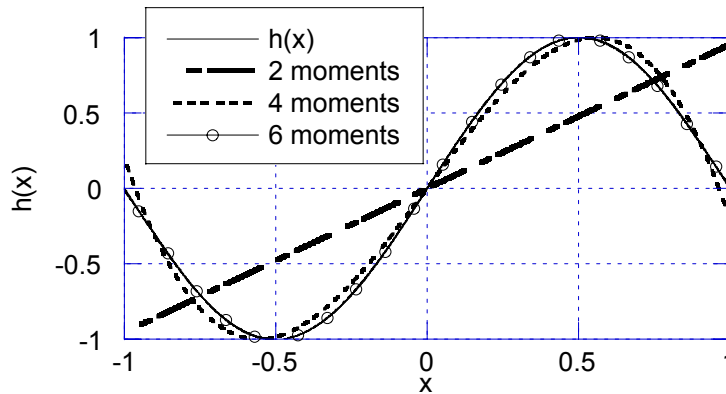

Figure 5.8 The distribution $h(x) = sin(\pi x)$ reconstructed with the knowledge of the first 2, 4 or 6 statistical moments of each polarity.

6 Measurement systems

6.1 Introduction

Two methods for investigating the activity of PDs in PD infested objects has been used in these investigations, namely Phase Resolved Partial Discharge Analysis (PRPDA) and Dielectric Spectroscopy (DS). The main contributions made in this project is first a PRPDA system that can measure with variable frequency in the range 1 mHz to 400 Hz and secondly that the Variable Frequency-PRPDA (VF-PRPDA) system is combined with a dielectric spectroscopy system in order to simultaneously perform acquisition of PD-pulses and measure the apparent dielectric response current through the test-object. The apparent dielectric response current is the sum of the linear dielectric response current and the partial discharge current.

For the PRPDA measurements the commercial ICM (Insulation Condition Monitoring) system [13] have been used that allow PRPDA measurements in the frequency range 30 - 400 Hz. However, the development of a new software and modifying the synchronising signal extended the frequency range to now covering 1 mHz - 400 Hz [60]. The present chapter starts with a description of the basic principles of electrical detection of PD pulses and of the foundations of PRPDA. Next follows a description of the existing VF-PRPDA system, with special emphasis on the modifications performed.

Dielectric Spectroscopy (DS) has been extensively used as a measure for insulating quality [46], and the application of DS on PD infested systems has mainly been used for investigating the voltage dependence of the loss-tangent, tan-δ at high-voltages. It is often believed that an increase in tan-δ with voltage (often named "tan-δ tip-up") is due to inception of PDs. A measure of the insulation quality is then the magnitude of the tip-up. However, the approach here is to measure the total current composed of polarisation currents, loss-currents, and PD-pulses.

The system for dielectric spectroscopy has been developed by the author and by Mrs. Giddens Herbig [60]. It contains both physical parts and achieved knowledge from dielectric spectroscopy systems developed in previous projects at KTH, see e.g. [64, 4, 65]. However, the software is completely new and differs from previous versions in many ways, the basic difference is that the applied voltage and the integrated current are sampled and all samples for all applied cycles are stored for post-processing. The stored waveforms can be post-analysed by for example Fourier analysis; this yields both the apparent capacitance and loss, but also the harmonics of the fundamental component. Storing of data for all acquired cycles yields that a temporal analysis of the stochastic PD-current can be performed.

Finally, the PRPDA system and the Dielectric Spectroscopy system have been merged together in order to measure PRPDA and Dielectric Spectroscopy simultaneously [52]. This

is a new and fruitful concept that allows a direct comparison of PD-current contribution to the non-linear part of the apparent dielectric response current.

6.2 Survey of measurement systems

The complete measurement system for simultaneous measurements of VF-PRPDA and dielectric spectroscopy is composed of the high-voltage system, the VF-PRPDA system and the dielectric spectroscopy system. The VF-PRPDA system was developed first and the dielectric spectroscopy system was developed and incorporated at a later stage.

A schematic diagram of the measurement system and its components is shown in Figure 6.1. A block-diagram of the system and the control equipment is shown in Figure 6.2 and a photo of the experimental setup in the laboratory is shown in Figure 6.3.

The measurement system is composed of three parts, i.e. the high-voltage system, the PD-detection system and the dielectric spectroscopy system. The details of each part will be given in the following sections of this chapter and in [52].

When a partial discharge occur in the test object C_T the charge is drawn from the coupling capacitor C_K and generates a voltage impulse across the detection impedance, Z_{Det}. If the filter impedance, Z_{Filt} is high and the stray capacitance is negligible, then the same charge is measured by the electrometer in the dielectric spectroscopy system. However, the PD current impulse is filtered by the balancing capacitor, C_B and the protection resistance, R_P before the actual integration by the electrometer. If only PD-measurements are performed, the point S (Summation point), may be solidly grounded. Alternatively, the detection impedance Z_{Det} may be located in this point rather than in series with the coupling capacitor.

The dielectric spectroscopy system is designed to measure the apparent dielectric response current of C_T. The dielectric response current is for most insulation systems completely dominated by the capacitive (displacement) current and is balanced out by a current of equal magnitude but with reversed polarity. The balancing current is generated by an inverted voltage in phase with the applied voltage and applied across the balancing capacitor C_B. The current remaining after balancing is integrated to a measurable voltage by an electrometer.
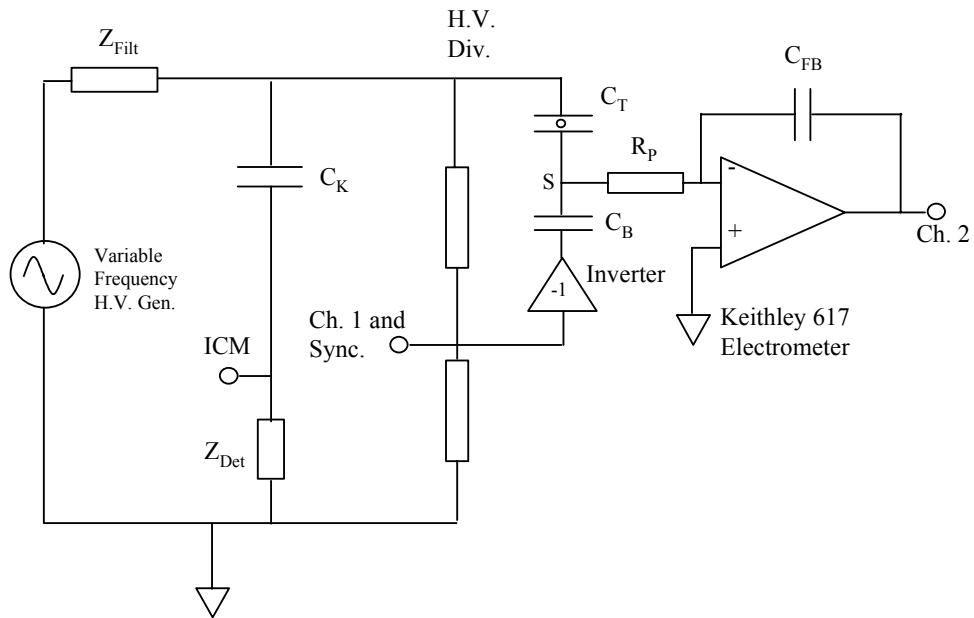
Figure 6.1 The measurement system for simultaneous measurement of VF-PRPDA and dielectric spectroscopy.

The block-diagram in Figure 6.2 shows how different units in the measurement system are connected to each other. Some of the units can be visually identified in the photos in Figure 6.3.
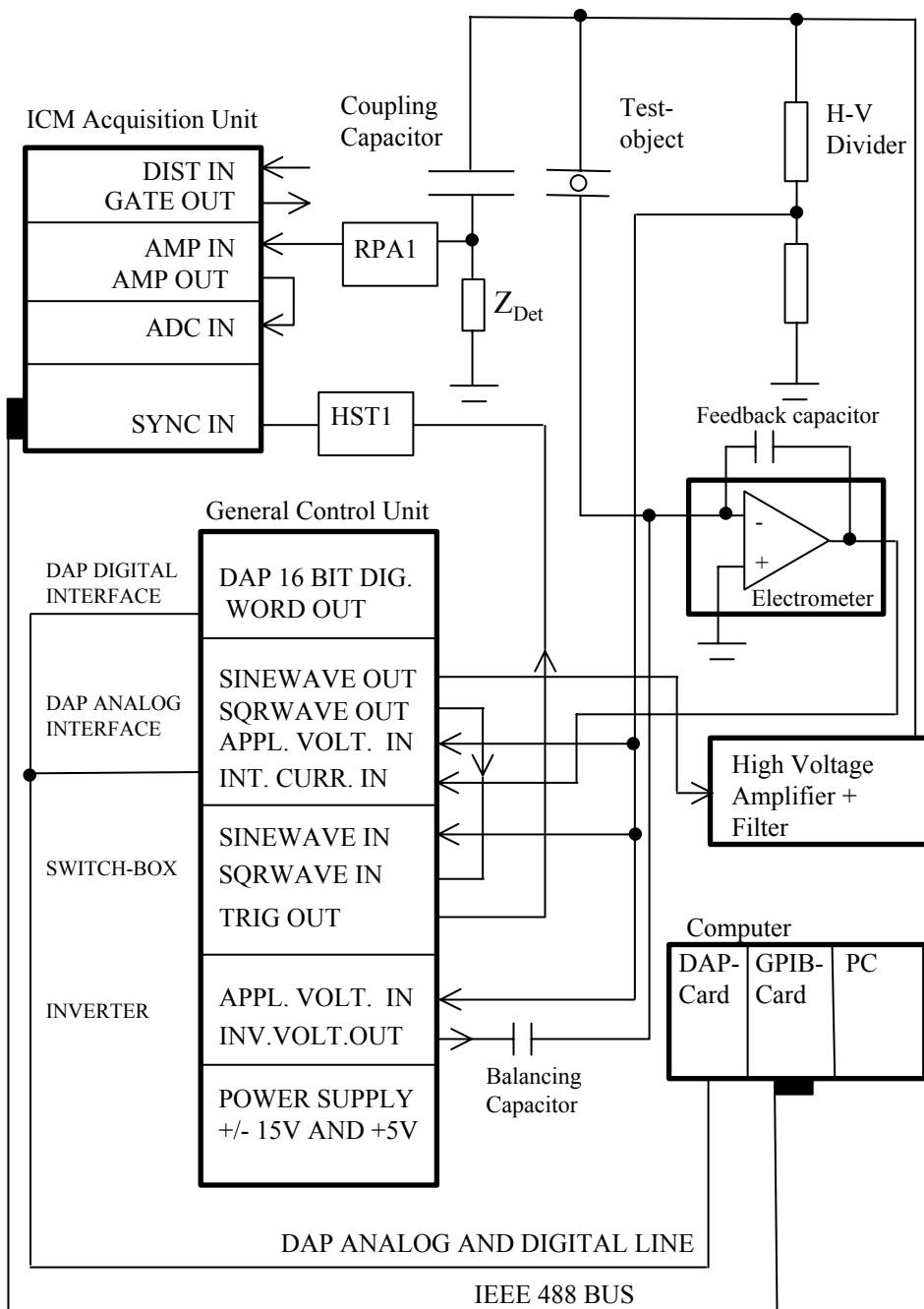
Figure 6.2 Block-diagram of measurement system for VF-PRPDA and dielectric spectroscopy.
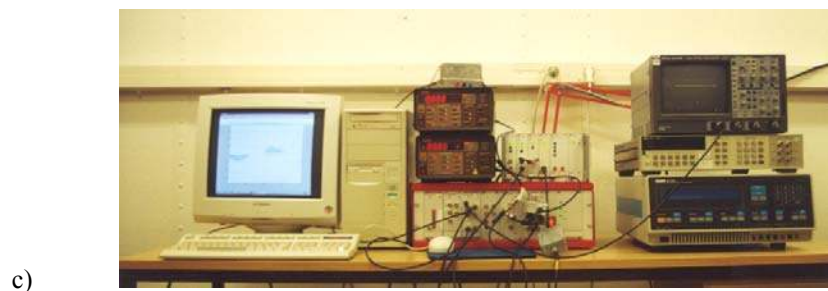
58

a)

b)

c)

Figure 6.3 a) The laboratory; the safety cage has been removed to make the equipment more visible. b) The test bench with vacuum chamber, coupling capacitor, thermostat bath, etc. c) The measuring equipment.

6.3   High-voltage system

In this section, a description of the high-voltage components used in the measurement system are given, i.e. the amplifier, the filter, the voltage divider and the coupling capacitor. The transfer function of the high-voltage system from low-voltage input to high-voltage output is measured. The transfer function yields the highest frequency where the phase-shift from input to output is so small that the PRPD measurement system can be synchronised with the input low-voltage signal and not with the signal from the high-voltage divider as required at high frequencies.

HV-amplifier:

The AC high voltage used has been generated by synthesised low-voltage signal and amplified by a TREK 20/20 High-Voltage Amplifier, which has the specifications given in Table 6.1 [66].

Table 6.1 Specifications of TREK 20/20 High-Voltage Amplifier

Property	Specification
Input voltage range	0 to $\pm$ 10V$_{peak}$
Output voltage range	0 to $\pm$ 20 kV$_{peak}$
Output current range	0 to $\pm$ 20 mA$_{peak}$ when operating in quadrant I or III
Gain	2000 V/V
Frequency range	0 to 15 kHz (3 dB)

HV-Filter: The TREK HV-amplifier operates with switched DC aggregates and the switching frequency for the TREK is 50 kHz, which is a harmful frequency since it is within the 6 dB band-width limit for the amplifiers in the ICM, and it will completely destroy any high-sensitivity measurements. A high-voltage filter of low-pass type was designed to reduce the 50 kHz noise, and to exclude the influences from PDs in the TREK when testing above ~ 12 kV. The filter, see Figure 6.4, is designed in three stages, where the first stage is connected directly to the output of the H.V. amplifier, and the output is connected to the test-object, the coupling-capacitor and the high-voltage divider.
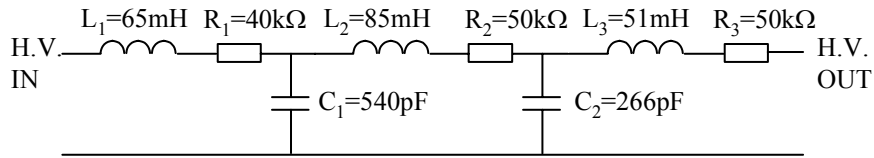
Figure 6.4 High-voltage low-pass filter

The 3 dB cut-off frequency of the filter depends on the capacitive load, i.e. the coupling capacitor, the test-object and the supply cable. The gain (damping) and phase-shift of the H.V. filter have been measured for a low load and a high load. The measurements have been verified by a simulation of the circuit model and the measured and simulated results have been compared in Figure 6.5.
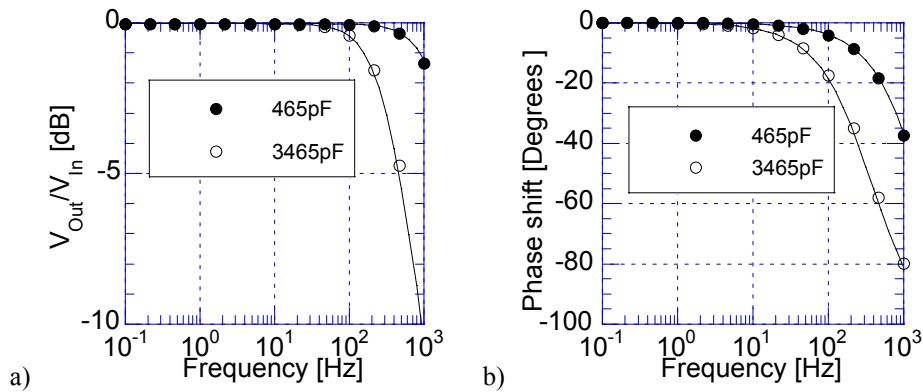

Figure 6.5 a) Amplitude and b) phase-shift for the high-voltage filter at two different capacitive loads. Solid lines are simulated curves from the circuit above, together with the voltage divider and the capacitive load at the output.

High-voltage divider: Amplitude and phase of the applied voltage across the test-object must be measured accurately because it will directly alter the accuracy of the measurements, in particular in the dielectric spectroscopy measurements. The high-voltage divider used is a resistive divider with some capacitive compensation, designed by Holmgren [2] to work over the frequency range 1 mHz - 1000 Hz. The high-voltage divider is mounted in a grounded steel barrel that serves as an equipotential surface and yields fixed stray capacitance, Figure 6.6.
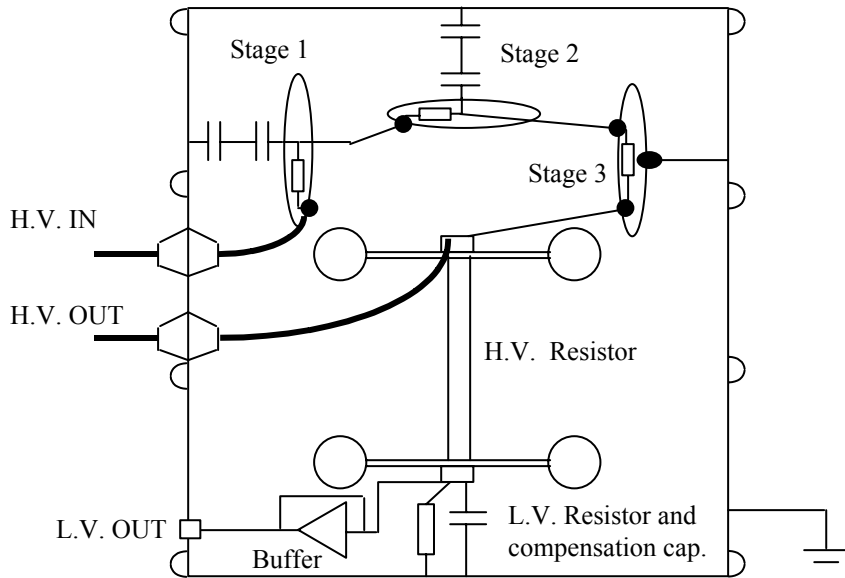
Figure 6.6 High-voltage divider and high-voltage low-pass filter mounted in a grounded steel-barrel that serves as an equipotential surface that yields fixed stray capacitance.

The frequency response of the high-voltage divider has been controlled by a Schlumberger 1250 Frequency Response Analyser, which has the facilities that it allows input voltages as high as 500 V_{peak}. The result is shown in Figure 6.7.
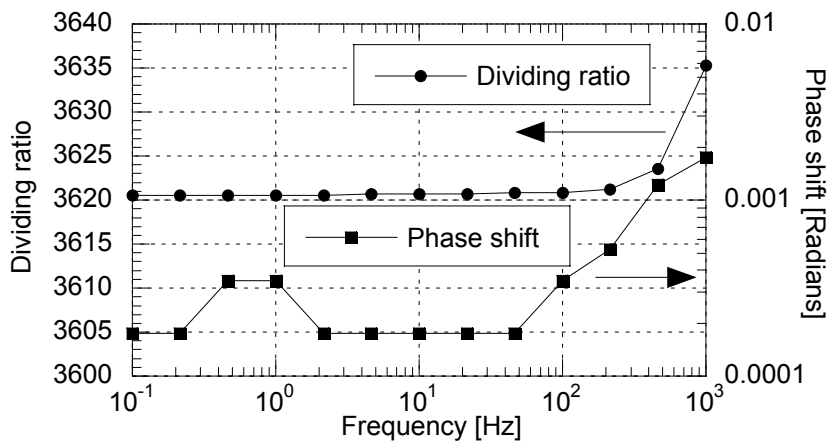

Figure 6.7 Dividing ratio and phase-shift vs. frequency for the high-voltage divider in the range 0.1 Hz - 1000 Hz.

Coupling-capacitor: Different coupling capacitors have been used depending on the test-object capacitance. Default is a pair of Hipotronics coupling capacitors of each 100 pF and designed for 25 kV_{rms}, they have in principle been used only for test-objects with a small capacitance, i.e. below 20 pF. For test-objects with a larger capacitance or when shunting has been required a combination of different ceramic LCC® capacitors have been used. Caution is required when using the LCC® capacitors because they are not PD-free up to rated voltage and series combinations are often required to achieve a PD-free coupling capacitor up to the test voltage level.

The test-object capacitance and the coupling capacitor together with the capacitance from the high-voltage supply cable will load the Trek in series with the filter. The frequency dependency of the amplitude and phase-shift from TREK input to high-voltage on test-object has been measured and simulated for two different loads and is shown in Figure 6.8. The actual gain around 500 Hz for the low-load is due to self-resonance in the system, however that situation has not occurred in practical situations.
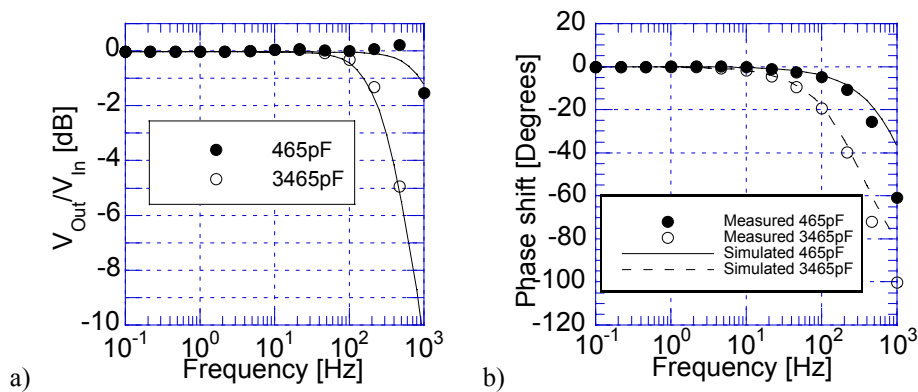

Figure 6.8 a) Amplitude response and b) phase-shift for the complete system, i.e. the HV-amplifier in series with the HV-filter and connected to the HV-divider in parallel with the test-object and the coupling capacitor.

6.4 VF-PRPDA system

6.4.1 Partial Discharge Detection

The technique adopted in this project for electrical detection of partial discharges in electrical insulation under the application of an alternating high voltage is basically a straight detection system, Figure 6.9. The many general aspects that can be put on an electrical PD detection system can be found in the literature, e.g. [35, 1, 36], and only details for the system used in this project will be given here.
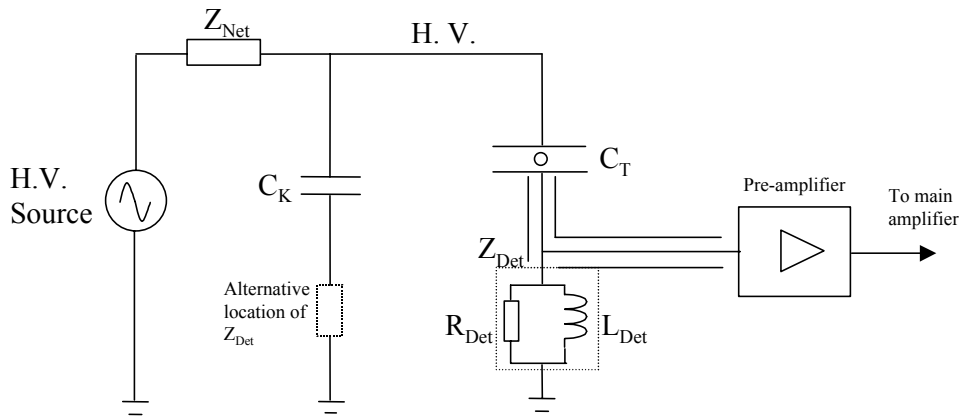
Figure 6.9 The system for straight detection of partial discharges.

The apparent charge transported in the leads to the test object C_T during the discharge is measured as the voltage impulse across a detection impedance, Z_{Det}, which in this project is composed of an inductance, L_{Det} (3.8 mH) in parallel with a resistance R_{Det} (1 kΩ). The voltage impulse is connected by means of a coaxial cable to a pre-amplifier with input impedance 10 kΩ // 50 pF. This yields an effective capacitance, C_{Det} in the detection impedance which is the sum of the coaxial cable capacitance (100 pF/m) and the input capacitance of the pre-amplifier (50 pF).

The detection impedance may be placed either directly in series with the test object or in series with the coupling capacitor, C_K. The coupling capacitor should in principle be as large as possible to ensure a low-impedance path for the PD-impulses and also keep the voltage drop across the test-object as small as possible. However, a large coupling capacitor loads the supply and should in this aspect be as small as possible. The charge seen by Z_{Det} is equally measured in series with C_K as in series with the test-object if stray capacitance can be neglected and if the impedance of the high-voltage supply network is high compared to the capacitors. However, the sign of the voltage impulse is reversed between the two branches.

6.4.2 Phase Resolved PD Detection

Phase resolved PD detection was early based on observations by an oscilloscope, where the discharges are superimposed on to the applied voltage sine-wave and displayed on an elliptical time-base [35, p.67; 67]. However, the developments of digital techniques during the 1960s and 1970s made it possible to electronically digitize and store PD data with the aid of multi-channel analysers, see e.g. [68, 69]. In principle these techniques allowed either sorting of the PD-magnitudes or counting of the numbers vs. time or phase. Additional developments during the 1980s allowed simultaneous measurement of the PD-pulse height and the time (phase) of occurrence [61], i.e. the formation of what is presently named a PD-pattern. The use of the PRPDA measurement technique from late 1980s and during the 1990s is extensive and a complete review is not attempted here. The PRPDA-

64

technique was early applied in Japan [70] together with the Cigré-II method for studying insulation ageing. Extensive work on recognition have been performed by Gulski and Kreuger [71], which can be seen as a continuation of the work in [67], but with modern techniques and data storing facilities. Applications on high voltage apparatus such as hydro generators, SF_6 insulated systems and power transformers were performed early by ABB in Switzerland [72].

The temporal evolution of partial discharges during application of a high alternating sinusoidal voltage, is here seen as sequence of pulsating discharges with magnitude q_i occurring at time t_i after the application of voltage, Figure 6.10. That pulsating discharges are considered is enhanced to make a distinction to "swarming micro partial discharges (SMPD)" [73], i.e. discharges with high repetition rate but a magnitude so small that it may be hard to detect and resolve them with the PRPDA-technique. Nevertheless, the SMPD activity is of importance because it is often seen close to breakdown of the insulation [74].

The Phase Resolved Partial Discharge Pattern (PRPDP) is obtained by sorting and counting discharges of size q_i, occurring at time t_i into a discretized two-dimensional counter array $n(\varphi_j, q_m)$ where $q_m \leq q_i < q_{m+1}$ and $\varphi_j \leq \varphi_i < \varphi_{j+1}$, where $\varphi_i = \omega t_i$. The discrete phase is reset to zero after each completed voltage cycle, with the consequence that the order in which the individual discharges occur is lost. However, that information could be useful in investigating the recurrence of discharges from, for example a single void [75], but is probably hard to apply when there are many discharge sources present discharging at the same time, like in an aged stator-bar or an old paper insulated cable.
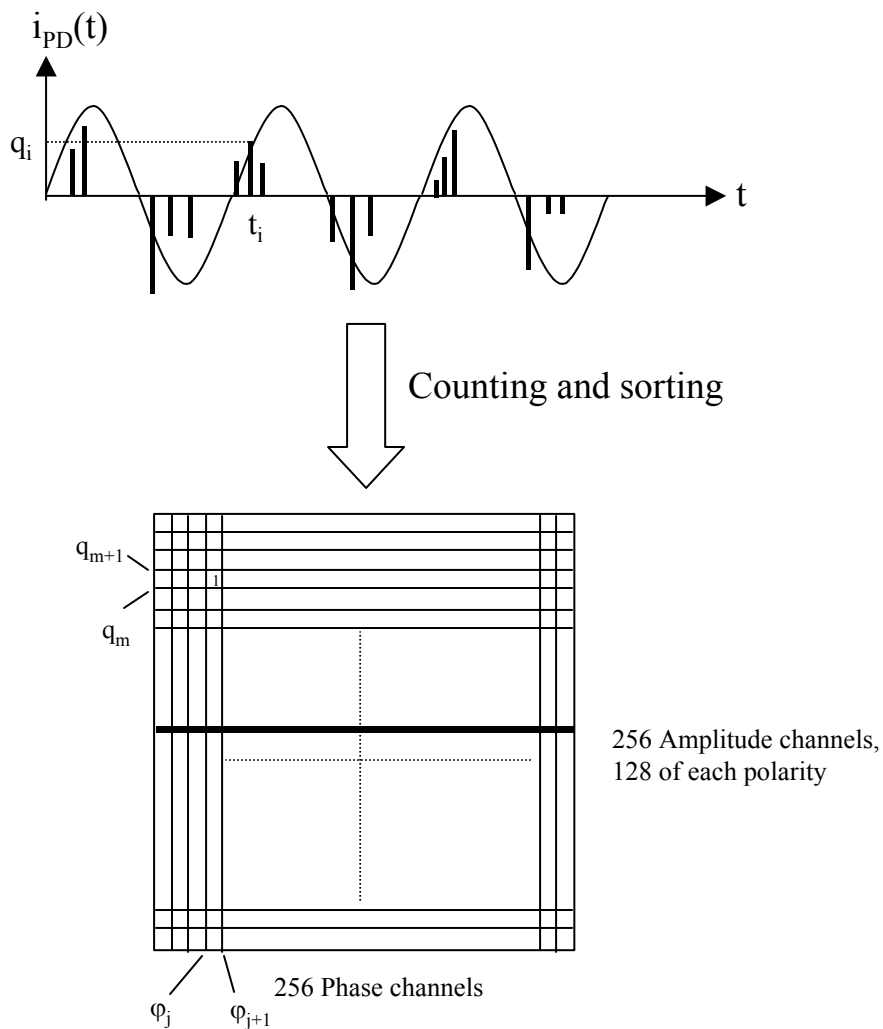
Figure 6.10 Mapping of consecutive discharges into a single voltage cycle. The phase is discretized with 256 channels and the magnitude is discretized with 256 channels, here 128 of each polarity. The numbers in the two-dimensional array are the counts of the discharges.

The final result is often presented as a φ-q-n pattern, Figure 6.11, where numbers $n(\varphi_j, q_m)$ are given as a coloured pattern where a higher intensity of red indicate more discharges of that size and in that phase position.

Figure 6.11 An example of a PD-pattern after a measurement.
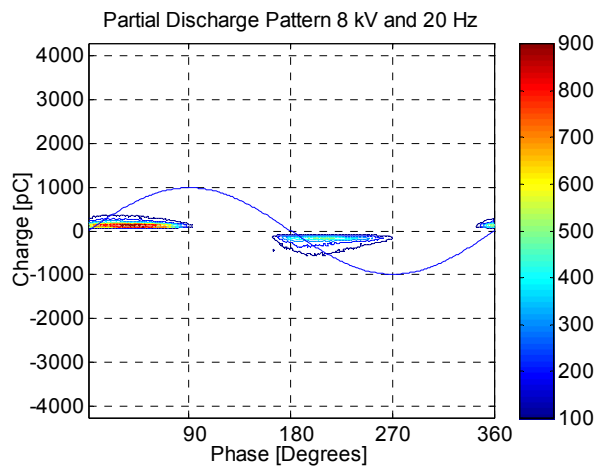
The complete three-dimensional PD-pattern is often useful for visual judgements but is harder to apply in a more quantitative analysis. However, a number of phase- and amplitude-distributions may be derived from the PD-pattern. These distributions will be frequently used in this thesis and are defined and discussed in Chapter 5.

6.4.3   The ICM System

The PRPDA system adopted for the PRPDA in this thesis is an ICM++ (Insulation Condition Monitoring) Digital Partial Discharge Acquisition System, manufactured by Power Diagnostix (*PD•*) Systems GmbH [13]. The ICM instrument has the properties presented in Table 6.2.

Table 6.2 Features of the ICM system

Property	Specification
Computer control	IEEE 488.2 instrument bus
Data storing	256 x 256 integer array with maximum 32768 counts in each cell
A/D converter	12 bit resolution
Gain	Range: 1 - 800 in steps 1, 2, 4, 8 multiplied with 1, 10 or 100
Band-pass filter	6 dB cut-off frequencies: 40, 80 or 100 kHz (LF) and 250, 600 and 800 kHz (HF)
Applied voltage frequency range	30 - 400 Hz with HST 1 voltage measure and synchronising module
Time mode	Possible to detect PD-activity vs. time, e.g. for DC voltage applications
Data storing	Binary files, *filename.dat*

The ICM system has expanded since the version used in this thesis (version 2.00) and have today the facility to measure at 0.1 Hz, but does not yet cover the full frequency range 1 mHz - 400 Hz used in this thesis. The modifications required to use the ICM system in this extended frequency range is described in the next section.

6.4.4   Extension of the frequency range towards low-frequencies

The ICM can perform phase resolved measurements in the frequency range 30 - 400 Hz, and simultaneously measure the applied voltage from a voltage divider. The divided voltage is at the same time used as a synchronising- or trigger- signal for repetition of the sweep. However, at frequencies below 30 Hz the ICM system could not operate in phase mode. The modifications required to extend the frequency range for the ICM to cover 1 mHz - 400 Hz are described in this section. The developed system for Variable Frequency - Phase Resolved Partial Discharge Analysis (VF-PRPDA) is shown as a block-diagram in Figure 6.2, and a photo of the full test-setup is shown in Figure 6.3.

The ICM system acquisition unit is controlled from a PC through a GPIB IEEE 488.2 interface, and all control commands as well as the acquired data are sent through this interface.

In order to allow control of the complete ICM system a new software for controlling and storing data was designed. The new software program was made in Borland C++ 5.02 [76] and allowed control of the ICM through GPIB commands, but also control of the DAP-card that was used as a signal generator for both the applied low-frequency sinusoidal voltage and the synchronising square-wave. The DAP-card had also a digital interface through which different devices and functions were controlled.

The first problem encountered when forcing the instrument to re-trigger below 30 Hz was to do all time-settings in the "time-mode (single-mode)" before changing to repetition mode, i.e. phase mode; this forced the instrument to repeat the measurements after each voltage period. This "trick" was an essential step forward in developing the low-frequency application.

However, the divided applied voltage could not work as a synchronising signal below 30 Hz. Instead a square-wave signal that run in phase with the applied low-voltage signal was generated simultaneously. This square-wave signal is connected directly to the input of the HST1 unit whose output is connected to the synchroniser unit of the ICM. Therefore, measuring of the applied voltage could no longer be made by the ICM. However, this sacrifice was unessential since this facility is supplied by one of the analog input-channels of the DAP. However, the HV-filter imposes a phase-shift of the applied high voltage as shown in section 6.3. This phase shift is mainly of importance at frequencies above 30 Hz, but in this frequency region the divided voltage from the high-voltage divider can be used as a synchronising signal. The signal used for synchronising is selected by an analog switch (switch-box), which is digitally controlled from the DAP-card.

Verification of the system at low frequencies was made by feeding the simple differentiating circuit in Figure 6.12 with the synchronising square-wave and voltage pulses similar to partial discharges occur in the zero-crossings of the applied voltage. In the frequency range 0.05 Hz - 400 Hz this technique worked well, with correct phase positions for the verification pulses. However, for frequencies below 0.05 Hz the pulse-pair was shifted in phase, Figure 6.13 a). The origin of this reproducible phase-shift is unclear, but a careful investigation showed that the pulse occurrence was linearly shifted in time with the applied voltage period, T, see Figure 6.13 b). A linear fit to the measured time shifts was found to be $t_{Shift} = 0.523T - 9.98$. Thus, the measurements were performed with the synchronising square-wave and acquired data were shifted afterwards by $256 \cdot t_{shift} / T$ phase channels.
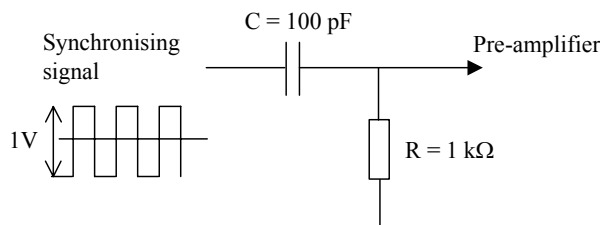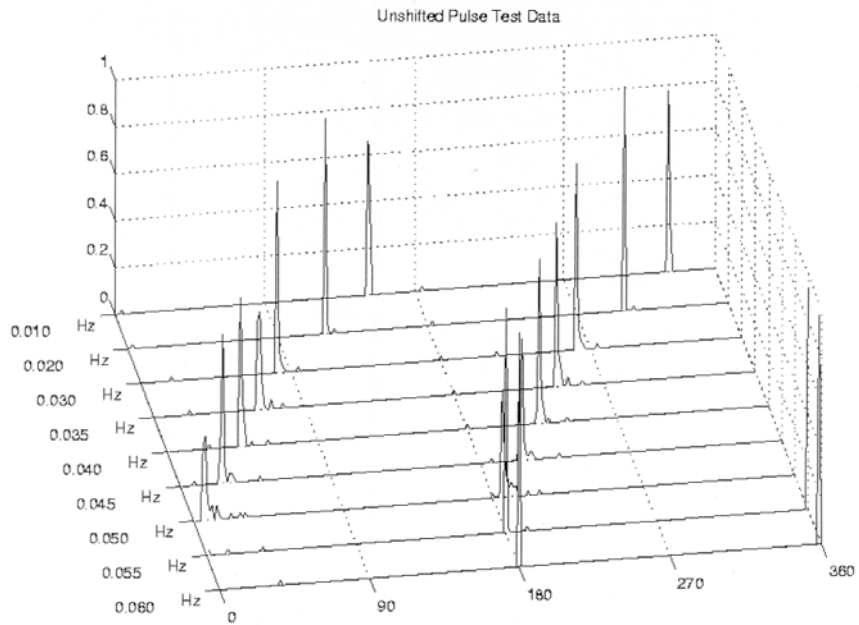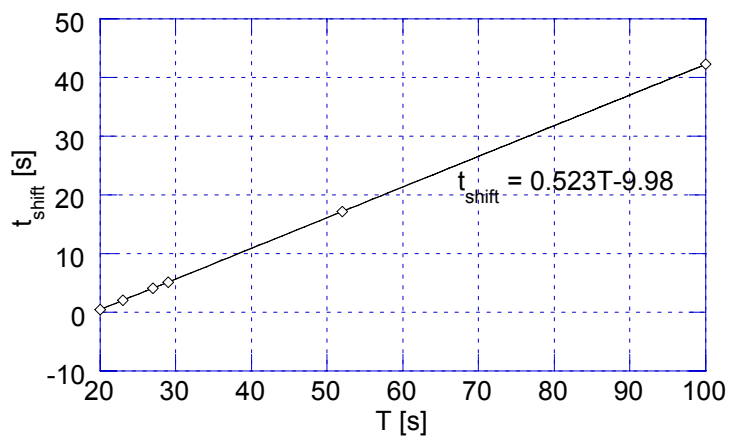

Figure 6.12 Pulse generating circuit used for generating test pulses in the zero-crossings of the synchronising signal.

a)

b)

Figure 6.13 a) Phase position of verification pulses at different frequencies from 0.01 Hz to 0.06 Hz. b) Linear time-shift of pulse occurrence vs. applied voltage period, T.

6.4.5 Software

The control of the ICM over the frequency range 1 mHz - 400 Hz required a completely new software. This software was written in Borland C++ 5.02 [76] and controlled the ICM acquisition unit and the DAP-card used for generating the input voltage to the HV-amplifier and the synchronising signal.

The intended measurement is specified on the *settings.txt* text-file, which is read into the computer and executed. An example of the *settings.txt* file is shown in Figure 6.14.

The first section is *Amplifier Settings*, here is the amplification of the main- and pre-amplifier (RPA 1) specified as well as the 6 dB cut-off frequencies for the band-pass filters in the main amplifier. The next section is devoted for *Gate Settings*; however, the gate of noise facility has not been used in this project but is implemented for future versions and for completeness. The gate unit has similar properties as the main amplifier. The third section contains *A/D Converter Settings* where ADCmd is the Analog to Digital Conversion mode and determines how the reading of the PD-pulse signal should be taken. In this project triggering on the first peak above the discrimination level has been used and re-triggering is not allowed during the dead time (FPNonRetr). The dead time determines the time between two readings and as such it determines the maximum allowable repetition rate of discharges. The dead time must be adjusted to the pulse-width of the pulse to be converted to avoid readings of pulse-echoes. The Analog to Digitial Converter Low Level Discriminator is used to discriminate against noise and pulse-echoes. In order to discriminate against amplifier noise it must not be set lower than around 4 % of maximum reading (5 V). The coding has here been used as Linear and Bipolar but for example unipolar and logarithmic code could be used as well. The beeper has been turned off. The last two lines are used for selecting synchronising with line (50 Hz) or external and on which slope the instrument should trigger. External triggering is essential here with synthesised signals, and positive slope has been used.

The *Data Acquisition* section starts with if the measurement is calibrated or just scaled, and how much charge in [pC] that is represented by a certain amplitude level in discrete units. The number of tests to be run is specified and is listed in the end of the file. The acquired PD-pattern is stored together with settings data and measurement conditions in a binary *filename*.dat file. The filename is composed of a four-letter base-name that indicate the type of object, then a two digit number is devoted for the test set number and finally a second two digit number is appended to specify the exact test number in the sequence. For example *sdkp1307* means surface discharges on kapton, test set number 13 and test number seven in the sequence of (here) different frequencies, i.e. 1 Hz and 5000 V. The file location is specified in the report path. The following lines are devoted for comments, but comes in an order similar to the default structure in the standard ICM program. The last section describes the test sequence to be run, and is composed of the test number, the applied voltage frequency, the applied voltage magnitude in volts peak and the number of voltage cycles to be applied.

```
Amplifier Settings(WAS)

Amp_Main_Gain        =  4              {1,2,4,8,10,20,40,80,100,200,400,800}
Amp_Pre_Gain         =  10            {0=OFF,1,10,100}
Amp_Gate_Enable      =  0        {0=TRUE,1=FALSE}
Amp_OK_LED           =  0        {0=ON,1=OFF}
AmpUpperCutoff[kHz]  =  800            {250,600,800}
AmpLowerCutoff[kHz]  =  40             {40,80,100}

Gate Settings(WGS)

Gate_Main_Gain       =  800      {1,2,4,8,10,20,40,80,100,200,400,800}
Gate_Pre_Gain        =  10             {0=OFF,1,10,100}
Gate_Enable          =  0        {0=TRUE,1=FALSE}
OK_LED               =  0        {0=ON,1=OFF}
UpperCutoff[kHz]     =  800            {250,600,800}
LowerCutoff[kHz]     =  100      {40,80,100}
Gating               =  0        {0=OFF,1=Amplifier,2=A/D,3=Amp&ADC}
Gate_Level(WGL)      =  4.5      {Value_in_%_from_0_to_100%16bit!}

A/D_Converter Settings

ADCmd(SAFSAT,SDNSDR) =  2        {1=TimeWinNonRetr,2=FPNonRetr,3=FPRetr}
Dead_time[us](WD)    =  10.0     {dddd.d_in_range_0.1<=dddd.d<=5000.0}
ADCLowLevDsc[%](WAL) =  4        {Value_in_%_from_0_to_100%_must_be>4%}
Coding(SAC)          =  0        {0=LinBip,1=LinUnip,2=log,3=sine,4=sqsin}
Beeper(SBM,SBG,SBD)  =  0        {0=Melody(off),1=Gatetime,2=Deadtime}
Sync/Trigmd(SL/SE)   =  1        {0=Line(SL),1=External(SE)}
Sync/Trgslp(SP/SN)   =  1        {0=Negative(SN),1=Positive(SP)}

Data Acquisition

Calibration_mode     =  1        {0=scaled,1=calibrated}
Calib_charge[pC]     =  780      {2,5,10,20,50,100,200;x1orx10}
Calib_units          =  7        {Range_1thru128step1}
Num_of_tests         =  10       {integer}
Base_name            =  sdka     {four_letter_description}
Test_set             =  13       {one_or_two_digit_number}
Report_path          =  c:\database\kapton\   {valid_pathname\}

Report Header
                     *(Align here)
Report Number..........0001
Report Name............sdka
Test Object Number......
Test Object Name.......
Inspector..............Uno Gäfvert
Executive..............Hans Edin
Testing_Personnel......Hans Edin
(continued)............
(continued)............
Comments...............Shift Equation:
(continued)............0.5226T-9.975
(continued)............N2,31C  0%RH kapton
(continued)............960mbar

Test Sequence

Number          Frequency       Amplitude       Number_of_periods

1               100                  5000               500
2                50                  5000               500
3                20                  5000               500
4                10                  5000               500
5                 5                  5000               200
6                 2                  5000               200
7                 1                  5000               200
8                 0.5                5000               100
9                 0.2                5000               100
10                0.1                5000               100
```

Figure 6.14 The settings.txt set-file

6.4.6 Calibration of PD system

Calibration of the PD detection system must be performed in order to achieve correct readings of the apparent charge. The method for calibration applied here is the one recommended in IEC standard 60270 [77].

The calibration is performed by applying a step-voltage ΔV_{Cal} in series with a calibration capacitance C_{Cal} across the test object, thus producing a current pulse with a charge content $q_{Cal} = C_{Cal} \Delta V_{Cal}$. The electronic calibrator used here is a Haefely PD Calibrator Type 451, with calibration charge magnitudes in the range 2 pC - 2000 pC.

The relation between the actually detected charge q_{Det} and the calibration charge q_{Cal} is given by the capacitances in the network [52], i.e. C_T, C_K and C_{Cal},

$$q_{Det} = \frac{1}{1 + \dfrac{C_T + C_{Cal}}{C_K}} q_{Cal} \tag{6.1}$$

and q_{Det} is equal to q_{Cal} if $C_K \gg C_T \gg C_{Cal}$.

It is of particular importance to keep the calibration error as small as possible when simultaneous measurements of PRPDA and dielectric spectroscopy are performed, i.e. when PRPDA data are to be quantitatively compared with dielectric spectroscopy measurements of the same PD-current [52].

The condition $C_K \gg C_T \gg C_{Cal}$ is not always possible to fulfil when a low-power source as the TREK HV-amplifier is used (max current 20 mA). The solution is to use the largest possible coupling capacitor that the TREK can supply and perform a careful circuit analysis of the relation between the apparent charge, detected charge and the calibration charge.

6.4.7 Combined gain measurements

In some situations it occurs that the object under investigation suffer by partial discharges of a large dynamic range, i.e. both small discharges (often many) and big discharges. A high gain in such a situation will force the amplifiers to saturate for the highest discharge magnitudes, and thus, these can not be quantified correctly. On the other hand, a small gain will yield a correct interpretation of the large discharges, but will discriminate against the small. These two effects, if not considered, may yield a complete miss-interpretation of, for example, the total charge/cycle or any other measure that are sensitive to the total amount of charge.

The smallest discrimination level allowed for the ICM system is less than 4% of maximum reading. However, counting with the worst situation yields that problems will occur if the ratio between maximum and minimum discharge level is larger than 1/0.04, i.e.

$$\left(\frac{q_{max}}{q_{min}}\right) > 1/0.04 = 25 \qquad (6.2)$$

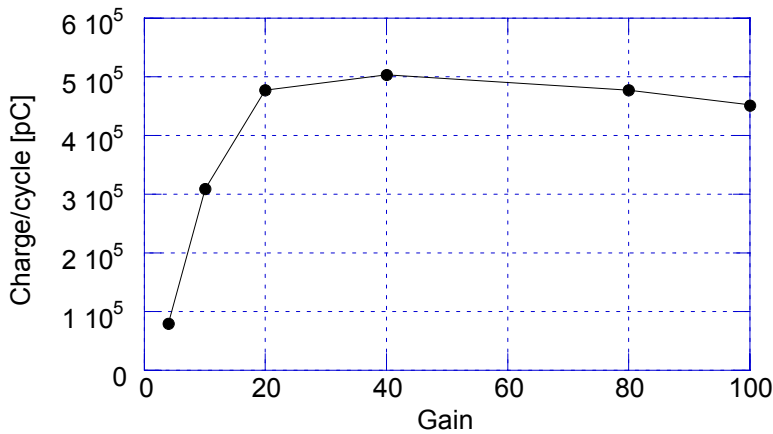An example of this effect is shown in Figure 6.15 for surface discharges along a Kapton surface.

Figure 6.15 Total charge per cycle for surface discharges on Kapton measured at different gains, V = 6 kV$_{peak}$ and f = 50 Hz.

The discriminator level is here set to 4% and measurements at different gains have been performed. At the lowest gain is the highest discharges measured correctly whereas the discrimination against the smaller discharges is hard. However, at increasing gain, more of the small discharges will be detected and contributes largely to the total amount of charge, but with the error that the large discharges are measured incorrectly (to small due to saturation). The total charge has a maximum which is explained by the fact that with further increasing gain the large (saturated) discharges are given smaller values, an effect that is not compensated for by including more small discharges. The optimum in Figure 6.15 seems to be at a gain of approximately 40.

One solution to overcome the above mentioned problem is to measure at two different gains, one low and one high, and then combine the two patterns into one measurement. In principle, the large discharges are taken from the low gain measurement and the small discharges from the high-gain measurement.

The combined pattern is formed by first taking data from channels 2 to 255 in the pattern measured with the high gain, channel 1 and 256 is omitted since they contain the saturated discharge magnitudes. These data must not be counted twice and the corresponding magnitude levels should be removed from the low gain measurement, i.e. the first *128/(G$_H$/G$_L$)* channels of each polarity from this pattern is discarded. Nevertheless, the final pattern

has more channels than a single ordinary pattern; this yields that the analysis software must allow for an arbitrary number of amplitude channels. With this method it is important that the ratio G_H/G_L is not higher than 25, i.e.

$$\left(\frac{G_H}{G_L}\right) < 1/0.04 = 25 .$$

(6.3)

This yields that discharges that are lower than the discriminator level with the low gain (G_L) will be amplified too much with the high gain (G_H) and becomes saturated; thus, they are never counted correctly.

Two obvious disadvantages by this procedure is a doubled measuring time and that the two patterns are measured non-simultaneously which may yield inconsistencies due to the stochastic nature of PD.

6.4.8   Shunting of large discharges

Discharges may have a very large magnitude, i.e. too high to be measured correctly with either the electrometer or the ICM.

When it concerns the ICM the basic problem is that the voltage across the measuring impedance will be too high if a too large current will pass. This will in its turn force the pre-amplifier to saturate even at its lowest gain, and thus, no discharges above this can be detected correctly. Two methods may be applied to solve that problem, where the standard solution is to change the detection impedance. The impedance used here, as discussed above, is an R in parallel with an L and with an unavoidable C in parallel, mainly from the coaxial cable between the measuring impedance and the pre-amplifier. A reduction of the voltage amplitude will be done by enhancing the capacitance, e.g. by increasing the length of the coaxial cable. However, this will alter the characteristics of the response.

The alternative solution is to measure only in the coupling-capacitor arm and by-pass part of the current by a shunting capacitor. However, the introduction of a large shunting capacitor will lower the maximum allowed frequency or voltage due to the finite power in the high voltage amplifier.

6.5   Dielectric Spectroscopy and Simultaneous measurements

6.5.1   System for dielectric spectroscopy

The dielectric spectroscopy system developed for the investigations in this thesis has been developed by the author with assistance from Mrs. Giddens Herbig during her "post-master" period at KTH [60]. A schematic drawing of the dielectric spectroscopy system is shown in Figure 6.16.
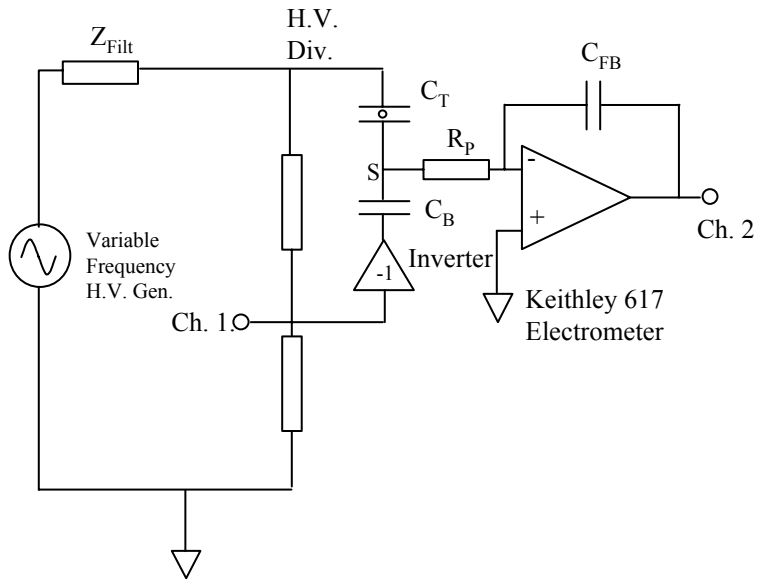
Figure 6.16 Schematic drawing of the system for dielectric spectroscopy.

The high-voltage is applied across the test-object after low-pass filtering in the high-voltage filter. The applied voltage is measured by the high-voltage divider and measured on channel 0 at the DAP-card. The current through the test-sample is mainly capacitive due to the dielectric nature of the test-samples. This capacitive current may be balanced out by adding a capacitive current equal magnitude but reversed sign in order to increasing the resolution of the loss-component and non-linearities in the current, caused by e.g. partial discharges.

Inverter: The inverter with high current buffer used in the system was originally adopted for a previously designed dielectric spectroscopy equipment and is well documented in the licentiate thesis by Thärning [3]. The essentials of the inverter are a very small phase-shift between input and output, a variable gain that can be adjusted to achieve balance, and an output stage that is able to drive an equal large capacitive current as in the test-object.

Balancing capacitor, C_B: The balancing capacitor is selected to fully compensate for the capacitive current in the test object at that particular frequency where the balancing is performed. The balance condition is:

$$C'(\omega_{Bal})V_0 = C_B V_{Inv} \tag{6.4}$$

The inverter output is limited to $V_{Inv,max} = 12\ V$, which impose a minimum requirement of $C_{B,min} = C'(\omega_{Bal}) \cdot V_{0,max} / V_{Inv,max}$, where the maximum test-voltage is $V_{0,max}$. The inverter can amplify the input voltage from 1 to 39 times, i.e. k_{Inv}. The maximum value of C_B is determined by the divider ratio $G \approx 3620$, and the minimum inverter gain, $k_{Inv,min} = 1$,

76

as $C_{B,\max} = G \cdot C'(\omega_{Bal})/k_{Inv,\min}$. This yield the following range for the balancing capacitor:

$$C'(\omega_{Bal}) \cdot \frac{V_{0,\max}}{V_{Inv,\max}} \leq C_B \leq C'(\omega_{Bal}) \cdot \frac{G}{k_{Inv,\min}} \tag{6.5}$$

The above inequality is guaranteed by the fact that the maximum peak voltage ever applied with the equipment is 20 kV$_{Peak}$, which also limit the inverter input voltage to 20000/3620 V $\approx$ 5.52 V.

In the above relations it is required that the balancing capacitor is a loss-free capacitor. Here metallized polypropylene capacitors have been used with a loss-tangent less than $5 \cdot 10^{-4}$ at room temperature. However, leakage currents on the surface housing may appear but can be reduced by proper cleaning of the surface and by the application of a guard electrode. The balancing capacitor is then mounted in a shielded box or tube. In the present equipment, and for the experiments performed in this thesis the effective loss tangent of the balancing capacitor achieved in this way is low enough. However, in low-loss applications such as dielectric spectroscopy on water-tree infested XLPE insulation [3] there are higher demands on a low loss in the balancing capacitor and a high degree of temperature stability. If required, it is possible to reduce the losses further by lowering the fixture with the polypropylene capacitor in a cryogenic container with liquid nitrogen. The low temperature (77 K) reduce the loss-tangent to below $5 \cdot 10^{-4}$ and yield at the same time a constant temperature. The capacitance and loss of the balancing capacitor and connection cables were measured in advance with an HP 4284A LCR meter, and implemented in the program.

Electrometer: A Keithley 617 Electrometer [78] of which pre-amplifier has been used to integrate the current to a voltage (charge divided with C_{FB}). The pre-amplifier is supplied with a feedback capacitor, C_{FB} of the same low-loss type as the balancing capacitor above, and properly guarded. The current to voltage relation is simply obtained as

$$V_{Ch1}(t) = -\frac{1}{C_{FB}} \int_0^t i(t')dt' + V_{Ch1}(0) \tag{6.6}$$

or with a sinusoidal current

$$V_{Ch1} = -\frac{I_{in}}{j\omega C_{FB}} \tag{6.7}$$

The benefit by using capacitive feedback is the suppression of high-frequency noise with a factor $1/\omega$. A disadvantage is that any small direct current component will cause a voltage ramp on the electrometer output that will force the electrometer in overload. The way to overcome that problem is to incorporate a feedback resistor in parallel with C_{FB}; however, this has not been done in this equipment. The gain of the feedback pre-amplifier is

controlled by C_{FB}, and for a linear response C_{FB} is determined by the remaining current amplitude after balancing, i.e.

$$\hat{V}_{Ch1} = \frac{\hat{I}_{in}}{\omega C_{FB}} = \frac{\hat{V}_0 \sqrt{\Delta C_{Lin}'^2(\omega) + C_{Lin}''^2(\omega)}}{C_{FB}} \leq 10\,V \tag{6.8}$$

Thus, the size of C_{FB} is determined by the applied voltage amplitude and the dispersion of the material. However, when the current contains PD-current impulses, then the dynamic range must be extended which increase the magnitude of C_{FB}.

The performance of the electrometer when partial discharges are present is discussed in [52].

The pure capacitive feedback will also imply that unipolar corona discharges will cause a ramp at the electrometer output, and are as such inconvenient for measurements of corona discharges, but is in the same way a sensitive detector for unipolar currents. However, measurements can be performed if C_{FB} is large enough and the measurement time is so short that saturation of the electrometer does not occur.

Data Acquisition and Processing (DAP) card:

As commented on above, the PC is supplied with a DAP-card that is programmed to generate the variable frequency low voltage that is amplified by the TREK 20/20 HV amplifier and a synchronising signal for the ICM. Furthermore, the DAP card can sample up to 16 input signals consecutively when the inputs are configured as single-ended. Two of these input channels are devoted to measure the applied voltage (V_{Ch0}) and the electrometer output (V_{Ch1}). The two input channels are sampled with equal sampling-rates, rates that are dependent on the applied voltage frequency. The samples are stored in a memory buffer on the DAP-card and are after each cycle written onto temporary files on the hard disk. This yields that all measured cycles (~ 400) are stored and not only an average of the acquired data.

6.5.2 System for simultaneous measurements of PRPDA and dielectric spectroscopy

The system for VF-PRPDA was combined with the system for dielectric spectroscopy to allow simultaneous measurements of PRPDA and dielectric spectroscopy and is described in [52].

78

6.5.2.1 Software for the simultaneous system

This program for controlling the dielectric spectroscopy system with the additional code required for running the simultaneous measurements was written in a similar way as the stand-alone program for VF-PRPDA measurements, i.e. in Borland C++ 5.02 [76]. This program controlled the ICM acquisition unit as well as the DAP-card used for generating the low-frequency signal and the synchronising signal, and for measuring the applied voltage (V_{Ch0}) and the integrated current (V_{Ch1}).

Three files are used for controlling the measurement to be performed, i.e. the *genset.txt* file, see Figure 6.17, the *icmset.txt* file and the *k617set.txt* file. The *icmset.txt* file is in principle similar to the *settings.txt* file used above, but the lines after *Calib_units* until *Report_path* and the *Test Sequence* specification are moved to the *genset.txt* file.

```
General Set File

Current_to_voltage    = 0          {0=K617Electrometer,1=K428Current
                                    Amplifier}
Feedback_capacitance  = 32.9e-9    {Value[F],0=Not_used}
Feedback_resistance   = 0          {Value[Ohm],0=Not_used}

Balanced/Straight     = 0          {0=Balanced,1=Straight}
Balancing_capacitor   = 0.47e-6    {Value[F]}
Series_resistance     = 1.5        {Value[Ohm]}

Raw_data/Harmonics    = 0          {0=Raw_data,1=FFT_components}

Balance_flag          = 1          {0=Cprim_meas,1=Real_meas}
Balance_freq          = 60.0       {Value,nnn.n[Hz]}
C0                    = 250e-12    {Geometrical_capacitance[F],0=Unknown}
Cprim_at_balfreq      = 825e-12    {Cap_at_bal_freq[F],0=Unknown}
eprim_at_balfreq      = 3.3        {Epsprim_at_bal_freq[rel],0=Unknown}

HV_filter             = 1          {0=None,1=Filter1}
HV_divider            = 1          {0=None,1=Barrel1}
Coupling_capacitance  = 200e-12    {Value[F],0=None}
Detection_impedance   = 1          {0=None,1=Imp1}

Test Information

Num_of_tests          = 10         {Integer}
Base_name             = sdkp       {Four_letter_description}
Test_set              = 4          {One_or_two_digit_number}
Report_path           = c:\database\kapton\  {Valid_pathname\}

Test Sequence

Number          Frequency       Amplitude       Number_of_periods

1               100             5000                              500
2                50             5000                              500
3                20             5000                              500
4                10             5000                              500
5                 5             5000                              200
6                 2             5000                              200
7                 1             5000                              200
8               0.5             5000                              100
9               0.2             5000                              100
10              0.1             5000                              100
```

Figure 6.17 The genset.txt file.

The general settings of the measurement to be performed are started by specifying the way the current should be converted to a voltage. In this project the Keithley 617 electrometer with capacitive feedback has been used, but the program is prepared also for the Keithley 428 current amplifier, which has been used with other equipment for dielectric

spectroscopy, [65]. Next, the feedback elements are specified, i.e. the feedback capacitance and/or the feedback resistance. The dielectric spectroscopy measurements could be performed either as a balanced measurement or as a straight measurement, i.e. with balancing capacitor disconnected. For balanced measurements the balancing capacitor and the small series resistance in the connection cables are entered. It is further specified if the DAP-card should directly write acquired data to the computer or first process the data with an in-built Discrete Fourier Transform (DFT).

The balance must be measured before any balanced measurement in order to achieve a correct reading of the capacitive current, if such a measurement should be performed is controlled by the balance flag. The *Balance_freq* is the frequency at which the balancing procedure is performed.

The geometrical capacitance, if known, is then entered, followed by the capacitance at the balancing frequency and the corresponding permittivity if the geometrical capacitance is known.

Furthermore, it is specified which HV-filter and which HV-divider is used. The value of the coupling capacitor is entered as well as the detection impedance used for detecting PD.

The forthcoming fields have been described in conjunction with the PD-system, see the text related to Figure 6.14.

The *k617set.txt* file (not shown) contains a few settings that force the instrument to run in external feedback mode and to run with maximum output range (20 V).

7 Analysis softwares

7.1 Introduction

In this chapter the softwares developed for post-processing of acquired data are described. The first program is designed for analysis of PD-patterns and the second program is used for analysing data obtained by dielectric spectroscopy.

The program for PD analysis significantly facilitate the analysis of acquired data and are essential tools in the analysis of the over 1000 PRPDA data files that have been acquired in the progress of this project. Without the programs it would not have been possible to analyse the large amount of data within a reasonable time. A further motivation for the need of an efficient and expandable analysis tool are the incorporation of the many measures that can be used in quantifying PD-processes, together with their dependency upon many variables and parameters like voltage, frequency; pressure, temperature, relative humidity, etc.

Data from dielectric spectroscopy consists of the integrated current and the applied voltage sampled during many cycles, often several hundreds. Each cycle can be analysed to give for example the loss tangent and the capacitance, but also the harmonics can be calculated. All measures that can be applied on a single period can then be studied as a function of applied voltage time or different averaging measures may be applied on all periods, or for a range of periods. Furthermore, the variables and parameters that influence the PD process are equally well important for the dielectric spectroscopy data.

The purpose with this chapter is to describe the qualities of the analysis programs, but the chapter has also the intention to be used as a "users guide" to the programs.

7.2 Software for analysis of PRPDA data

The programs developed are designed as Graphical User Interfaces (GUIs) in the MATLAB® version 5.3 [79] environment and requires MATLAB® for running. The qualities of the analysis software for PRPDA may be summarised as:

- A single file can be loaded and the PD-pattern plotted

- Phase- and amplitude-distributions from a single pattern can be plotted

- Several files can be loaded into a fileset and the distributions derived from the patterns may be compared as different sub-plots on the same plot

- Two files measured with a different gain can be loaded and the two patterns can be merged together in a single non-redundant expanded pattern. The expanded pattern can then be used as any other pattern in the further analysis.

- Six filesets of data, each containing 14 files can be loaded simultaneously and used in a quantifying analysis

- Derived quantities like total charge/cycle, total number of discharges/cycle, $\Delta C'_{PD}$, statistical operators, etc. can be plotted as a function of frequency, voltage, temperature, relative humidity, etc.

The program designed for analysis of PD-patterns is called *PDmain* and is run by the command *PDmain* in the MATLAB® Command Window. This command initialises the GUI of the main program, Figure 7.1. A guide on how to use the program in different situations will follow in sections 7.2.1-7.2.3. The basics of the programming structure are briefly described in section 7.2.4.

7.2.1   Load a single file with *PDmain*

An acquired PRPDA data file (*filename*.dat file) may be found on the hard disk or on any external disk unit by browsing in the list in the upper right corner. At startup of *PDmain* the default directory is set to a location specified on a startup.txt file, here E:\Edin\M-filer\Databas\ is the startup directory as shown in the *Enter start directory* text box. Changing disk units is done by entering the disk unit name in the *Enter start directory* text box and then pressing the *Go to start directory* push button. After browsing to the levels where *filename*.dat files appear, the particular file intended for loading is selected. When selecting a particular file a short information about the measurement conditions appears in the *File information* text box, for example:

File: CORO1409.DAT
Voltage: 6000Vpeak
Frequency: 0.5 Hz

Presently, the selected file together with the applied voltage amplitude and frequency are shown. More information could be added to this list-box, but information like relative humidity, temperature, etc. are not naturally added in the *filename*.dat file and are taken from another file that lists the information about each particular file.

The selected file is loaded by pressing the *Load file* push button. The acquired PD-pattern is shown in the upper left corner. Phase- and amplitude-distributions for the visible PD-pattern are obtained by pressing the suitable radio button to the right of the axes in the lower left corner.
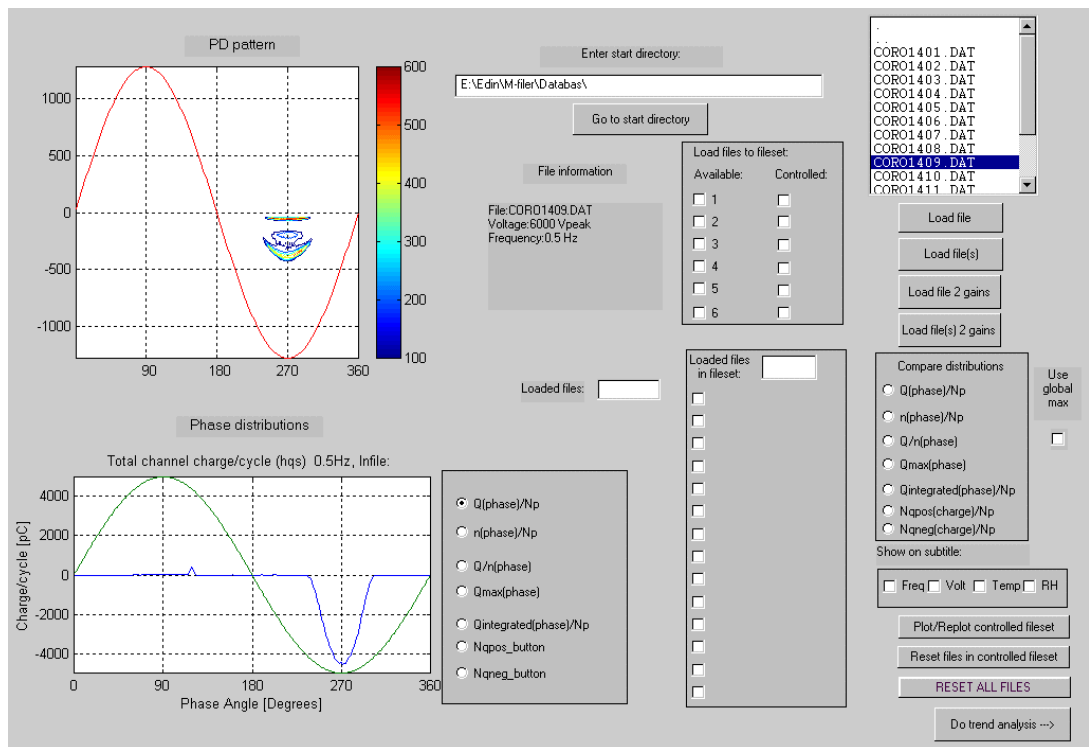
Figure 7.1 Screen-appearance of PDmain when the file CORO1409.DAT is loaded. The data origins from a point-plane gap stressed with a 6 kV, 0.5 Hz sinusoidal voltage.

7.2.2 Load several files into a single fileset for comparison

It is often desired to compare quantities derived from PD-patterns obtained under different conditions, e.g. obtained at different frequencies but with the same voltage and other parameters constant. This can be performed by loading the files into a certain *fileset*, see Figure 7.2.

First, a fileset number must be selected by pressing one of the *Controlled* check-boxes in the *Load files to fileset* menu, advisable the first one if it comes first. This fileset will then automatically become *Available*, but may be disabled by clearing the *Available* check-box if required. Files are loaded into the *Controlled* fileset by consecutively selecting each file and then pressing the *Load file(s)* push button. The loaded files are listed in the *Loaded files in fileset* list. The controlled fileset (2) is indicated in the text box to the right of the *Loaded files in fileset* header. Each loaded file has a check-box ahead of the file-name, which is selected when the file is loaded for the first time. Deselecting this check-box imply that the file will not be used in forthcoming comparisons.
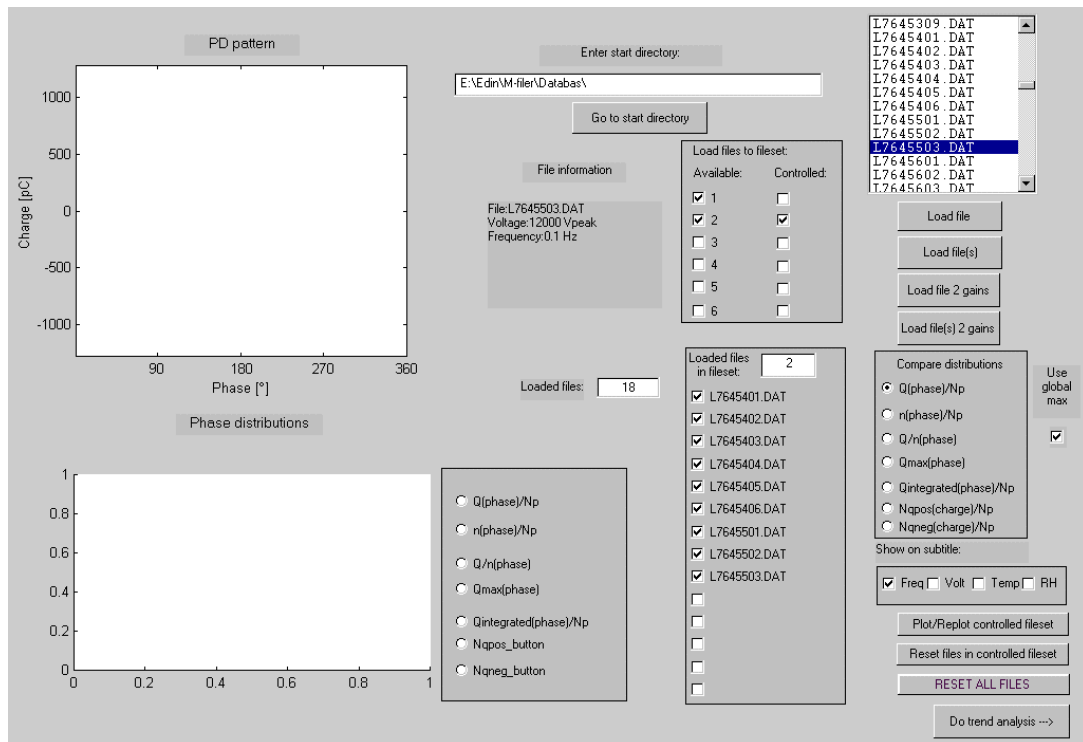
Figure 7.2 Appearance of PDmain when nine files have been loaded into fileset 1 and nine into fileset 2. Q(phase)/Np will be compared for the nine files in fileset 2, the maximum value of all data will be used to scale the ordinate axis in all sub-plots and the sub-titles will be label with the applied voltage frequency.

84

The phase- and amplitude-distributions for the *selected* files in the *Controlled* fileset can now be compared by selecting the proper radio button in the *Compare distributions* menu. For example, Q(phase)/Np, i.e. $H_{qs}(\varphi)$, may be chosen and the distributions plotted by pressing the *Plot/Replot controlled fileset* push button. This plot appears as a new figure with a small subplot for each loaded file in the fileset,

Figure 7.3. The title of each subplot may be set to the applied voltage, frequency, temperature or relative humidity, or as a combination of these four independent variables or parameters, by selecting proper check-boxes in the *Show on subtitle* menu. The voltage and frequency is known for all measurements, but temperature and relative humidity is implemented here because they are of importance for some investigations in this thesis. However, any other parameter like pressure, sample thickness, material permittivity, etc. could be implemented if desired.

The scale on the individual subplot is set according to two strategies: either the maximum value for each subplotted (independent of polarity) distribution is used as maximum scale for that subplot, or the maximum value of all subplotted distributions are used as maximum scale on all subplots. The former scaling is fruitful when comparing for example shapes of the distributions, whereas the latter is perhaps better when comparing the magnitude variation between selected distributions. The latter scaling is selected by the *Use global max* check-box.
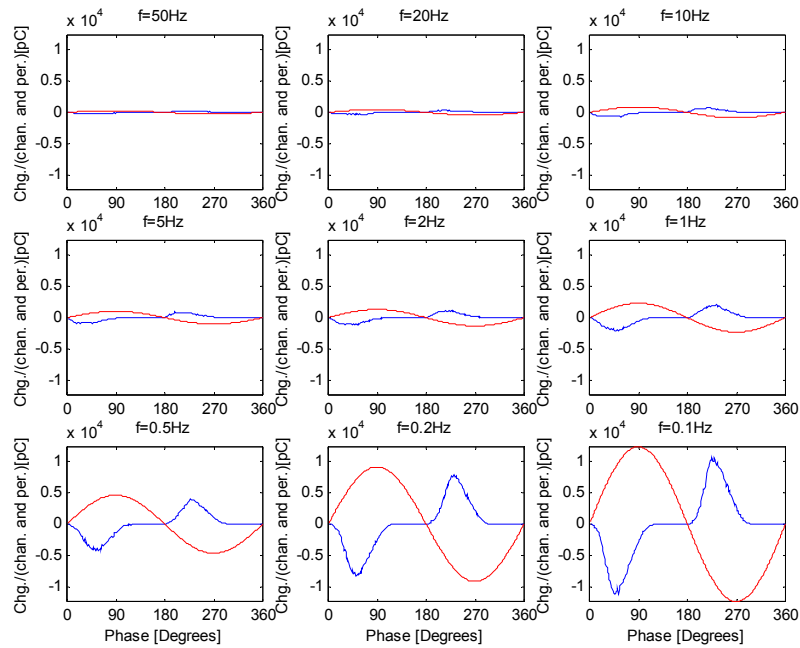
Figure 7.3 Nine phase distributions of Q(phase)/Np, i.e. $H_{qs}(\varphi)$. The applied voltage frequency is given on each subtitle and all subplots have the same scale.

The plots are generated for fast comparisons, but may be edited within MATLAB® to achieve the quality desired for publication. Alternatively, data used for plotting may be stored on a text file and exported to another program.

The maximum number of filesets at the same time are six, with maximum 14 files in each fileset, but the number of filesets and files in each fileset can be extended if required. Comparison of distributions can only be performed within a fileset and not between files in different filesets.

Loaded files in the controlled fileset can be removed by pressing the *Reset files in controlled fileset* push button. All files in all filesets are removed by pressing the *RESET ALL FILES* push button.

The push button *Do trend analysis* in the lower right corner opens up the GUI *Trendanalysis*, which are used for comparisons of different dependent variables derived from the *selected* files in the *Available* filesets.

7.2.3 Trendanalysis

With *Trendanalysis*, Figure 7.4, it is possible to obtain plots of many dependent variables computed on the acquired PD-patterns, versus the independent variables frequency, angular frequency and voltage amplitude; or versus some parameter like temperature and relative humidity.

Up to 16 subplots may occur on each plot. Each *Active subplot* has its own setup of dependent variables (*Chosen properties*) vs. one independent variable (*vs. variable*).
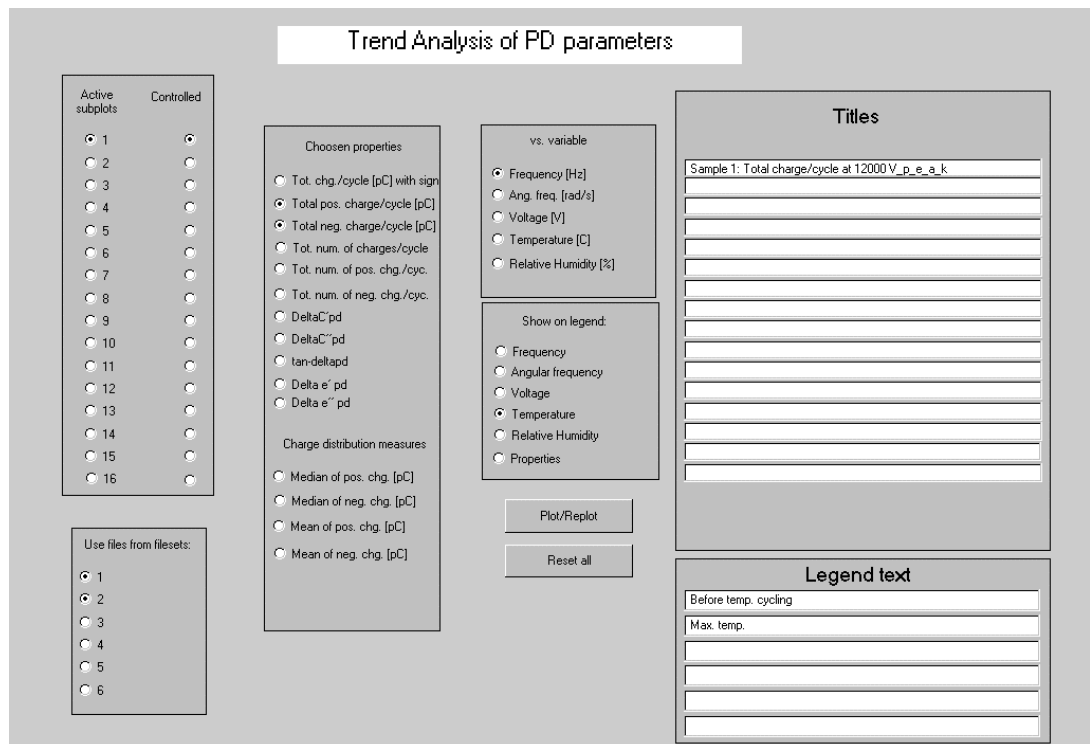
Figure 7.4 Screen-appearance of the Trendanalysis GUI.

In the following it will be explained how the total charge/cycle of both positive and negative polarity for the two filesets loaded with *PDmain*, Figure 7.2; can be plotted versus frequency in the same figure, Figure 7.5.

First, the *Active subplot* (1) radio button intended for use is selected. Next, the subplots setup is made *Controlled* by pressing the corresponding radio button. Next, the fileset(s) to be compared are selected from the *Use files from filesets* menu (1 and 2). Files that are deselected in the *Loaded files in fileset* menu in *PDmain* are not used by *Trendanalysis*.

Next, the dependent variables are chosen from the *Chosen properties* menu, for example *Total pos. charge/cycle [pC]* and *Total neg. charge/cycle [pC]*, by pressing their corresponding radio buttons. In principle all dependent variables could be selected at the same time, and the user must select which variables that are meaningful to plot in the same subplot.

Next, the independent variable or parameter (here frequency) is selected. Presently one may choose between frequency, angular frequency, voltage, temperature and relative humidity, but this list can be extended if desired.

The title of each subplot could be written in the corresponding text boxes to the right.

The plotted curves may be label and the labels shown as a legend. The legend may contain a combination of the parameters selectable from the *Show on legend* menu (here temperature). The parameters selected to be shown on the legend must be equal for all files within a fileset. The plotted properties may also be selected to be shown on the legend. Additional text may be appended in the end of the legend text string. Each extra legend text corresponds to the fileset. The purpose with this is that the files in each fileset have a common property that may not be given by the default labels, e.g. fileset 1 measured 'Before temp. cycling' and fileset 2 measured at 'Max. temp.'.

The final plot, Figure 7.5, is generated by pressing the *Plot/Replot* push button. The *Trendanalyis* GUI may be reset to its initial state by pressing the *Reset all* push button.
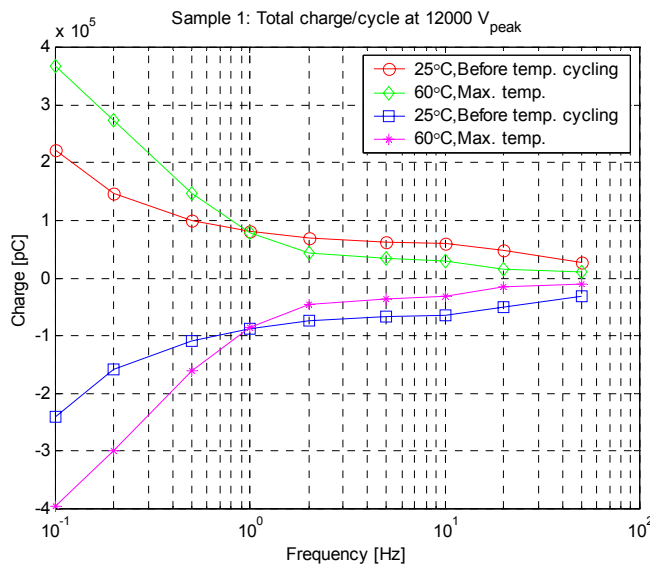
Figure 7.5 Total positive and negative charge per cycle vs. frequency for fileset 1 (25 °C) and fileset 2 (60 °C).

7.2.4 Program structure

The GUIs of *PDmain* and the sub-program *Trendanalysis* are directly developed with MATLABs GUI building tool [80]. Each button of any kind has a callback to only one function. Actually, there are one callback function for *PDmain* and a second function for *Trendanalysis*. Each object in the GUI has a unique identifying *tag*. This tag is used in the callback function to identify the calling object. The action of the calling object is controlled by a switchyard programming structure within the callback functions. The structure of the function *PDcalcinit.m*, which is the callback function for *PDmain*, is shown in Figure 7.6.

Each object in the GUI has a corresponding *case* within the *switch* function, of which only the first three are shown above. Every *case* has its own source code that manages what happens when the related object is calling.

```
function PDcalcinit(tag);

% function PDcalcinit(tag);
% Callback function for PDmain GUI

% Define global variables
global COMPARE_MATRIXhqs1;
global COMPARE_MATRIXhqs2;
.
.
.
switch tag

case 'initialize'
.
.
case 'Listbox1'
.
.
case 'LoadFiles'
.
.
.
end %switch callingObject
```

Figure 7.6 The structure of the callback function used in PDmain.

7.3 Software for analysis of dielectric spectroscopy data

The qualities of the analysis software for dielectric spectroscopy may be summarised as:

- A single data file can be loaded and the acquired applied voltage and integrated current waveforms can be plotted for visual investigation

- The average waveforms after averaging a certain number of waveforms can be plotted

- C', C'', $\Delta C'$, $\Delta C''$ and amplitude of harmonics, e.g. $\sqrt{a_3^2 + b_3^2}$, can be plotted vs. applied voltage period or time

- The harmonic content in either the current or in the integrated current can be plotted. Individual waveform periods or the average waveforms over a range of periods may be used.

The analysis program for dielectric spectroscopy data is the authors but makes partly use of routines developed by J. Sköldin in his Diploma work [81].

The program is run in the MATLAB® Command Window with the command *DSmain* (DS = Dielectric Spectroscopy) and the GUI is loaded and appears as shown in Figure 7.7.
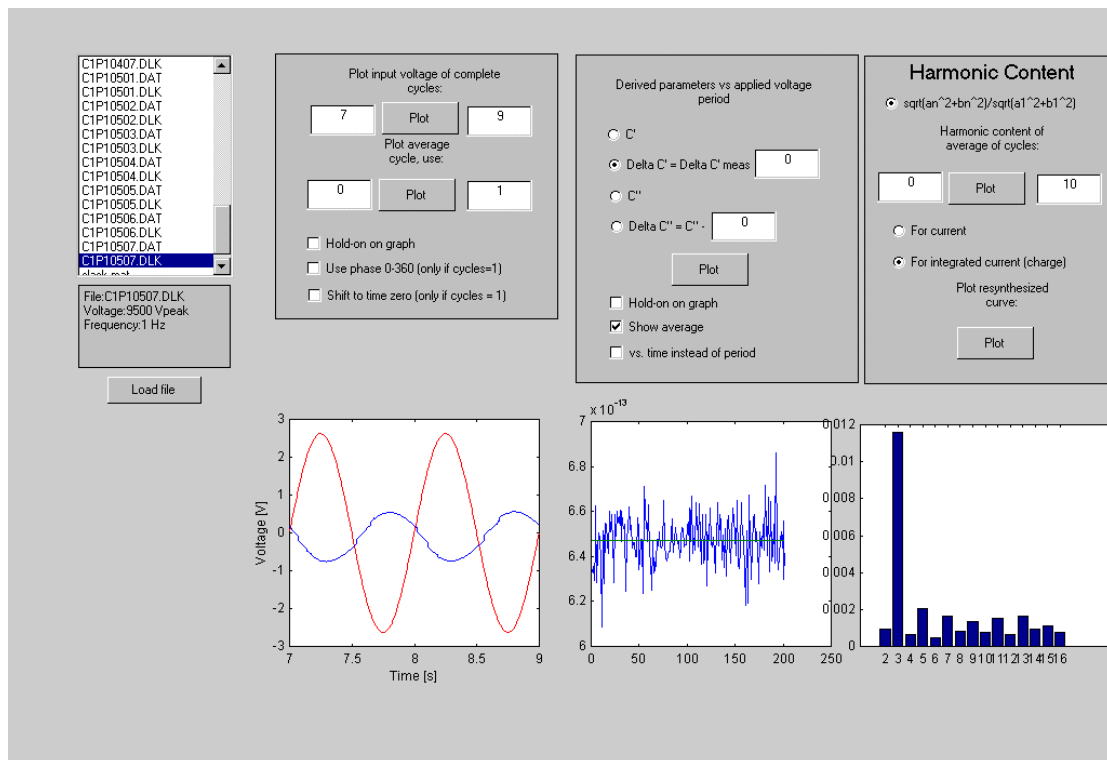

Figure 7.7 Screen-appearance of DSmain when a single file is loaded.

7.3.1   Load a single file with *DSmain*

Data measured with dielectric spectroscopy are stored in binary *filename*.dlk files and may be found on the hard disk by browsing in the list of files in the upper left corner. Each *filename*.dlk file contains data acquired from the application of a single voltage and frequency.

When a particular *filename*.dlk file is selected, the filename, the applied voltage and frequency are directly visible in the text box below the file list. The actual file is loaded by pressing the *Load file* push button.

Different periods of the acquired raw data, i.e. the voltage on the high voltage divider output and the pre-amplifier output from the electrometer, may be selected in the *Plot input voltage of complete cycles* menu and plotted in the corresponding axes. Alternatively, the

90

average waveforms of a range of cycles could be plotted. The plot may be hold for comparison reasons and if only one period is plotted the abscissa could alternatively be scaled to phase instead of time. This property is useful when comparing currents with different frequency.

In Figure 7.7 the file C1P10507.dlk (C1 = Cigré method 1, P1 = piece 1) is loaded, of which data has been obtained with 9500 V and 1 Hz. The raw data for acquired cycles 7 to 9 are plotted vs. time after the start of acquisition. The jumps in the current curve (lowest amplitude) are the charge increase/decrease due to the integration of the PD impulses.

In the menu *Derived parameters vs. applied voltage period* it is possible to select the common dielectric spectroscopy parameters: C', C'', $\Delta C'$, $\Delta C''$ for plotting vs. applied voltage period or time. With $\Delta C'$ or $\Delta C''$ it is possible to subtract a certain value from the measured values. This facility may be used to subtract the linear background capacitance or loss, from the measured apparent capacitances if only the non-linear contribution from PD will be investigated. The result is shown in the corresponding plot. The data fluctuates due to the variations in the PD activity, and the solid line shows the average value, shown because *Show average* is selected.

The third menu is the *Harmonic Content* menu, where the average harmonic content for a range of periods may be selected for plotting. The first radio button is used for selecting the kind of harmonic content measure, presently there are no choice since only the convention with $HC_n = \sqrt{a_n^2 + b_n^2} / \sqrt{a_1^2 + b_1^2}$ is possible. However, it is possible to select between the harmonic content for the current or the integrated current (cumulative charge). The harmonic content of the first 16 harmonics is shown as a bar diagram. Here the odd harmonics dominate, which is a result of the polarity-symmetry of the PD currents.

The same plot window may also be used for plotting the acquired voltage that is proportional to the integrated current, or to plot the (out-balanced) current, i.e. the derivative of the integrated current. For both the harmonic content plot and the current plot, the average of the selected cycles is used.

8 Cable model

8.1 Introduction

The aim with the following section is to demonstrate the VF-PRPDA technique on samples with many defects of a known origin. Two test objects with internal cavities are created as cable-like structures (cable models), with band-gaps deliberately introduced between PET tapes (polyethylene-terephthalate, Mylar™) wrapped around tube of polyolefin that is shrunk onto a copper tube. The frequency range for the measurements on the first cable model was 0.1 Hz - 100 Hz, but was extended to 1 mHz - 100 Hz for the second cable model.

Some of the results have previously been presented at the Nord-IS 1999 conference [59].

8.2 Test objects

Two similar cable models were developed, CBM 1 and CBM 2, with a design shown in Figure 8.1.
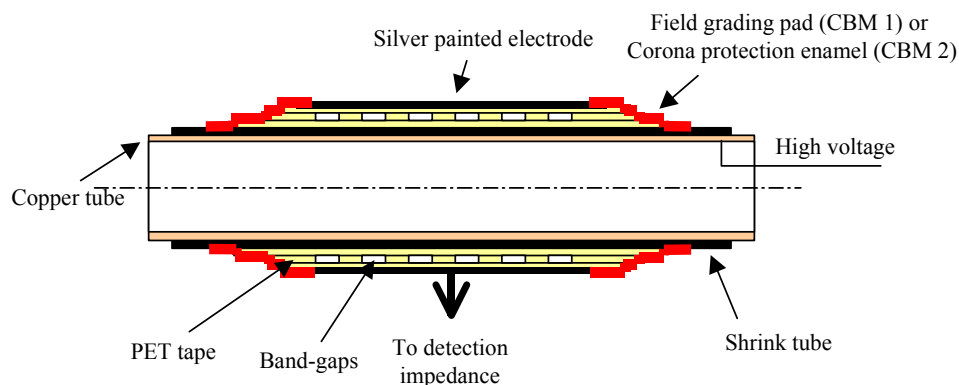
Figure 8.1 Schematic drawing of the cable model.

The inner conductor is a 54 mm in diameter polished copper tube. A shrinkage tube of irradiated polyolefin (FIT-221 manufactured by Alpha Wire [82]) was painted on the inside with a conductive copper-paint and then heat-shrunk on to the copper tube. This procedure was performed in order to minimise the risk of creating metal to dielectric bounded cavities. The final thickness of the shrink-tube was 1 mm. Then, the copper tube was mounted in a turning machine and five layers of a PET (polyethylene-terephthalate, Mylar™) tape was wrapped around the shrink-tube. Band-gaps were deliberately introduced between the layers of PET tape in order to create cavities that could cause partial discharges. The large diameter of the copper tube in comparison to the thin

92

insulation yield a nearly homogeneous field within the bulk material, which ensures a small scatter in inception voltage for the cavities introduced. However, deviations in shape between different band-gaps is likely and may introduce scatter in discharge magnitudes, where the ideal situation is flat band-gaps, but the real situation is a perturbed gap, Figure 8.2.
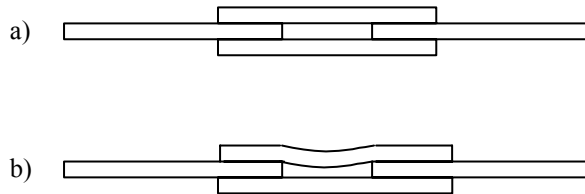

Figure 8.2 a) The ideal situation of the band-gaps and b) the likely situation.

The two samples were made with two different end corona protection strategies. CBM 1 with an ABB-Kabeldon field-grading pad overlapping the PET tape and the low-voltage electrode. For CBM 2 a corona protection, field-grading enamel was painted across the low-voltage electrode and on to the PET surface. The properties of the cable models are summarised in Table 8.1.

Table 8.1 Properties of CBM 1 and CBM 2

Property	CBM 1	CBM 2
Inner conductor, high potential electrode	Cu, $\varnothing$ = 54 mm	Cu, $\varnothing$ = 54 mm
Length of low voltage electrode	25 cm	25 cm
Innermost layer	Irradiated polyolefin, Thickness = 1mm	Irradiated polyolefin, Thickness = 1mm
Outer layers	5 layers of 64 μm thick PET tape	5 layers of 64 μm thick PET tape
Termination	ABB Kabeldon stress-grading pad + IV-tape	Corona protection, field-grading enamel (for machine insulation)
Outer conductor, low potential electrode	Silver paint	Silver paint

8.3 Experimental results

8.3.1 Cable model 1 (CBM 1)

The total charge per cycle versus frequency is shown in Figure 8.3, and the total number of discharges per cycle versus frequency is shown in Figure 8.4. The response is in general fairly flat and frequency independent, except for a small increase in PD activity from 100 Hz down to a peak around 20 Hz, which may be explained by the statistical time-lag. With increasing voltage, the total charge per cycle increases, due to an increase in number of discharges, Figure 8.4 and not due to increased individual discharge magnitudes, Figure 8.5.

There exists an asymmetry between discharges of a positive and negative polarity, Figure 8.3. This type of asymmetry is not allowed in steady status for discharges between insulating surfaces, but could exist for surface discharges that may allow for a conductive path to one of the electrodes.
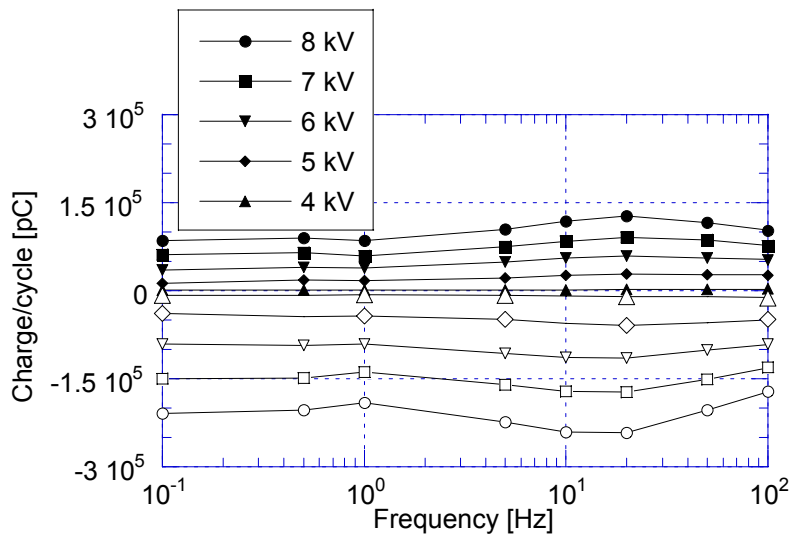
Figure 8.3 Total charge per cycle of positive (filled) and negative (open) discharges vs. frequency for CBM 1. Voltages in the range 4 kV - 8 kV.
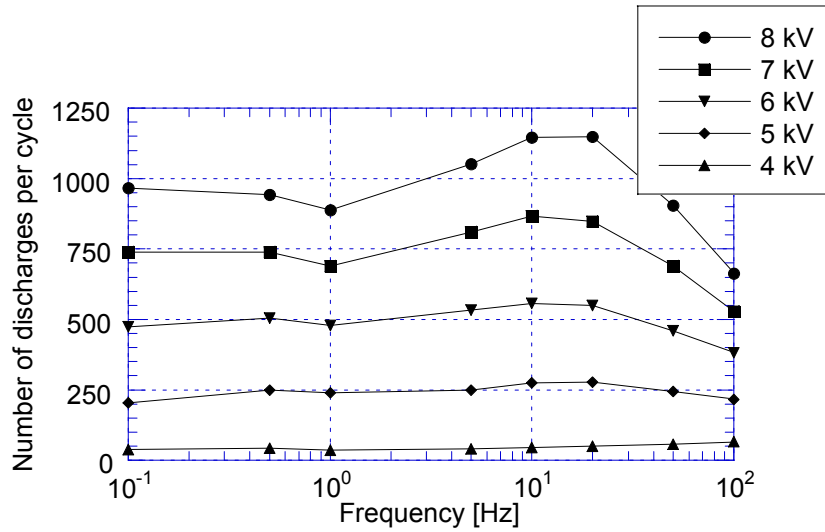
Figure 8.4 Total number of discharges per cycle, N_{Tot} vs. frequency for CBM 1. Voltages in the range 4 kV - 8 kV.

A consequence of decreasing frequency is a reduction of the mean discharge magnitude, Figure 8.5. The major reduction is in the frequency range 10 - 100 Hz and is explained by the fact that with a decreasing frequency the over-voltage is reduced due to less phase-lag, since the statistical time lag should be constant, independent of frequency.
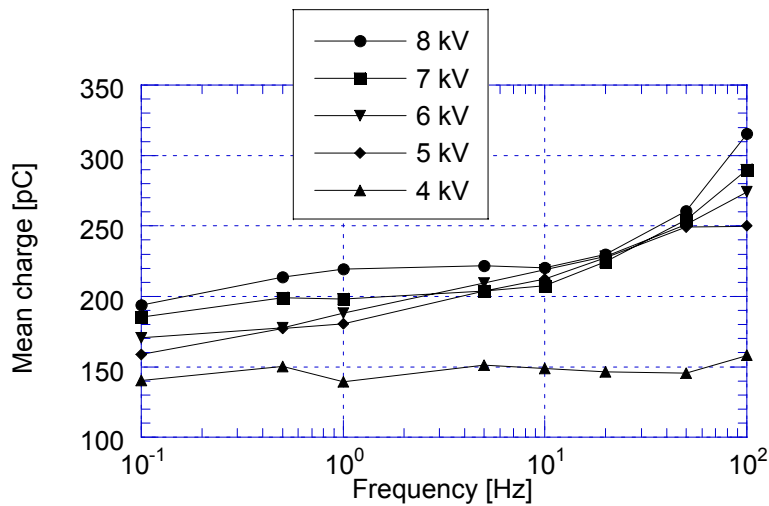
Figure 8.5 Mean discharge magnitude of positive discharges, $\overline{Q}^+$ vs. frequency for CBM 1. Voltages in the range 4 kV - 8 kV.

An increased voltage magnitude does not change the mean discharge magnitude much and the trend in the frequency dependence is the same for voltages above 5 kV. This indicates that it is the same discharge mechanism at all applied voltages. The charge per cycle vs. phase distribution, $\bar{q}(\varphi)$ obtained at 8 kV and for frequencies in the range 0.1 Hz - 100 Hz is shown in Figure 8.6. The domination of the negative discharges is pronounced, but otherwise the distributions indicate void discharges as intended. 50 Hz and 100 Hz differs in magnitude from the lower frequencies, but all distributions are similar in shape and phase location. The voltage zero-crossing overlap of the discharges is caused by the surface charge field from trapped charge species after preceding discharges.
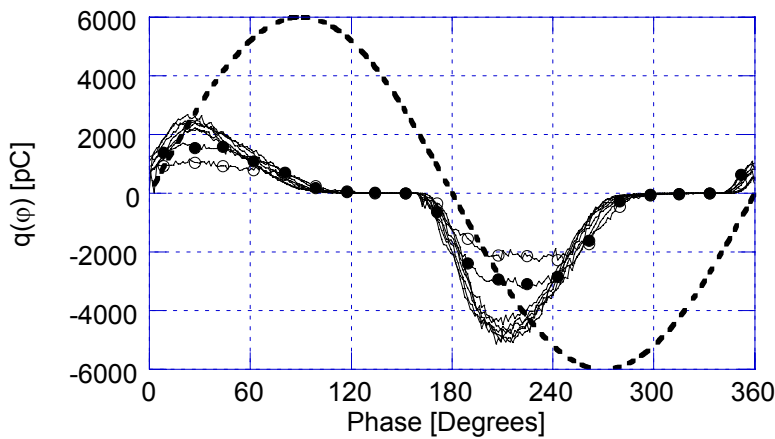
Figure 8.6 $\bar{q}(\varphi)$ for CBM 1 at 8 kV. Symbols: ∘ 100 Hz, • 50 Hz. The other distributions are taken at 20, 10, 5, 1, 0.5 and 0.1 Hz and are almost similar.

The voltage dependence at 50 Hz was measured at two different times during the same day, Figure 8.7, here presented as Run 1 and Run 2. Run 1 was performed by measuring consecutive times at 50 Hz and increasing voltage from 2 kV up to 7 kV, the time between each test was the time needed for storing the PD-data, i.e. around 15 seconds. Run 2 data is taken from a batch of measurements between 4 kV and 8 kV, but with the frequency sweeping from 100 Hz down to 0.1 Hz at each voltage. With 400 cycles at each frequency, this yields around 1.5 hours between 50 Hz data at different voltages. However, the reproducibility between the two runs is very good.

The voltage dependence is close to linear above 4.5 kV and the curvature close to inception is probably due to scatter in the inception voltage for the individual voids. A linear variation in charge per cycle vs. voltage indicate void discharges or delaminations [83]. An inception voltage around 4 kV is not unlikely because an approximative calculation by Paschen's law for air with *p = 1 bar, d_{gap} = 64 μm (V_b ≈ 500V [1, p. 338]), ε'_{PET} ≈ 3.3, $d_{PET,solid}$ = 256 μm; $\varepsilon'_{Polyolefin}$ ≈ 2, $d_{Polyolefin}$ = 1 mm* and a three capacitances in series model, yield an inception voltage of around 5 kV.
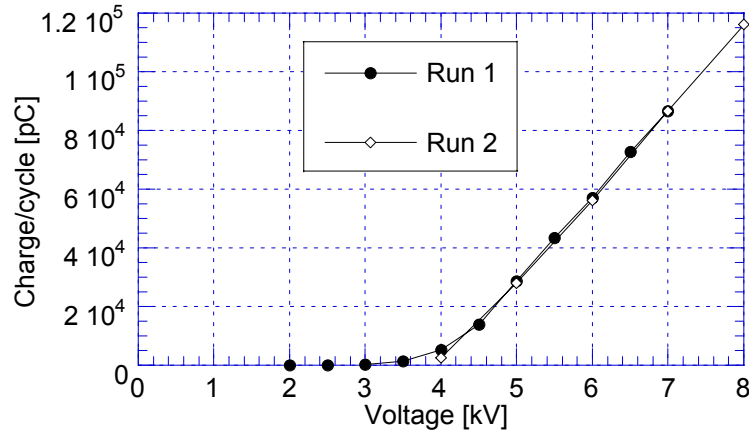
Figure 8.7 Total positive charge per cycle, Q_{Tot}^{+} vs. applied voltage for CBM 1 at 50 Hz.

8.3.2 Cable model 2 (CBM 2)

CBM 2 differs to CBM 1 in the type of termination, but also in the large number of deliberately introduced band-gaps. The VF-PRPDA is applied for frequencies lower than for CBM 1 and covers the range from 1 mHz to 100 Hz.

The total charge per cycle for CBM 2 is shown in Figure 8.8. The increase of the PD activity when the frequency decrease from 100 Hz to around 10 Hz is similar to CBM 1 and is explained by the statistical time-lag. However, the symmetry between the discharging polarities is more pronounced for CBM 2 than for CBM 1. The total charge per cycle is less than for CBM 1, which is caused by a much less number of discharges per cycle, Figure 8.9, but is partly compensated for by larger mean discharge magnitudes, Figure 8.10.

The total charge per cycle is almost monotonous decaying below 5 Hz. The origin of this decay can not be explained by any frequency dependence in the bulk materials of the PET or the shrink-tube, since the loss is small and the permittivities frequency independent in this range. The source is then likely the surface conductivity of the PET surface, which impose a screening-effect that becomes relevant at lower frequencies.
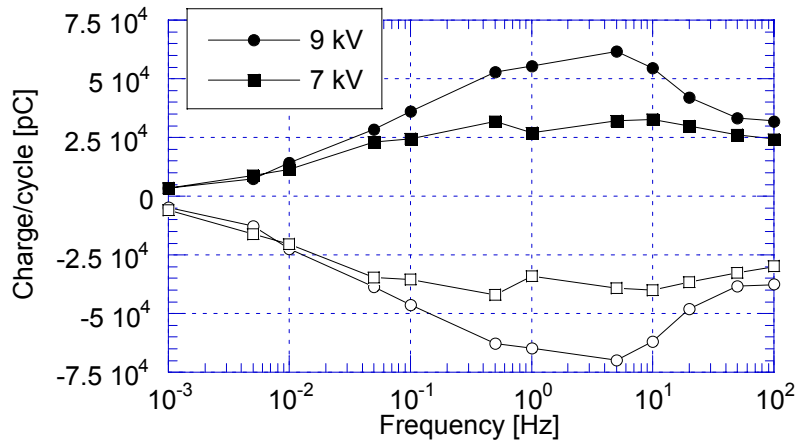
Figure 8.8 Total charge per cycle of positive (filled) and negative (open) discharges vs. frequency for CBM 2 at 7 kV and 9 kV.
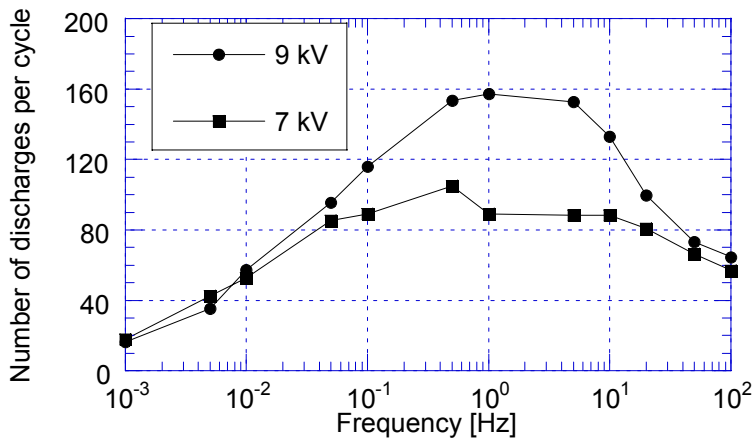

Figure 8.9 Total number of discharges per cycle, N_{Tot} vs. frequency for CBM 2 at 7 kV and 9 kV.

The mean discharge magnitude, Figure 8.10, decrease monotonously from 1000 pC to 500 pC when the frequency decrease from 100 Hz down to 1 mHz, and symmetrical on both polarities. The difference in the mean magnitude between 7 kV and 9 kV is small, which again indicate that the voltage increase yields an increased number of discharges, Figure 8.9, rather than an increase of single discharge magnitudes. This behaviour is consistent

with a reduced statistical over-voltage in the cavity when the applied voltage magnitude increases, which also explains the decrease in decreasing mean charge magnitude when the frequency decrease.
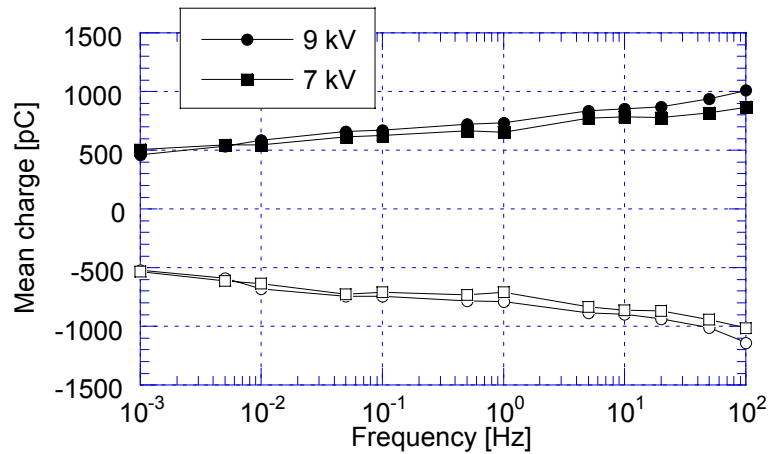
Figure 8.10 Mean discharge magnitude of positive (filled) and negative (unfilled) discharges vs. frequency for CBM 2 at 7 kV and 9 kV.

The voltage dependence of charge per cycle at 10 Hz and 0.1 Hz is shown in Figure 8.11. The inception voltage is somewhere in the range 4 kV to 5 kV. With increasing voltage the PD activity increase, not linearly as expected for cavities with a small scatter in magnitude and not super-linearly as if there are more sites that discharge at increasing voltage, but sub-linearly like a saturation. The reason for this saturation is likely that the magnitude of the single discharge events becomes smaller in magnitude with increasing magnitude, for example due to a reduced over-voltage, these small discharges may fall below the discrimination level of the system and will not be detected.
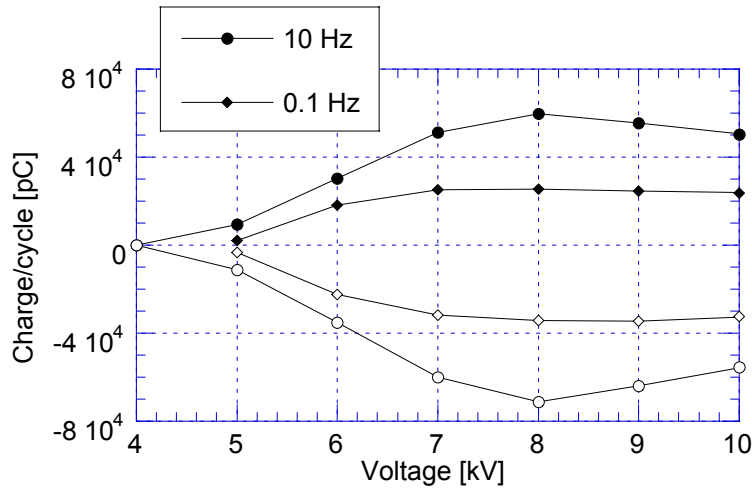
Figure 8.11 Total charge per cycle of positive (filled) and negative (unfilled) discharges vs. applied voltage for CBM 2 at 10 Hz and 0.1 Hz.

The charge per cycle vs. phase distribution, $\overline{q}(\varphi)$ is shown in Figure 8.12. The phase distributions are much shaper and skewed than for CBM 1, cf. Figure 8.6. The reason behind this effect could be that surface discharges are involved for CBM 1. The different phase distributions are symmetric with respect to discharge polarity (different from CBM 1's that are asymmetric) and have a voltage zero-crossing overlap.

The mean phase for 7 kV and 9 kV vs. frequency is shown in Figure 8.13. The mean phases for 9 kV are shifted more towards the zero-crossings of the applied voltage than 7 kV, which is a direct consequence of the higher voltage that yields discharges earlier in the phase. The mean phase variation with frequency is quite small and not distinct. At 7 kV it seems to be a shift towards zero-crossings with decreasing frequency; however, at 9 kV the trend is rather the opposite.
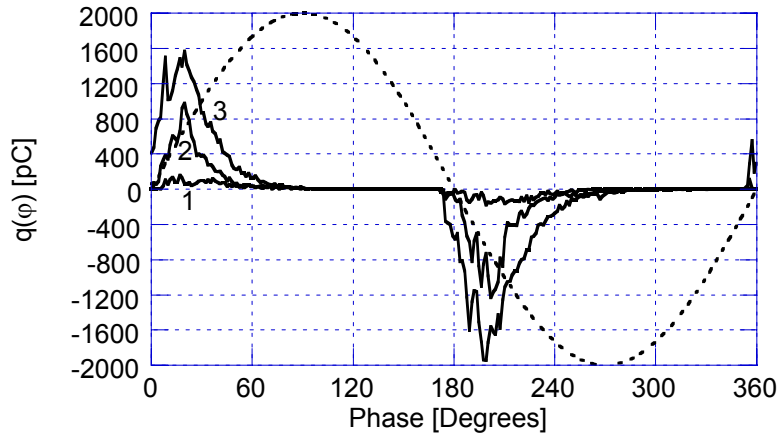
Figure 8.12 $\bar{q}(\varphi)$ for CBM 2 at 9 kV. 1) 1 mHz, 2) 10 mHz and 3) 100 mHz. Distributions at other measured frequencies have a shape similar to distributions 2) and 3).
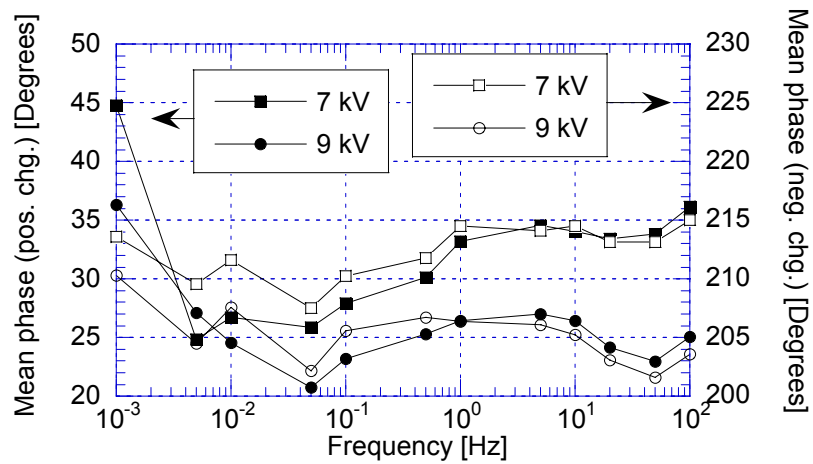

Figure 8.13 Mean discharge phase of positive (filled) and negative (unfilled) discharges vs. frequency for CBM 2 at 7 kV and 9 kV.

The standard deviation, Figure 8.14 shows that 9 kV distributions are broader than 7 kV distributions, except in the frequency range 1 mHz - 10 mHz where the difference is less pronounced. The width of the distributions becomes smaller with decreasing frequency, which is in agreement with a reduced cavity field due to the increasing influence of a surface conductivity.
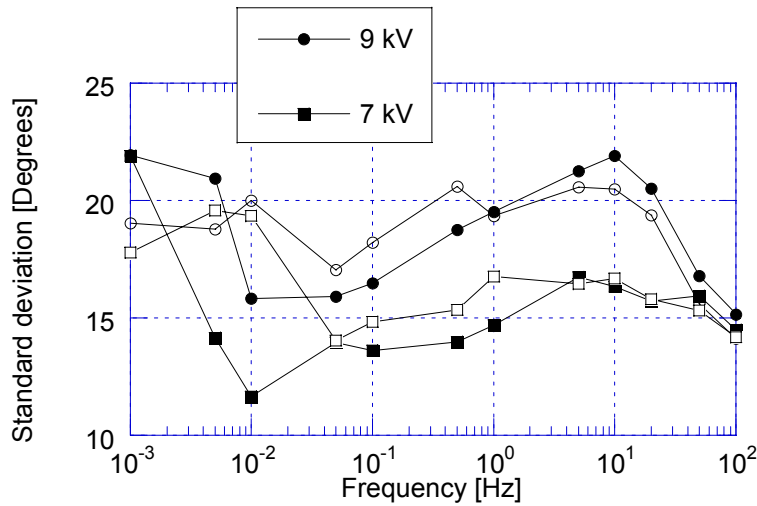

Figure 8.14 Phase standard deviation of positive (filled) and negative (unfilled) discharges vs. frequency for CBM 2 at 7 kV and 9 kV.

The skewness, Figure 8.15, is overall positive. Positive and negative discharge polarity follows each other well. 7 kV is slightly more skewed than 9 kV, but it is not pronounced. Okamoto and Tanaka [61] found for cylindrical voids in epoxy with different depth to diameter ratio that a positive skewness larger than 0.5 indicate flat voids, whereas a negative skewness indicate narrow channels or electrical trees, see also Gulski [57]. The skewness shown in Figure 8.15 is everywhere above 0.5 (accept for one single point), thus, indicating flat band-gaps.
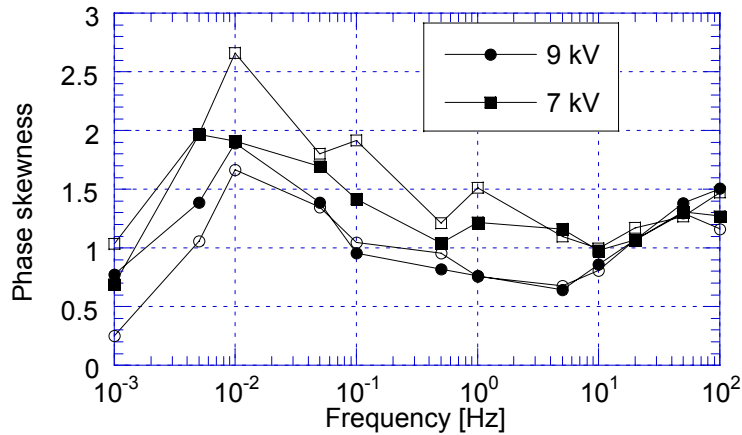
Figure 8.15 Phase skewness of positive (filled) and negative (unfilled) discharges vs. frequency for CBM 2 at 7 kV and 9 kV.

8.4 Surface discharges in CBM 1 ?

There are several observations in the preceded sections that indicate that CBM 1 may suffer by surface discharges and internal discharges, but only internal discharges for CBM 2.

The main argument for that CBM 1 has surface discharges in the terminations is the asymmetry in total amount of charge between positive and negative discharges. Such an asymmetry has been shown for surface discharges [40]. The smooth charge per cycle phase distribution in Figure 8.6 is caused by many discharges of a small magnitude, whereas the sharper distribution for CBM 2, Figure 8.12, is caused by fewer discharges of a larger magnitude. This difference indicates that the discharges in CBM 1, at least partly, may have a different origin than the discharges in CBM 2.

When it concerns the frequency dependence it is clear that the total charge per cycle for CBM 2 decrease with decreasing frequency for frequencies lower than 1 Hz (for 9 kV at least), Figure 8.8. Compared to the total charge per cycle for CBM 1, Figure 8.3, which shows no tendency to decrease with decreasing frequency even at 0.1 Hz. The shape of the total charge per cycle vs. frequency curves observed in Figure 8.3, is also observed for surface discharges on mica [40].

8.5 Conclusions

It has been shown that CBM 1 partly suffer by a discharge mechanism different than CBM 2, likely surface discharges in the terminations.

The discharges in CBM 2 is more pronounced origin from internal cavities, i.e. the deliberately introduced band-gaps. The partial discharge activity for CBM 2 decrease with decreasing frequency, which is probably related to the reducing influence an existing surface conductivity has on the electrical field in the cavity at lower frequencies.

9 Machine insulation

9.1 Introduction

In this chapter, the results obtained with the VF-PRPDA technique on an old asphalt-mica insulated stator-bar is presented. The results have partly been presented in [59]. The frequency dependence have been studied over the frequency range 1 m Hz - 400 Hz with standard measures like total charge per cycle and number of discharges per cycle. Additionally, statistical operators of phase-distributions like, mean phase, standard deviation, skewness and kurtosis have been used in order to investigate if they are frequency dependent and if they could be used to illuminate some important properties of the frequency dependent PD-activity.

The electrical insulation of the stator in high voltage rotating machines are generally aged by PD of different origins and a tremendous amount of work have been spent on different methods for detecting and measuring the PD, see for example Stone [84].

The groundwall insulation of high voltage stator-bars has commonly been made with mica tapes wrapped around the copper bar and impregnated with a binder. The type of tapes and binder has varied, and successive improvements have been performed during the 20th century. An overview of the different insulation systems that have been used throughout the years may be found in McDermid [85]. The improvements have increased the dielectric stress from around 1 kV/mm up to at least 2.5 kV/mm, and an increased operational temperature from 105 °C (Class A) to at least 155 °C (Class F), together with a decreased void content that reduce deterioration by PD [85] and the risk of failure.

The stator bar investigated in this chapter is of the asphalt-bonded mica type. This type of insulation was commonly used from the 1920s and up to the 1950s when the asphalt was replaced with synthetic resins.

PD in older types of large electrical machines seems to be unavoidable. The origin the most common PD sources are discussed by Stone [86]:

- Slot discharges between the groundwall insulation and the slot. The discharges appear when the winding becomes loose and the semi-conductive layer has been eroded due to the bar-motion.

- Internal discharges within the groundwall insulation, either of void types created during manufacturing or due to delaminations caused by thermal ageing.

- Endwinding discharges, i.e. surface discharges on the winding where it leaves the stator core. Caused by the high electric field and a poor stress grading coating.

The literature on PD in machine insulation studied with variable frequency PD measuring techniques is scarce. However, Miller and Black [18, 19] studied total PD energy/cycle,

Δtan δ and amplitude distributions for different types of machine insulation in the frequency range 0.1 Hz - 50 Hz. Miller [87], supplemented their results with tan δ and capacitance tip-up measurements in the frequency range 0.01 Hz - 400 Hz.

9.2   Test object

The stator bar is an old stator bar with asphalt based insulation with mica flakes. The insulation thickness is 4 mm which yields an operating voltage of around 6 - 7 kV$_{rms}$ (phase voltage). A photo of the stator bar cross-section is shown in Figure 9.1. The stator bar contains delaminations, which can be heard by knocking on the bar and listening to parts with a "non-compact" sound.

The tests have been performed in normal atmosphere and under room temperature. The high voltage has been applied on the copper strands joined together and the current measuring electrode is the semi-conductive paint together with a copper wire tightly wrapped around the bar. The bar has on one side its original stress grading termination, but is at the other end terminated with an ABB-Kabeldon stress grading pad fixed with an IV-tape.


*Figure 9.1 Cross-section of the stator bar.*

9.3 Experimental results

The measurement results for the stator bar are presented in the following order: first comes voltage dependence in the range 4 kV - 9 kV over the frequency range 0.1 Hz - 100 Hz, then follows additional results for 9 kV that covers the low frequency range 1 mHz - 100 Hz. Finally, the results from nine consecutive runs at 9 kV and the frequency range 0.1 Hz - 100 Hz are presented.

9.3.1 Voltage and frequency dependence in the range 0.1 Hz - 100 Hz

In Figure 9.2 a) the total charge per cycle is shown at 4 kV and 5 kV. 4 kV is close to the inception voltage at 100 Hz, but is below the inception voltage when the frequency is lower than 5 Hz. At 5 kV, which is roughly 20 % above inception voltage, the total charge per cycle increase with decreasing frequency until 20 Hz, with a consecutive decrease which ultimately leads to the cessation of PD at 0.1 Hz. The result with a further increased voltage is shown in Figure 9.2 b). The effect of an increased voltage is merely an increase in the number of discharges, Figure 9.3; i.e. the discharge origin is not changing. The frequency dependence is basically the same as with 5 kV but with the difference that the PD activity remains at 0.1 Hz.

a)
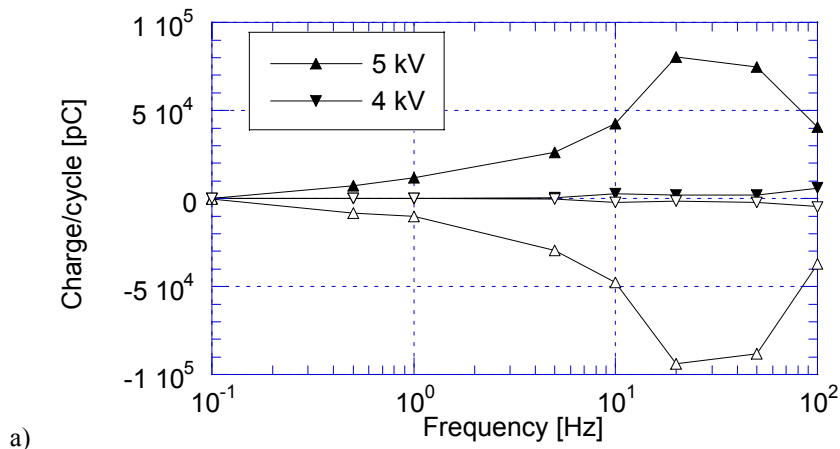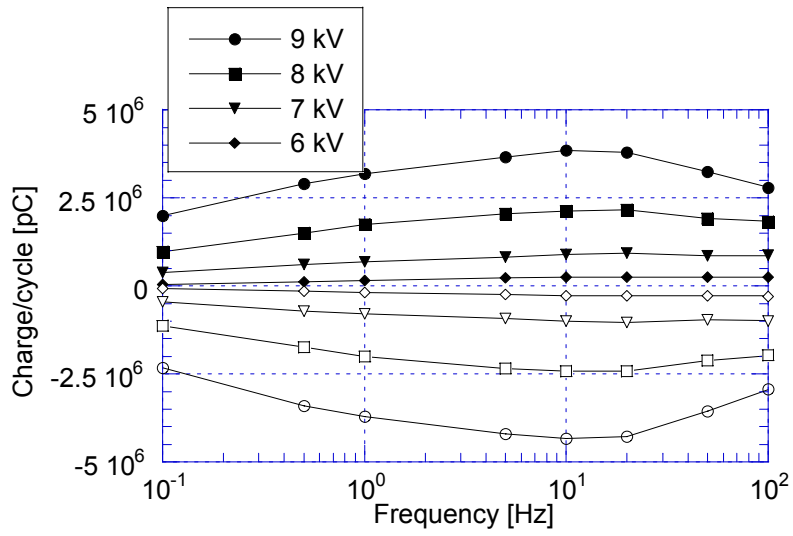
b)

Figure 9.2 Total charge per cycle of positive (filled) and negative (open) discharges vs. frequency for voltages in the range a) 4 and 5 kV and b) 6 kV - 9 kV.
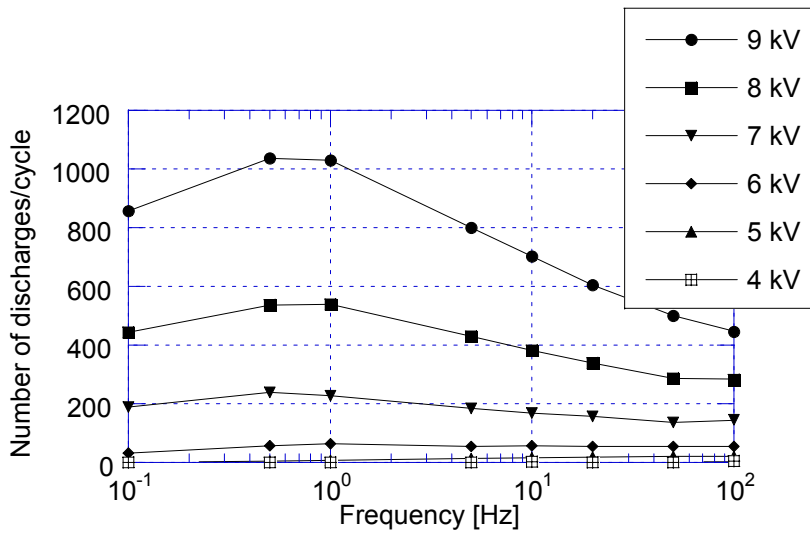

Figure 9.3 Total number of discharges per cycle vs. frequency for voltages in the range 4 kV - 9 kV.

The origin of the PD is due to delaminations and internal voids. This is already indicated in Figure 9.2, where the symmetry between positive and negative discharges is manifested. A more clear picture of the symmetry between discharges of positive and negative polarity can be achieved by studying the phase distributions, see Figure 9.4, where the charge per cycle vs. phase distribution, $\bar{q}(\varphi)$, is shown for 0.1, 1 and 10 Hz at 7 kV. It is clear that discharge activity occurs under advancing voltage slope of respective polarity and that the distributions of each polarity are similar, thus indicating internal discharges like voids or delaminations.
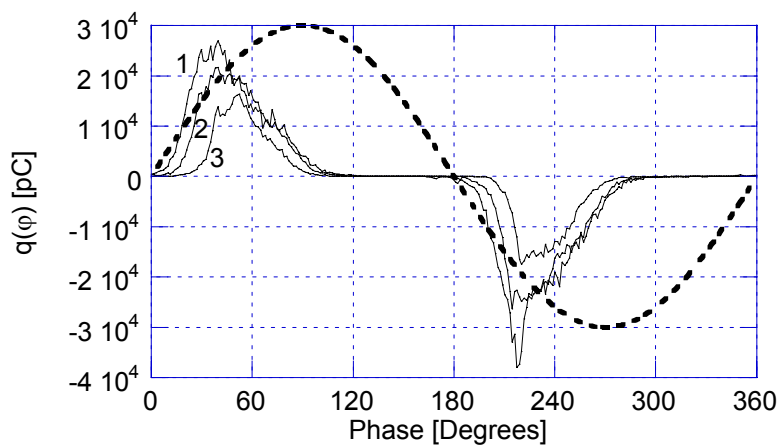

Figure 9.4 $\bar{q}(\varphi)$ for the stator bar obtained at 7 kV and for 1) 10 Hz, 2) 1 Hz and 3) 0.1 Hz. The curve for 100 Hz (not shown) is close to the 1 Hz curve.

The phase dependence of the PD-activity is not reflected in integrated quantities like total charge and numbers per cycle. Instead, the statistical moments for each discharge polarity may be considered, Chapter 5, or a harmonic expansion can be fruitful, Chapter 4.

The statistical moments are unreliable measures when the applied voltage is close to the inception. Therefore, 4 kV is omitted in the investigation and 5 kV is only initially considered to show the uncertainty in the statistical moments, Figure 9.5.

The mean discharge phase for positive discharges is shown in Figure 9.5, the result is clear: an increased voltage shifts the discharges earlier in phase, i.e. towards the zero-crossings. Accordingly, with decreasing frequency the discharges are shifted later in phase, i.e. towards the applied voltage peaks. Eventually there seems to be a minimum in the mean phase angle, which seems to occur at the frequency for maximum total charge per cycle, Figure 9.2. The reason behind that the discharge activity decrease with decreasing frequency is likely a reduced void field caused by the increasing influence of the surface conductivity in the delaminations.

The width of the phase distributions is measured with the standard deviation, Figure 9.6. It is clear that the distributions become wider at increased voltage since the applied voltage is above the inception voltage a larger portion of the phase. With decreasing frequency the distributions becomes narrower, which is a further consequence of a higher inception voltage at lower frequencies, due to a different field distribution.
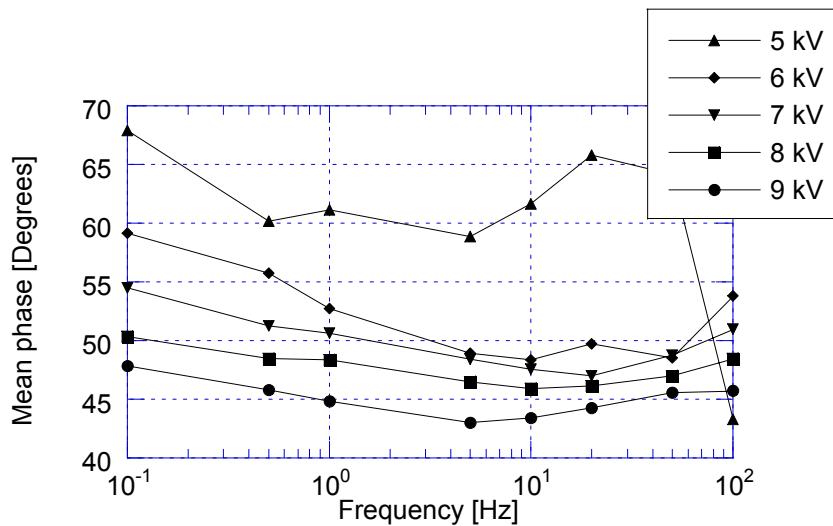

Figure 9.5 Mean discharge phase for positive discharges vs. frequency for voltages in the range 5 kV - 9 kV. 5 kV is close to inception and does not yield a relevant result.
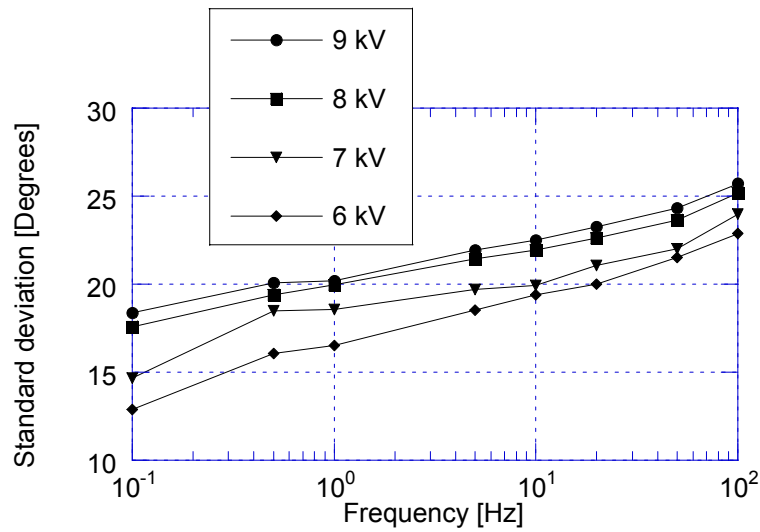
Figure 9.6 Phase standard deviation of positive discharges vs. frequency for voltages in the range 6 kV - 9 kV.

The skewness of the distributions is shown in Figure 9.7. The overall behaviour, independent of voltage, is that the skewness is positive and becomes more skewed with decreasing frequency. The positive skewness indicates that the distributions have a tail to the right, which is not too long since the values are less than 0.7. A triangular distribution has the skewness 0.57.
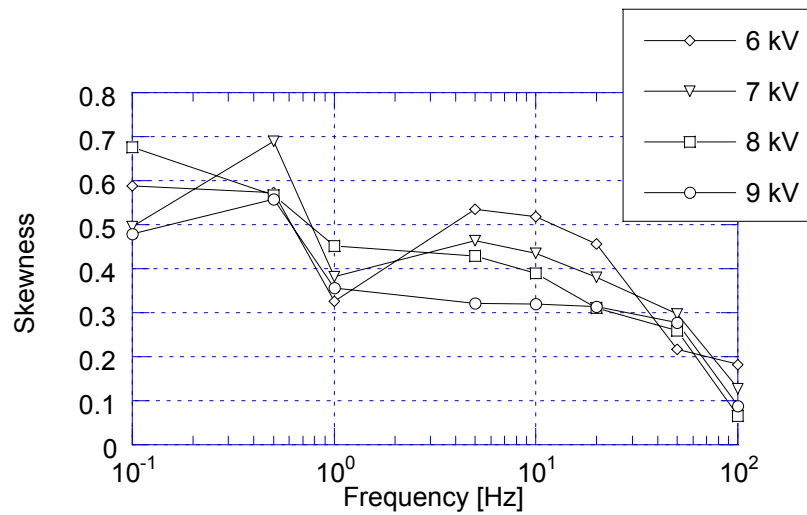

Figure 9.7 Phase skewness for negative discharges as a function of frequency for voltages in the range 6 kV - 9 kV.

111

The moments become more sensitive to discharges in the tail with increasing order, and are as such less useful. Nevertheless, the kurtosis, which is related to the fourth moment, is shown in Figure 9.8. The kurtosis is close to zero, except for 0.5 Hz where it deviates positively. This single point shows the sensitivity of this moment, because 0.5 Hz is not pronounced in the lower moments.
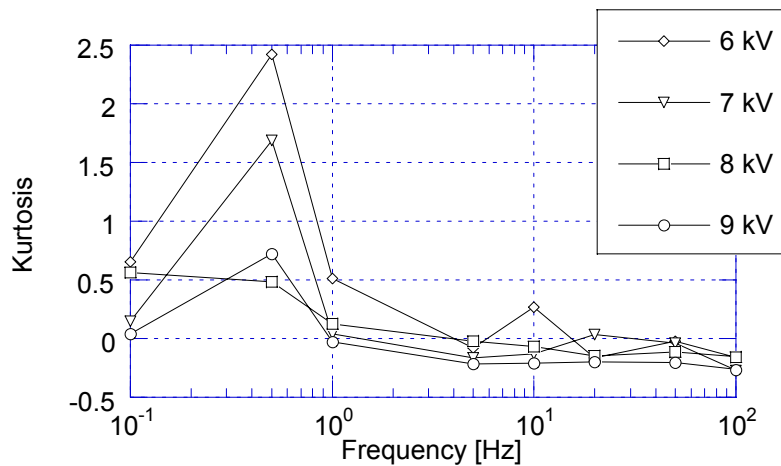

Figure 9.8 Phase kurtosis for negative discharges as a function of frequency for voltages in the range 6 kV - 9 kV.

9.3.2 Frequency dependence in the range 1 mHz - 100 Hz at 9 kV$_{peak}$

Previous result has been limited to the frequency range of 0.1 Hz - 100 Hz. However, some tests at 9 kV were performed in the low frequency region, i.e. down to 1 mHz. VF-PRPDA differs compared to dielectric spectroscopy of a deterministic current in the sense that it requires many more cycles for a reliable result. Here 50 applied voltage cycles have been used at 1 mHz, i.e. a measuring time of 14 hours for a single pattern, but could perhaps be reduced to 20 cycles (5.5 h) if the activity of PD is abundant.

The results for the frequency range 1 mHz - 100 Hz is shown as total charge per cycle, Figure 9.9 and total number of discharges per cycle, Figure 9.10. The basic trend is a continuous decrease with decreasing frequency until 5 mHz, where a minimum seems to appear. The decrease with decreasing frequency is similar in trend as observed for cable model 2 (CBM 2), Chapter 8, i.e. a structure with deliberately introduced band-gaps. The explanation is a higher PD inception voltage at lower frequencies, due to an increasing influence of the surface conductivity that decrease the field in the delaminations.

The reason behind the increase at 1 mHz could be that the field distribution at 1 mHz is governed by both the surface conductivity of the voids and of the bulk conductivity. The

recurrence of the cavities is then governed by a time-constant given by the cavity geometry and the bulk- and surface-conductivity, see Chapter 3.
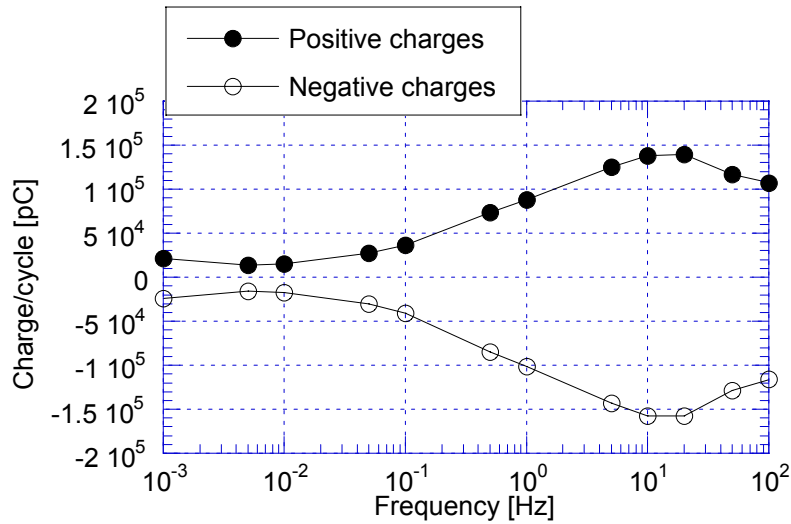

Figure 9.9 Total charge per cycle for positive (filled) and negative (unfilled) discharges vs. frequency at 9 kV.
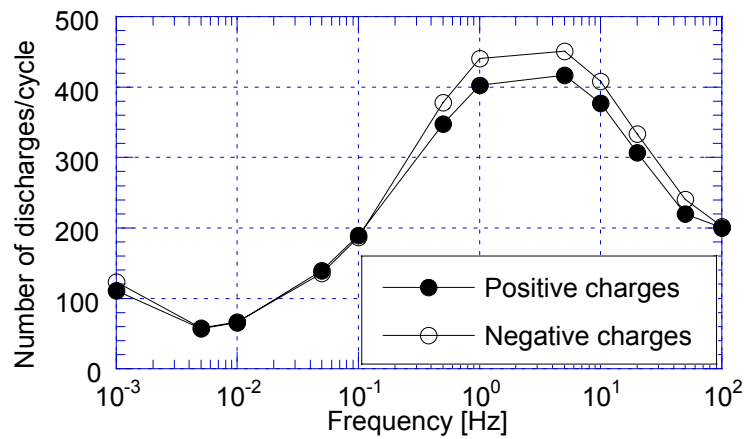

Figure 9.10 Total number of discharges per cycle for positive (filled) and negative (unfilled) discharges vs. frequency at 9 kV.

The mean phase of positive and negative discharges increase with decreasing frequency, Figure 9.11, thus the phase location of the discharge activity is shifted towards the peaks, which illustrates the increasing inception voltage at lower frequencies. However, a

maximum occurs at 10 mHz, i.e. close to the minimum in the charge per cycle and numbers per cycle.
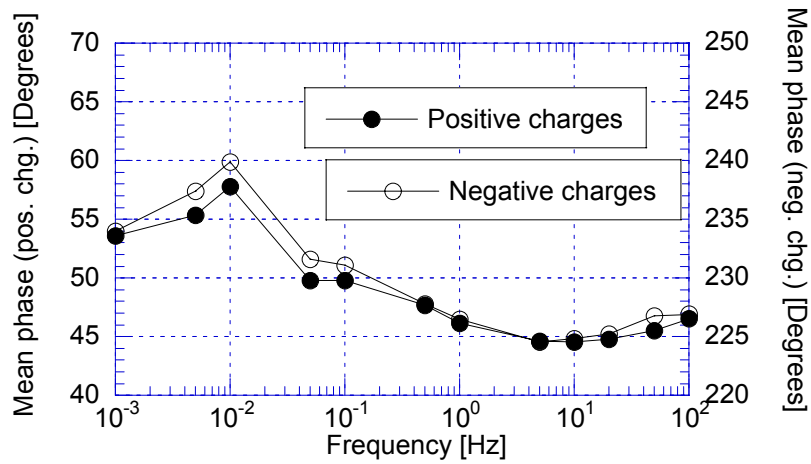

Figure 9.11 Mean phase for positive (filled) and negative (unfilled) discharges vs. frequency at 9 kV.

The standard deviation decreases monotonously, but saturates to 18 degrees below 0.1 Hz.
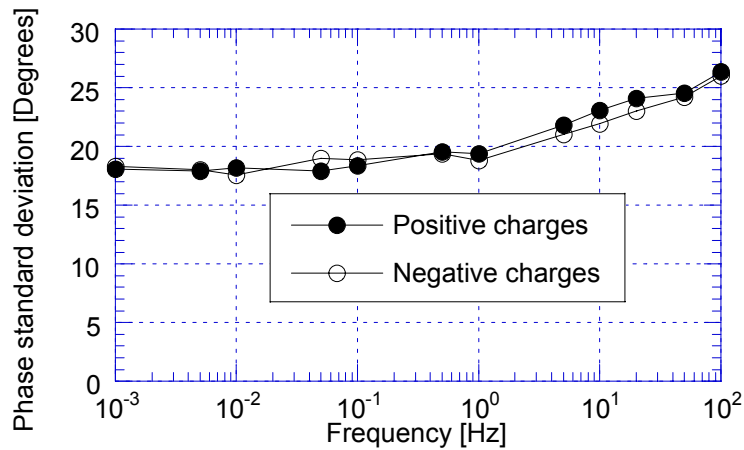

Figure 9.12 Phase standard deviation for positive (filled) and negative (unfilled) discharges vs. frequency at 9 kV.

The skewness, Figure 9.13 increases monotonously with decreasing frequency. However, the positive sign of the skewness is clearly an effect of that the tail is towards increasing phase angles from the mean. Nevertheless, the increasing magnitude of the skewness with decreasing frequency could be explained by the fact that the standard deviation decrease monotonously; thus it is not necessarily caused by a longer tail.
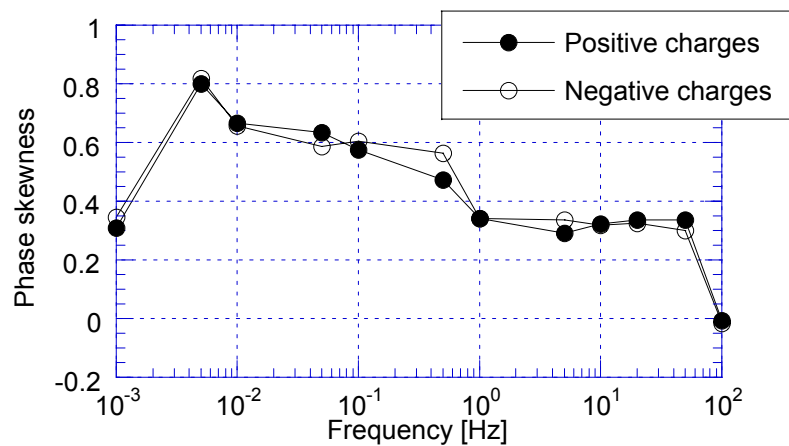

Figure 9.13 Phase skewness for positive (filled) and negative (unfilled) discharges vs. frequency at 9 kV.

The kurtosis, Figure 9.14, increases up to a plateau below 1 Hz and stays there except for the last point. The kurtosis is perhaps over-sensitive to minor changes of the PD activity, and as such is not in particular useful.
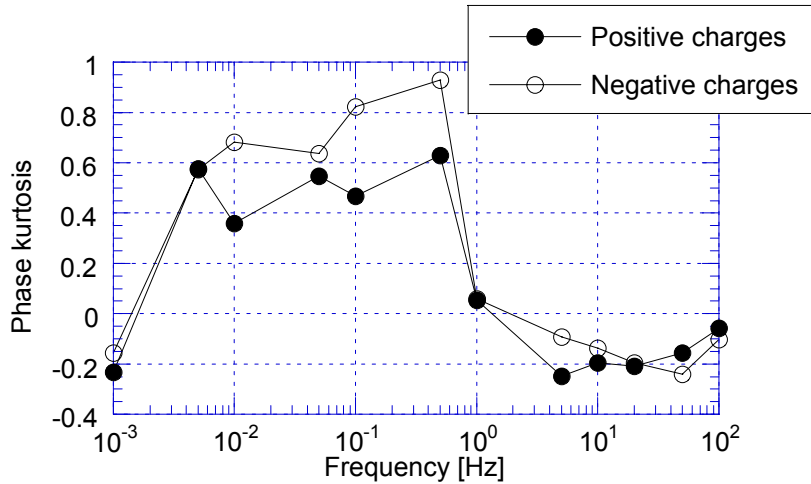
Figure 9.14 Phase kurtosis for positive (filled) and negative (unfilled) discharges vs. frequency at 9 kV.

9.3.3 Consecutive tests run at 9 kV for frequencies 0.1 Hz - 100 Hz

Eight consecutive runs were performed at 9 kV and in the frequency sequence from 100 Hz down to 0.1 Hz. Each run was completed within 1.5 h, i.e. 400 cycles of each frequency, whereas the next run followed immediately thereafter.

The result of the eight consecutive runs is shown as total charge per cycle in Figure 9.15 and as total number of discharges per cycle, Figure 9.16. The basic trend with consecutive runs is that the number of discharges decreases with time, which cause a corresponding reduction in total charge per cycle. The change is non-permanent since the "virgin curve" corresponding to Run 1 and the consecutive trend could be repeated if the bar is allowed some hours for relaxation.

The reason behind the trend is believed to be an increasing temperature at the surface in the delaminations, due to the progressive activity of PD. The increasing temperature will increase the surface conductivity in the delaminations, which cause a further reduction of the field at lower frequencies and less amount of charge per cycle. At higher frequencies, 10 Hz - 100 Hz, the field distribution is capacitively dominated and less sensitive to an increase of the surface temperature. Hence, the PD activity is not much affected in this frequency range by the surface temperature.
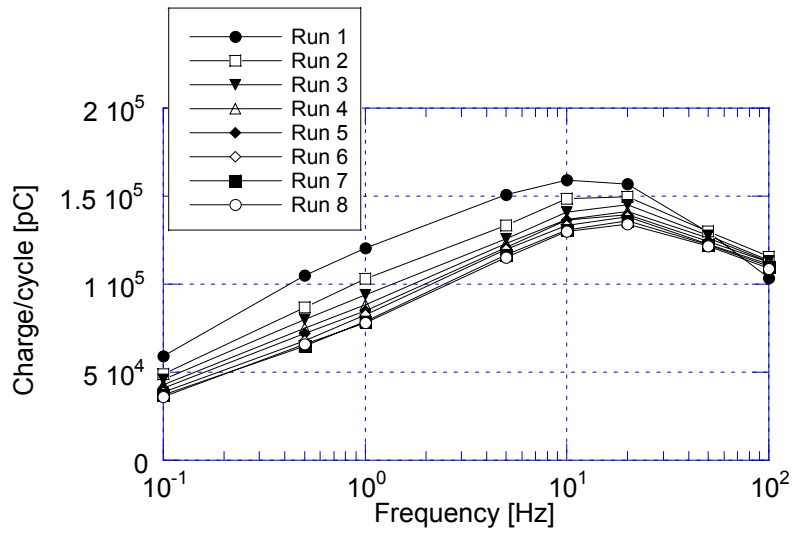
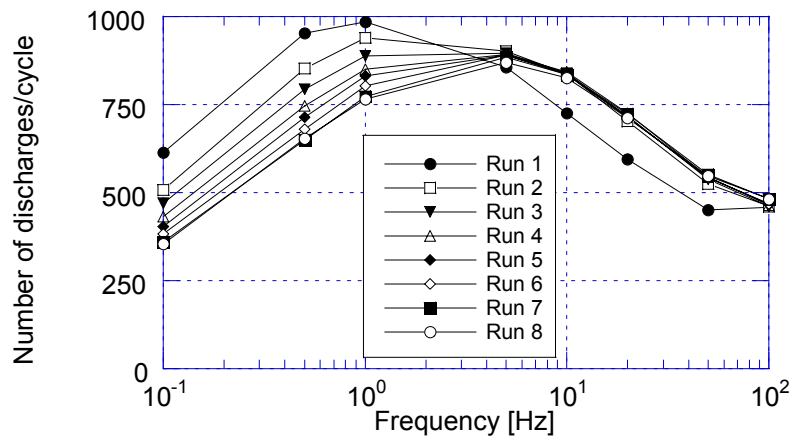*Figure 9.15 Total positive charge per cycle vs. frequency for eight consecutive runs at 9 kV.*

Figure 9.16 Total number of discharges per cycle vs. frequency for eight consecutive runs at 9 kV.

9.4 Conclusions

The partial discharge activity in an old stator bar of asphalt based insulation have been investigated with the VF-PRPDA technique in the frequency range 1mHz - 100 Hz.

The frequency dependence is similar at all voltages from inception voltage up to 9 kV, which indicate that it is one type of discharges at all voltages investigated.

The phase location of the partial discharges and the symmetry between positive and negative discharges indicate that the discharges come from delaminations or cavities.

The PD activity decrease with decreasing frequency below 1 Hz, a decrease that can be explained by that the field in the cavities is decreased by the conductive cavity surface at low frequencies.

10 Surface discharges

10.1 Introduction

The presence of a surface conductivity on void-surfaces is an important parameter in the reasons behind a frequency dependent PD-activity, Chapter 3, but also as a traceable parameter related to the ageing of insulation due to the progressive damage by PD [11, 12].

One type of discharges that are dependent on surface conduction and other surface properties are surface discharges along insulating surfaces. The VF-PRPDA technique is in this chapter applied on surface discharges with the intention to study how the frequency dependence of the PD-activity in the frequency range 0.1 Hz - 100 Hz is affected by the surface conductivity. The material presented here is an introduction to and a summary of the results presented in [40].

The surface conductivity of the film is altered by the adsorption of moisture from the ambient atmosphere of which the relative humidity is controlled. It is known from the literature that the surface conductivity of dielectric surfaces is related to the formation of monolayers of moisture on the surface [88]. However, the relation between the surface conductivity and the relative humidity must be determined for the particular insulating surface used in the experiment, see section 10.2.2.

The materials used in the investigation are muscovite mica, which is hydrophilic; polyimide (Kapton™), that is also hydrophilic (absorbs water) and polypropylene that is more hydrophobic.

The geometry adopted for generating surface discharges was the standardised geometry used in testing the resistance of insulating materials to breakdown by surface discharges [89]. That is a stainless-steel rod with a diameter of 6 mm resting on an insulating film with (here) a silver-painted back-electrode. The film is placed on a solid brass-electrode, which works as a contacting counter electrode.

10.2 Experimental

10.2.1 Equipment for controlling the ambient conditions

All experiments have been performed under controlled environmental conditions in a vacuum tight chamber made of stainless steel. A schematic picture of the test-setup is shown in Figure 10.1 and a photo of the test setup is shown in Figure 10.2. The double-walled chamber allows control of temperature by circulating heated or cooled water between the walls. The water is heated or cooled to desired temperature by a Haake K thermostat-bath. In the experiments performed here the thermostat-bath is mainly used to keep the temperature constant at 30 °C. The pressure of the gas could be controlled to

levels below atmospheric pressure, and is monitored by a Granville-Phillips 275 vacuum gauge. The dry gas is humidified by pumping the dry gas through a bottle with de-ionised water. The value of the relative humidity, and the temperature, is measured by a Delta-Ohm HD 9216 S combined temperature- and humidity-sensor mounted in the chamber.
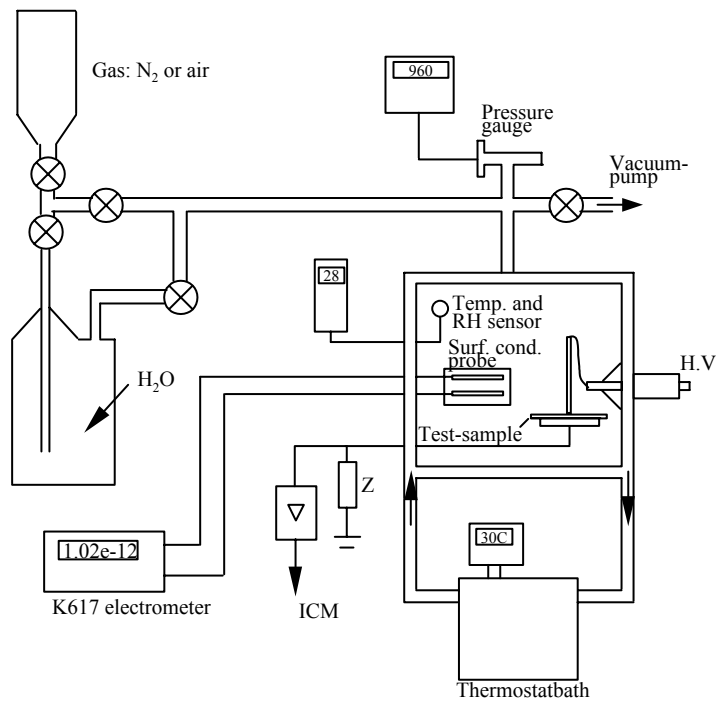

Figure 10.1 Test-setup for PD-experiments in controlled environment.
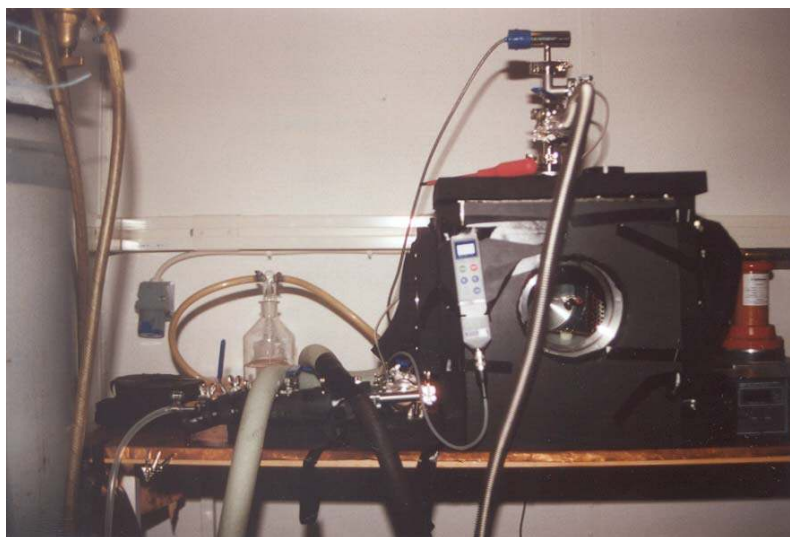
Figure 10.2 A photo of the test-setup for PD-experiments in controlled environment

Before settings of the test-gas, temperature and relative humidity, the chamber is evacuated down to a pressure below 0.1 Pa. Gas of either N_2 or synthetic air is then filled to desired pressure. The humidity level can not be exactly controlled beforehand, but is initially set to a high value, and a consecutive reduction of the humidity is done by evacuating an estimated amount of the humid gas and refilling with dry. After altering the humidity, the chamber must settle for around 12 - 18h before the forthcoming tests.

Figure 10.3 A photo of the test-cell for surface discharge studies.

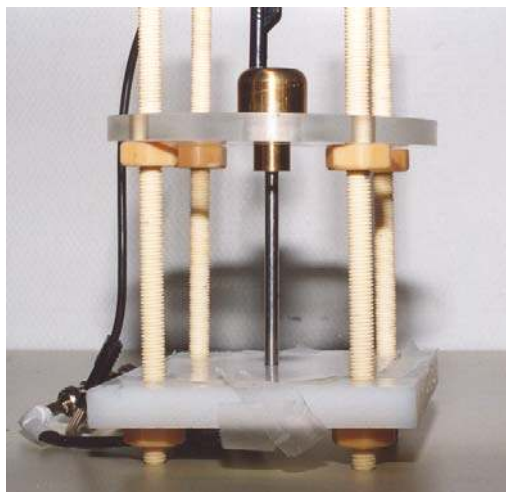## 10.2.2 Equipment for measuring surface conductivity

The transport of charge on insulating surfaces has rendered an extensive study during the last decades. A general source to the subject that contains many references is an article by T. J. Lewis in [90] where the tangential transport of charge in an adsorbed film of water is discussed as well as other charge transporting mechanisms.

Two different methods to measure the charge-flow are common. One method is to charge the insulating surface to a certain level by for example corona or tribo-electric charging. The time-decay of the deposited charge is then measured and is related to the surface conductivity [91, 92]. A second method, which is adopted here, is based on the measurement of the surface charging current flowing after the application of a DC voltage between two evaporated or painted electrodes [88, 93, 94]. The measuring electrodes adopted are two parallel strips of silver paint on each side of the sample, Figure 10.4. Electrodes are made on both sides of the sample, in order to cancel as much as possible of the field in the bulk.
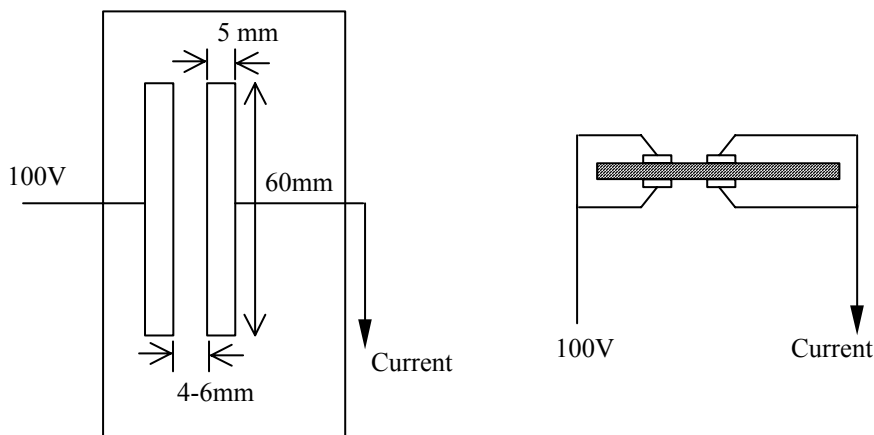
Figure 10.4 Surface electrodes and connections.

The measurement system used for measuring the surface currents is outlined in Figure 10.5. A programmable Keithley 617 Electrometer [78] that can resolve currents down to 100 aA, is used as the current measuring device. The applied voltage is generated by the internal voltage source of the electrometer, maximum ± 102 V and ± 2 mA, with an accuracy of ± (0.2 % + 50 mV). The rise-time of the output voltage is limited by the maximum output current, and thus by the capacitance connected to the output. This capacitance must be kept as low as possible if a short settling time is required. However, the lowest settling time that can be reached is set by the instrument and is ≤ 3 ms.

Keithley 617 Electrometer rear panel   Chamber (shield)

Figure 10.5 Experimental system for measuring surface conductivity.

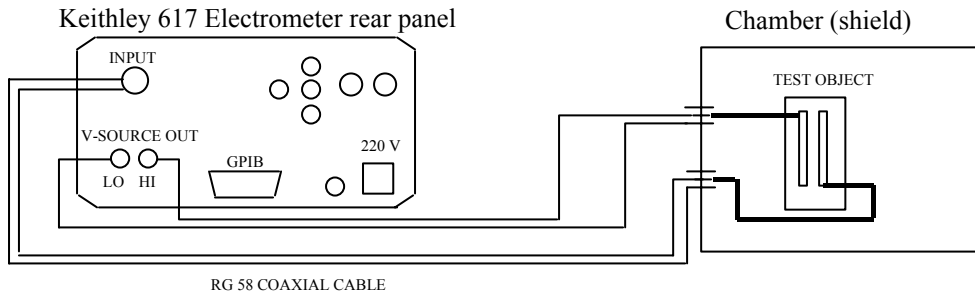The surface conductivity, σ_s is taken from the final value of the surface charging current after an 'infinitely' long charging time. However, an estimate of the surface conductivity has been taken by the charging current values in the end of the charging period (10.1). The charging time in these investigations was 1136 s (for programming simplicity).

$$\sigma_s = \frac{d}{l} \cdot \frac{i_{Chg}(t \to \infty)}{V_{Chg}} \approx \frac{d}{l} \cdot \frac{i_{Chg}(1136s)}{V_{Chg}} \, [\Omega^{-1}]$$
(10.1)

The surface resistance, $R_\square$ [Ω] is defined as $1/\sigma_s$.

Both the charging current and the consecutive discharging current are measured. The existence of a discharging current is a consequence of that the surface charging current is not a pure conductive current [5].

10.2.3 Samples

The materials used in the investigation are mica, polyimide (Kapton™) and polypropylene, Table 10.1.

The permittivity, $\varepsilon_r'(\omega)$ of the dielectric sample is one of the parameters that control the field distribution along the dielectric surface and if the permittivity varies with frequency then it may be an origin to a frequency dependent PD activity. The permittivity of the dielectric films was measured under atmospherical conditions with the IDA-system [27]. It was found that the dispersion in $\varepsilon_r'(\omega)$ is less than 10 % in the frequency range 1 mHz - 1000 Hz for all materials, the values are given in Table 10.1.

Table 10.1 Dielectric samples used for studying surface discharges

Material	Thickness [μm]	$\varepsilon_r'(\omega)$ [-]	Wettability
Muscovite mica	130	9	Hydrophilic
Polyimide (PI)	130	3.35	Hydrophilic
Polypropylene (PP)	300	2.3	Hydrophobic

10.3 Experimental results

10.3.1 Surface currents and surface conductivity

The charging currents obtained for mica with 100 V charging voltage, and silver-painted electrodes of the size 60 x 5 mm and an electrode separation of 4 mm are shown in Figure 10.6. The consecutive discharging currents are shown in Figure 10.7. The charging currents decay slowly with time, which also have been observed by Jonscher and Ramdeen [93]. That is a Curie-von Schweidler exponential law t^{-n}, $0 < n < 1$, where the exponent n is small compared to one. The existence of a non-vanishing discharge current, Figure 10.7, together with the slowly decaying charging current is a manifestation of a dispersive process different from pure conduction; i.e. process that corresponds to a low-frequency dispersion (LFD) in frequency domain. The physical explanation of LFD is not clear, but for the particular case with humid insulating surfaces an explanation related to an electrochemical process is proposed by Jonscher [5].
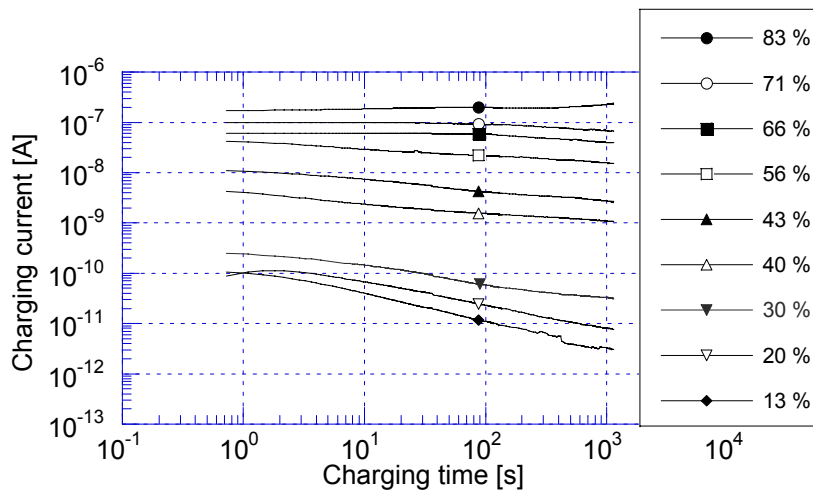
Figure 10.6 Charging-currents obtained for mica with 100 V charging voltage and 1136 s charging time under different relative humidities.

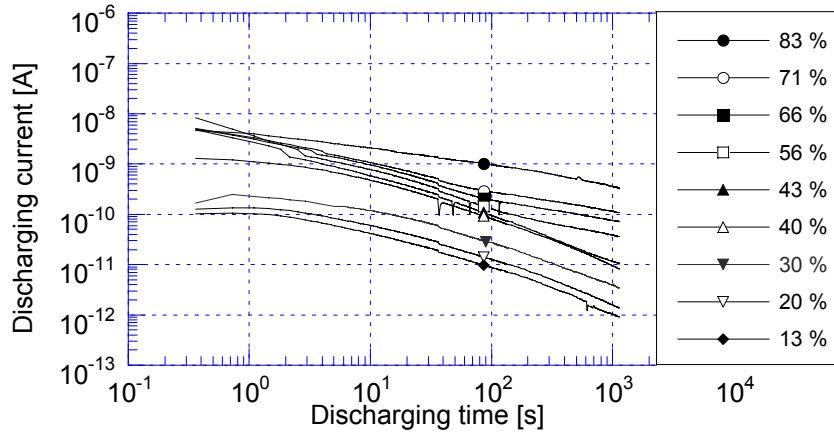*Figure 10.7 Discharging-currents obtained for mica under different relative humidities after charging with 100 V during 1136 s.*

The measured surface conductivity versus relative humidity for muscovite mica, polyimide and polypropylene is shown Figure 10.8.
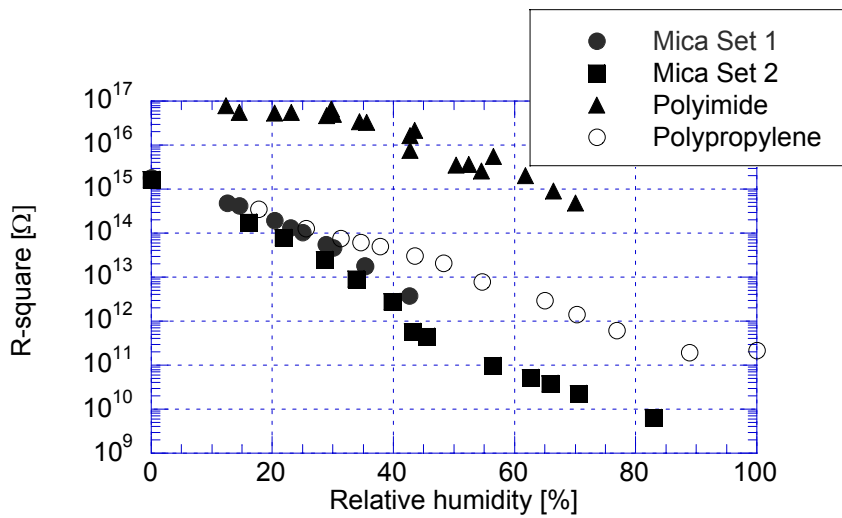

Figure 10.8 Surface resistance for mica, polyimide, and polypropylene as a function of relative humidity. Temperature = 30 °C.

125

Mica

There is a distinct increase in the charging current for mica, Figure 10.6, between the 30 and 40 % RH levels. It is believed that this increase has its origin in the formation of the first monolayer of moisture as shown by Hu et al [95]. The corresponding decrease in $R_\square$ is apparent, Figure 10.8 (Mica Set 2).

Polyimide

The surface resistance polyimide is much higher than for mica and polypropylene in the same range of humidities. The decay for polyimide in $R_\square$ between 10 % RH and 70 % RH is about two decades. A similar increase in surface conduction current between 10 % and 83 % RH for polyimide has previously been reported by Centurioni et al [96]. However, the data in [96] is presented as surface currents without any reference to applied voltage and exact geometry, and an exact comparison is therefore not possible. The degree of hydrophilicity (absorption of water) of polyimide is discussed by Bozzo et al [97], where it is reported that polyimide absorbs 2.9 weight % water (Room temperature, $RH > RH_c \approx 45$ % [96]), compared to for example 0.4 % for poly-ethylene-terphtalathe (PET), but up to 9 % for polyamide 6 (PA 6). This absorption does not affect the surface resistance much as seen in Figure 10.8. However, the absorption of moisture causes an increase of the permittivity and the dissipation factor as shown by Yasufuku and Todoki [98]. It is reported in [98] that the relative permittivity increases from 3.0 to 5.4 (23 °C, 300 Hz) and the dissipation factor (ε_r'') from $1 \cdot 10^{-3}$ to 0.1, when the moisture content increases from vacuum dried sample to saturated water content (3.3 weight %, *cf.* 2.9 % above). However, the bulk properties of the polyimide sample used have not been investigated as a function of moisture content. However, it is not unlikely that the bulk properties of polyimide have a stronger influence on the frequency dependence of PD at variable humidity than the surface conductivity.

Polypropylene

Polypropylene showed a surface resistance similar to mica at low humidities, but is higher at higher humidities, probably due to a less ability to adsorb moisture.

Polypropylene is a fairly hydrophobic surface as seen in Figure 10.9 [99, p. 304], i.e. it is not easily wetted by water. The degree of wettability of any liquid on a surface is often measured with the contact angle between the surface and a droplet of the liquid [99, p. 166], which then may be related to the surface tension of the sample [99, p. 182]. When the liquid is water, this surface tension is a measure of the hydrophobicity or hydrophilicity of the surface. A low surface tension indicates a hydrophobic surface and a high surface tension a hydrophilic surface. However, to what degree the hydrophobicity correlates to the surface conductivity is not clear.
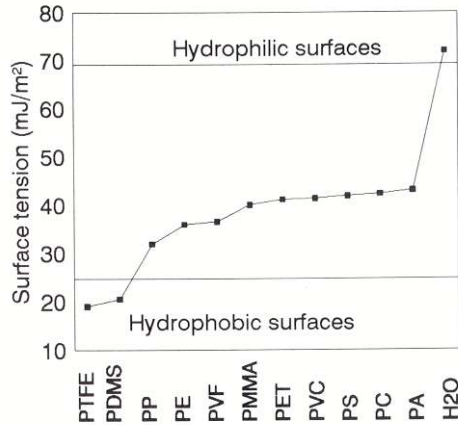
Figure 10.9 Surface tension of common polymers and water, from [99, p. 304]

10.3.2 VF-PRPDA results

The experimental results obtained for mica, polypropylene and partly for polyimide are presented in [40] and only a summary of the results are given. However, some additional results for polyimide are supplied. The results presented are based on the total charge/cycle, $Q_{Tot}(\omega, V_0)$.

The discharges that occur may be of three different types, all starting from the triple-junction between gas, electrode and dielectric surface. At voltage levels close to inception, the origin seems to be the wedge between the electrode and the sample, or the edge of the electrodes. These discharges will at higher voltages start to propagate in the field along the surface, and form surface streamers. The results presented here are restricted to the high-voltage region where both surface streamers and the unavoidable small wedge- or edge-discharges occur. The inception voltage in dry in N_2 are for all three samples is in the range 1.2 kV - 1.5 kV, and is in principle frequency independent, i.e. the wedge or edge discharges. The experiments performed at the highest humidity require voltages of up to 8 kV, thus more than six times the inception voltage.

10.3.2.1 Mica

The results for mica in dry N_2 is shown in Figure 10.10 a). The non-linear increase with applied voltage is a consequence of the surface streamer discharges [40]. The activity has a peak around 20 Hz, where the increase from 100 Hz down to 20 Hz is likely due to a reduced influence of the statistical time-lag. The decay below the peak is due to a reduction in magnitude of the PD [40], probably caused by a reduction in the tangential field due to a resistive field-grading.

127

The PD-activity at different humidities is shown in Figure 10.10 b). It is shown that the PD-activity decays with increasing humidity; however, the decay with increasing humidity is not strictly monotonous. With decreasing frequency at 7 kV the activity cease around 2 Hz for 75 % RH, around 0.5 Hz for 56 % RH, but does not disappear at all for 22 % RH and dry atmosphere. The likely explanation is that the increased surface conductivity with increasing humidity lowers the surface field component too levels below the PD inception field. The frequency where the PD extinguishes is dependent on the relative humidity and the applied voltage.
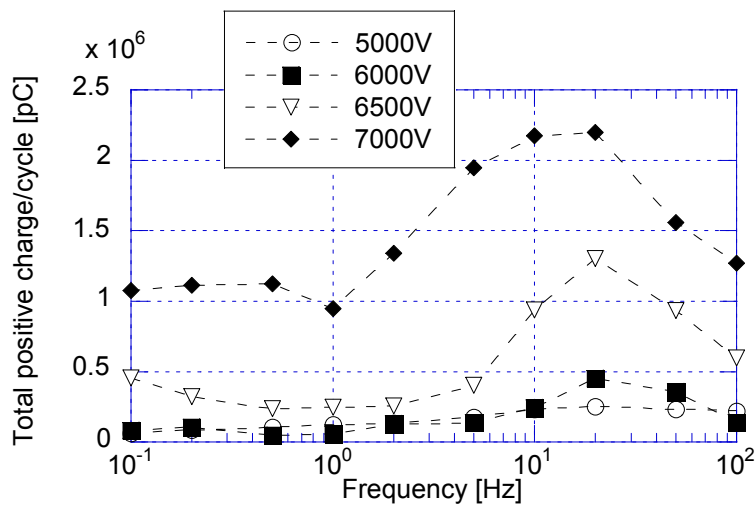
a)
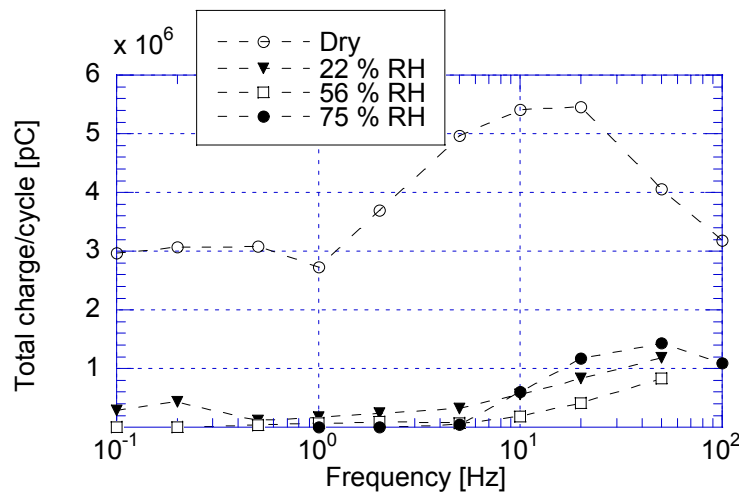
b)

Figure 10.10 Total charge per cycle vs. frequency for surface discharges on mica in N_2. a) Dry conditions 5, 6, 6.5 and 7 kV. b) 7 kV and 0, 22, 56 and 75 % RH.

10.3.2.2 Polyimide

For polyimide, the activity at 79 % RH shows a behaviour similar to humid mica at 56 - 75 % RH, but for lower humidities the tendency is a growing discharge activity with decreasing frequency, Figure 10.11 a). This increase in charge with decreasing frequency is due to an increase in the number of discharges, a tendency that could be explained by the fact that there are only wedge discharges. The higher repetition rate is explained by a fast relaxation of deposited charges, e.g. similar to pure corona discharges.

The difference in total charge per cycle between 6 kV and 8 kV at 79 % RH is shown in Figure 10.11 b). It is clearly visible that the discharge activity remains to lower frequencies at 8 kV than at 6 kV. This trend can be related to the surface field grading as explained for mica, but is not supported by the fairly high surface conductivity, Figure 10.8. Instead the extinguish of the PD may be related to an increased bulk conductivity.
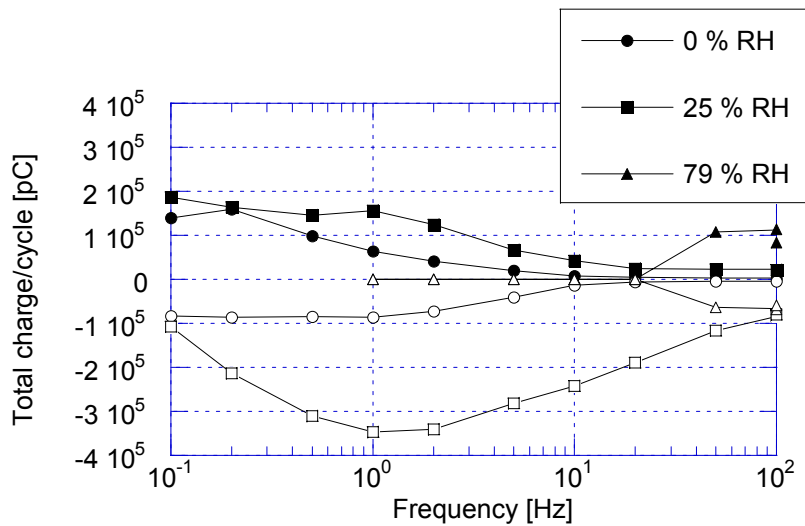
a)
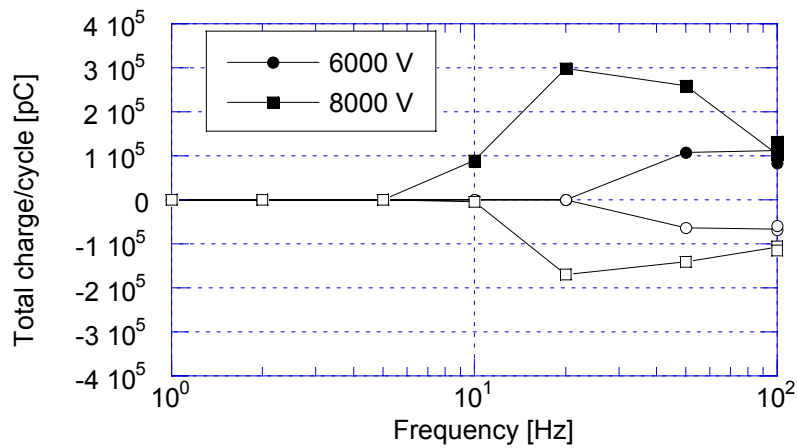
b)

Figure 10.11 Total charge per cycle vs. frequency for surfaces discharges on polyimide in
N_2 a) 6 kV; 0, 25 and 79 % RH and b) 79 % RH; 6 kV and 8 kV. Open symbols = negative
polarity and filled symbols = positive polarity.

10.3.2.3 Polypropylene

For polypropylene in dry N_2, a monotonous increase of total charge per cycle with
decreasing frequency is observed, Figure 10.12 a). The frequency dependence is similar for
all voltages in the range 3 kV - 6 kV, thus implying that it is the same discharge mechanism
over this voltage range. The increase with decreasing frequency from 100 Hz to 10 Hz is
explained by the statistical time-lag. The almost frequency independent discharge activity
between 1 and 10 Hz, indicates that the origin could be wedge-discharges. The further
increase from 1 Hz down to 0.1 Hz are caused by a change from small discharges to larger
discharges [40]. The occurrence of larger discharges could perhaps be caused by an
accumulation of charge on the dielectric surface at one polarity, with a consecutive large
back-discharge after polarity reversal of the surface field [100].

Under humid conditions, Figure 10.12 b), there is a higher discharge activity at 56 % RH
compared to dry conditions over the frequency range 0.1 Hz - 100 Hz. This increase is
caused by an increase in number of discharges, rather than an increased magnitude of the
single discharges [40]. No extinguish of PD is observed up to 56 % RH, an observation
partly explained by that the surface conductivity is not high enough. Another explanation
could be related to the fairly high hydrophobicity of the polypropylene surface. Since the
moisture is less bounded to the surface for a hydrophobic surface it may be easy to remove
by the surface discharge, i.e. a dry-zone may be formed around the high potential rod that
restores that part of the surface to the dry state. Although, the situation is not similar to the
dry situation because the surface outside the dry zone is humid.

130

a)

b)

Figure 10.12 Total charge per cycle vs. frequency for surface discharges on polypropylene in N$_2$. a) Dry conditions 3, 4, 5 and 6 kV. b) 6 kV and 0, 22 and 56 % RH.
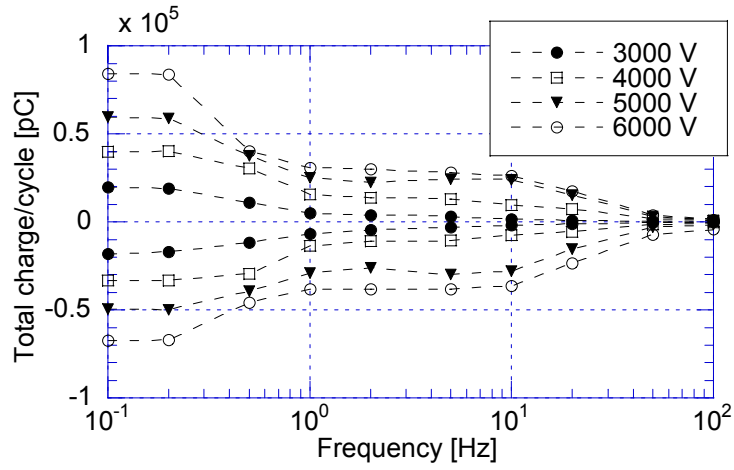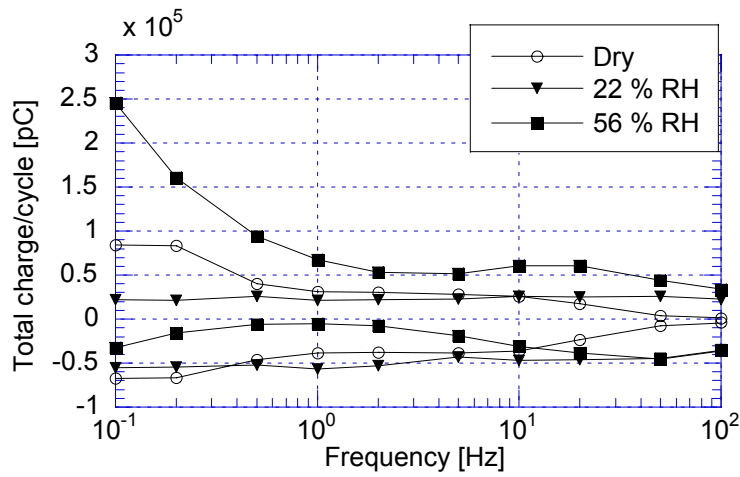
10.4 Conclusions

The surface conductivity on insulating surfaces is strongly dependent on the humidity of the ambient atmosphere. The hydrophilic mica has a surface resistance that decay with over five decades in magnitude when the relative humidity varies from dry to 80 % RH. Polyimide, even if hydrophilic, has a surface resistance, $R_\square$ of 10^{17} Ω at 10 % RH and decays with two decades until 70 % RH.

The frequency dependence of PD on humid mica is likely controlled by the field grading caused by the humidity dependent surface conductivity.

The frequency dependence of PD for polyimide is similar to mica at high humidities. However, for polyimide the dependence is more likely caused by a bulk effect rather than surface conduction.

The total amount of charge per cycle for dry polypropylene grows with decreasing frequency. This feature is kept even at 56 % RH and could be related to a formation of a dry-zone around the high potential rod.

11 Oil paper insulated cable

11.1 Introduction

In this chapter, PD in an old oil-paper insulated cable (PILC), i.e. a mass impregnated AC-cable, have been studied with the VF-PRPDA technique and by simultaneous measurements with dielectric spectroscopy. Moreover, the influence of the temperature upon the PD-activity has been studied in the range 20 - 60 °C.

A PILC cable, with paper tapes impregnated with oil and lapped around the conductor, is in general not a PD-free construction. The first discharges are supposed to come in cavities formed when the cable is thermally cycled by a load cycling. At high temperatures, i.e. high currents, the pressure in the cable is built up due to thermal expansion of the insulation, with the consequence that the lead sheath will expand if the mechanical stress becomes large enough [101]. With decreasing load, the temperature will fall, and since the insulation shrinks faster than the lead, ultimately a gap or cavity will occur. In this gap, an activity of PD will easily start, which may lead to a progressive deterioration. Another source is the butt gaps between the paper tapes, which may become voids if the oil is drained from the gap.

Today mass impregnated cables are successively replaced with XLPE-cables, but still a large amount of the distribution cables are mass impregnated. One example is the 11 kV distribution network in Gothenburg, Sweden [102], which in 1995 consists of 1460 km paper insulated cables, 301 km XLPE cables and 260 km overhead lines. Thus, the mass impregnated cables are still dominating in the distribution network, with the oldest parts from 1907. The investment in such a distribution network is tremendous, and it is of a high economic interest to utilise as much as possible of the existing mass impregnated cables before replaceing with XLPE. In order to ensure a good reliability of the existing network, and to achieve an economic and well-planned maintenance and replacement strategy, it would be fruitful to have a method for ranking of the cable ageing and suffering due to PD.

In order to achieve a quality assessment of their cable network, Göteborg Energi Nät AB (GENAB) investigated their cable network by a PD-mapping method from EA Technology [103]. During these investigations, some mass impregnated cables that suffered by PD were replaced and two suitable cables were supplied to KTH and Dept. of Electrotechnical Systems, of which one of the cables have been used in the investigations presented here. The material presented is partly a result of a diploma project performed by Joacim Sköldin under the supervision of the author [81]. Previously, other pieces of the cable have been investigated by Neimanis [7] to study the relation between characteristics of the dielectric spectrum and the moisture content in the paper.

11.2 Cable data

The mass impregnated cable used was a piece of a 10 kV, 3 x 120 mm^2 Cu cable, manufactured in 1948 by Sieverts Kabelverk, installed in Gothenburg 1949, and replaced in 1998. The cable has been given the name L764 as in the original network. The cable cross-section is shown in Figure 11.1 and some construction data are given in Table 11.1.
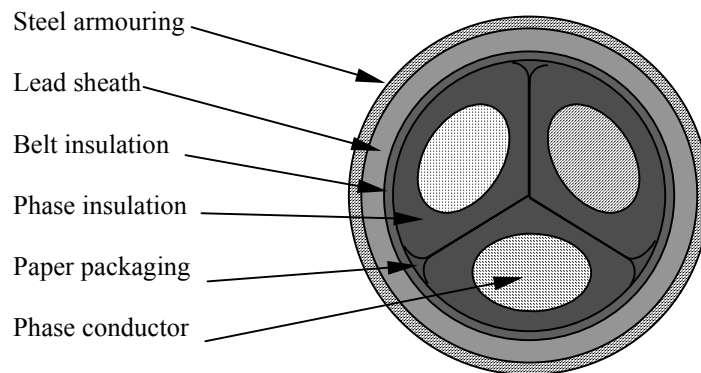
Figure 11.1 Cross-section of L764.

Table 11.1 Parameters of the mass impregnated cable [7]

Property	Specification
Network installation name	L764
Type	FCJJ
Conductor material	Cu
Conductor area	120 mm^2, Oval shape
Belt insulation	
Number of layers	5
Paper width $\times$ thickness	38×0.16 mm^2
Phase insulation	
Number of layers	14
Paper width $\times$ thickness	25×0.16 mm^2

PD measurements were performed on-site 1995-05-18 and 1996-08-22, by FEKAB/EA Technology, for which the measurements are shown in Figure 11.2 and Figure 11.3. The first measurement indicated PD from 4.5 kV$_{rms}$ of magnitudes 2000 - 5000 pC, depending on phase and location; the second measurement showed PD starting at 6 kV$_{rms}$ with magnitudes in the range 900 - 2600 pC. These variations, may be due to differences in temperature or could be due to normal scatter.

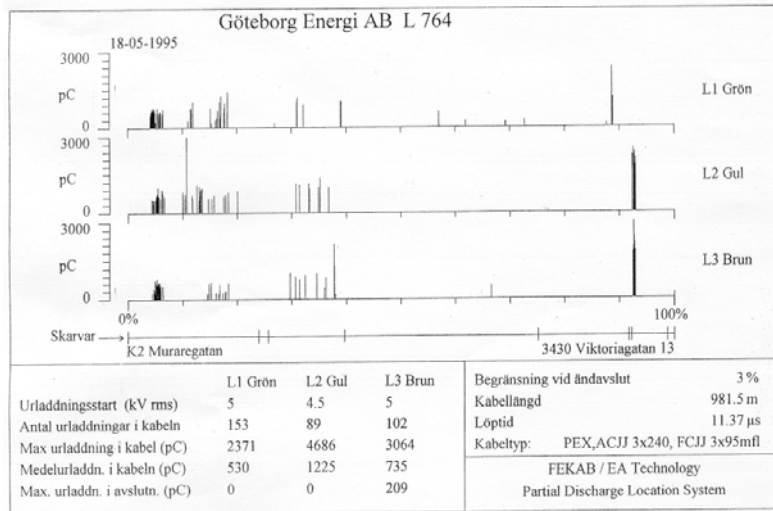|	L1 Grön	L2 Gul	L3 Brun		
Urladdningsstart (kV rms)	5	4.5	5	Begränsning vid ändavslut	3 %
Antal urladdningar i kabeln	153	89	102	Kabellängd	981.5 m
Max urladdning i kabel (pC)	2371	4686	3064	Löptid	11.37 µs
Medelurladdn. i kabeln (pC)	530	1225	735	Kabeltyp: PEX,ACJJ 3x240, FCJJ 3x95mfl	
Max. urladdn. i avslutn. (pC)	0	0	209	FEKAB / EA Technology	
				Partial Discharge Location System	

Figure 11.2 PD-measurements performed 1995-05-18 on L764 by FEKAB/EA Technology. Published by permission from Göteborg Energi Nät AB (GENAB) .

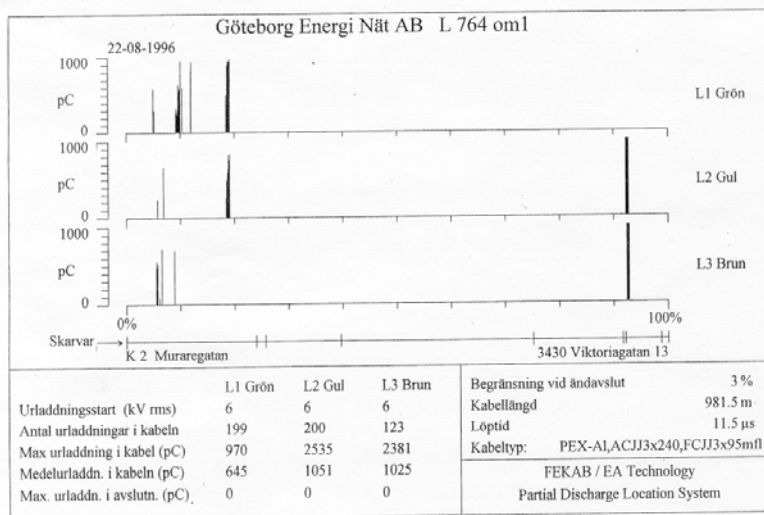|	L1 Grön	L2 Gul	L3 Brun		
Urladdningsstart (kV rms)	6	6	6	Begränsning vid ändavslut	3 %
Antal urladdningar i kabeln	199	200	123	Kabellängd	981.5 m
Max urladdning i kabel (pC)	970	2535	2381	Löptid	11.5 µs
Medelurladdn. i kabeln (pC)	645	1051	1025	Kabeltyp: PEX-Al,ACJJ3x240,FCJJ3x95mfl	
Max. urladdn. i avslutn. (pC)	0	0	0	FEKAB / EA Technology	
				Partial Discharge Location System	

Figure 11.3 PD-measurements performed 1996-08-22 on L764 by FEKAB/EA Technology. Published by permission from Göteborg Energi Nät AB (GENAB).

Two 2.5 m long pieces of L764 was subjected to further investigations with the VF-PRPDA technique. The first piece, *Sample 1*, is taken from the end of the cable and was supplied with commercial Raychem cable terminations, mounted by personnel from Birka Energi, who also supplied the terminations. Another piece, *Sample 2*, was taken next to Sample 1, but was not terminated by a commercial termination. Instead a first attempt was made with ABB-Kabeldon stress grading pad wrapped around the end and fixed with ABB-Kabeldon IV-tape. This procedure was unsuccessful in that it did not yield a PD-free termination. The cure was to immerse the cable ends in transformer oil, which ensured a PD-free termination for the voltages applied.

All measurements were performed by applying a voltage across the insulation between the three phases joined together and the lead sheath; i.e. part of the phase insulation and the belt insulation was stressed by the applied field.

The two samples was initially compared by measuring the dielectric spectrum of the cables at a voltage level below the PD-inception voltage, the result is shown in Figure 11.4.
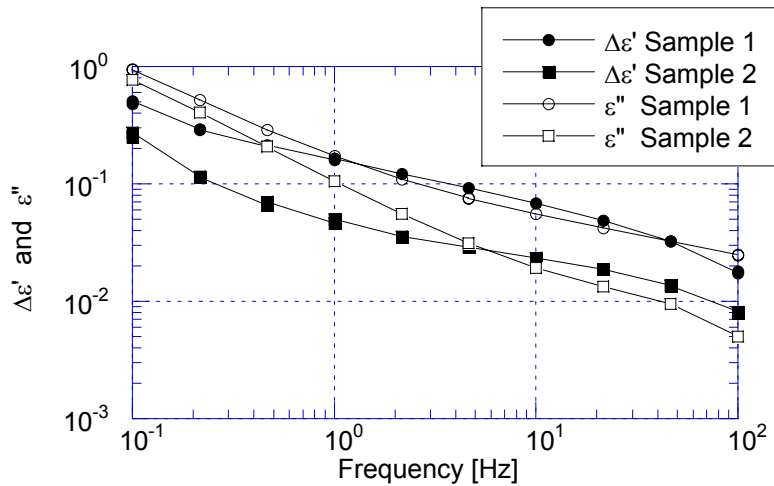

Figure 11.4 $\Delta\varepsilon_r'$ and ε_r'' measured for Sample 1 with commercial Raychem termination and Sample 2 without any termination at 1000 V_{rms}.

As clearly seen, $\Delta\varepsilon'$ and ε'' are higher for Sample 1 than for Sample 2. This behaviour is here explained by higher moisture content in Sample 1 than in Sample 2. According to Neimanis [7, p. 133], the moisture content in Sample 1 should be around 2.8 %, whereas Sample 2 should have a moisture content of less than 1 %.

11.3 Sample 1

11.3.1 VF-PRPDA of Sample 1 at 25 °C

The VF-PRPDA was performed on Sample 1 at different voltage levels, in order to investigate what a suitable voltage level for further analysis could be. The results are shown as total charge per cycle in Figure 11.5.
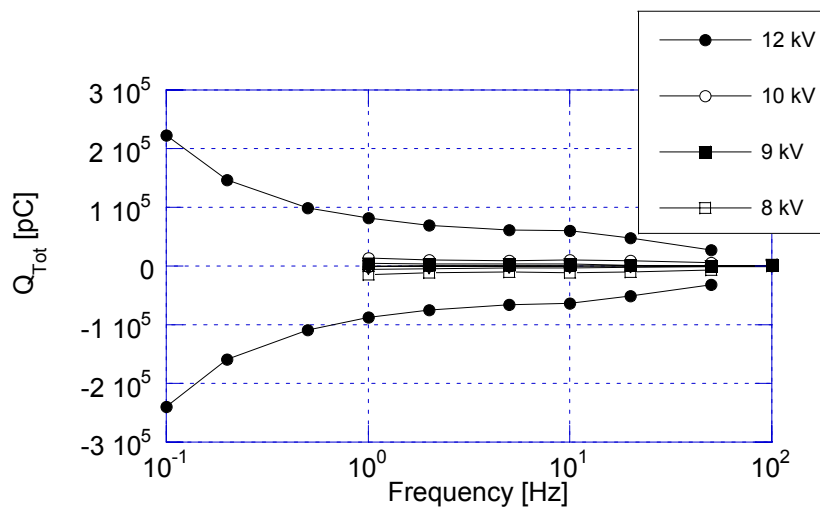

Figure 11.5 Total amount of positive and negative charge per cycle for Sample 1 at 25 °C and 8, 9, 10 and 12 kV.

Several properties are evident: first, there is a clear symmetry between positive and negative discharges, and secondly, there is a distinct difference in PD-activity between 10 and 12 kV. The symmetry between positive and negative discharges is manifested by the phase-distributions obtained. The distributions at 12 kV and for frequencies in the range 0.1 Hz - 50 Hz are shown in Figure 11.6. The discharge activity grows monotonously with voltage, therefore only curve 1 and 7 to 9 are denoted. The sign of the charge is reversed since the measurements were performed with the aid of a coupling-capacitor.
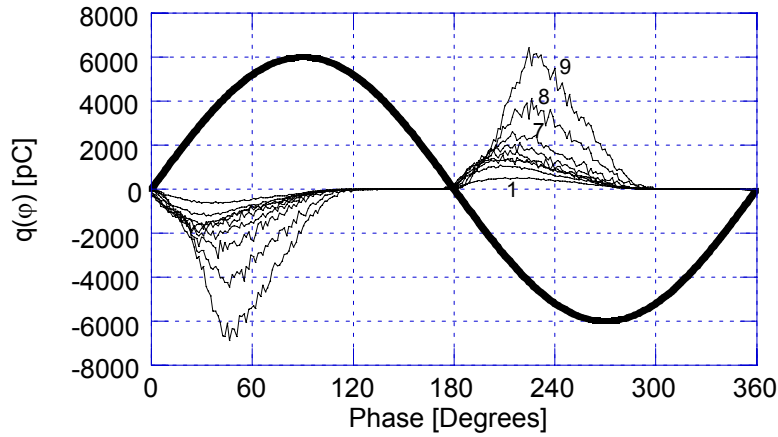
Figure 11.6 $\overline{q}(\varphi)$ for Sample 1 at 12 kV and 25°C. 1 - 9: 50, 20, 10; 5, 2, 1; 0.5, 0.2 and 0.1 Hz

The symmetry between positive and negative discharges, together with phase-location on mainly increasing voltage slope clearly indicate that the origin of the discharges are cavities within the cables, e.g. due to butt-gaps between paper-bands, or a gap between the insulation and the lead sheath.

The spread in magnitude is studied by the magnitude distributions, N_q^+ and N_q^-, shown in Figure 11.7 for the 12 kV case and different frequencies. The increase in magnitude is monotonous, and a great majority of the discharges are below 500 pC in magnitude, which is around 25 % of the maximum discharge magnitude. The relative difference in magnitude between N_q^+ and N_q^- is negligible because the amplitudes in a histogram are sensitive to in which channel the actual discharge is counted.
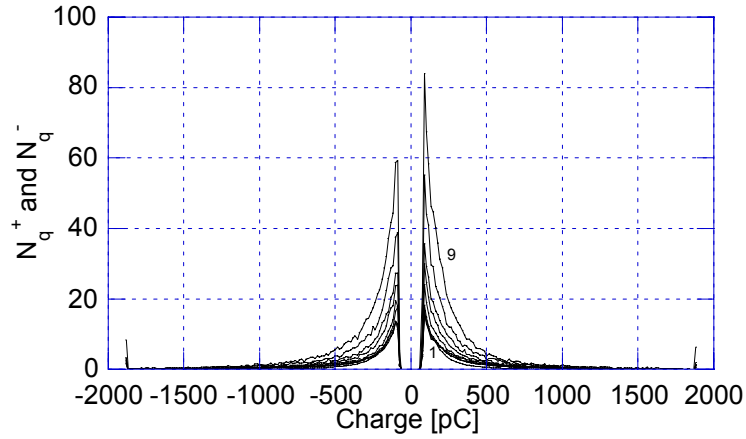
Figure 11.7 N_q^+ and N_q^- for Sample 1 at 12 kV and 25 °C. 1 - 9: 50, 20, 10; 5, 2, 1; 0.5, 0.2 and 0.1 Hz.

The main observation of the frequency dependence is that there is an increasing activity of PD with decreasing frequency measured as total charge/cycle, Figure 11.5. This increase is caused by a larger number of discharges at low frequencies, rather than an increase in the magnitude of the single discharges, Figure 11.7. The influence of the statistical time-lag is always pointing to an enhanced probability of PD at decreasing frequencies. However, the supply of start electrons seems to be ensured at 12 kV due to the large number of discharges that really appears, and will not explain the increasing PD-activity with decreasing frequency.

Partial discharges in mass impregnated paper insulation have been studied extensively for DC voltages, see e.g. Densley in [36], and it is likely that the phenomena that appear under DC voltage becomes relevant at frequencies low compared to the power frequency.

In the following, a model used by Jeroense and Kreuger [104], and later by Jeroense, Bergkvist and Nordberg [105] will be adopted for intuitive explanations of the behaviour of PD at low frequencies. The cavity and the discharge-free material are represented with a modified a-b-c model, Figure 11.8. C_a and R_a represent the capacitance and the resistance of the discharge-free insulation, and similarly for C_b and R_b for the insulation in series with the cavity. C_c is the capacitance of the cavity and R_c models an existing surface resistance of the cavity.
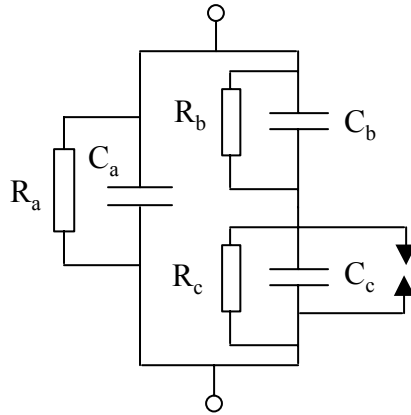
Figure 11.8 A modified a-b-c model used for describing PD under applied DC voltage [104,105].

After a discharge of the cavity under DC, the voltage across the cavity will recover with a time constant, τ_{rec} given by (11.1) [104].

$$\tau_{rec} = \frac{R_b R_c}{R_b + R_c}(C_b + C_c) \tag{11.1}$$

τ_{rec} is relevant for the recurrence of discharges even under AC-voltages, if the frequency of the applied voltage is in the order of $1/\tau_{rec}$ or lower. The physical mechanisms that determine τ_{rec} is given by the conductivity of the bulk material and the conductivity of the void surface. A high surface conductivity of any void will cause a screening effect of the void at lower frequencies, i.e. a reduced field in the void and a reduced activity of PD. This screening effect at low frequencies will inevitable occur at low enough frequencies, in particular for a flat void elongated in the direction of the field ($C_c << C_b$), Figure 11.9 a). This effect is not observed here. Instead, if the flat cavity is perpendicular to the field ($C_c >> C_b$), Figure 11.9 b), then the field distribution as well as the recharging time is governed by R_b in series with C_c. This picture will cause an increasing field across the cavity with decreasing frequency, i.e. when $f << 1/\tau_{rec}$, and consequently more discharges per cycle. This latter tendency is what is observed here for 12 kV; hence, it is believed that the discharges origin from fairly flat voids.
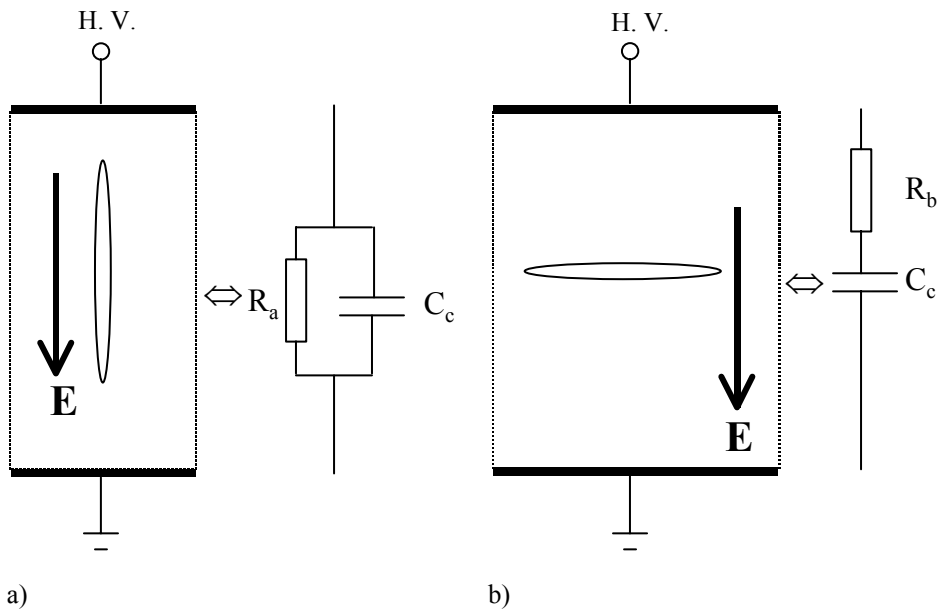
Figure 11.9 a) Flat cavity in parallel with the applied field and b) perpendicular to the applied field

11.3.2 Dielectric spectroscopy of Sample 1 at 25 °C

Dielectric spectroscopy was measured simultaneously as the VF-PRPDA. The apparent permittivities measured at different voltages are shown in Figure 11.10 and the contribution of PD to $\Delta\varepsilon'_{App}$ and ε''_{App} computed from the VF-PRPDA data is shown in Figure 11.11.

a)

b)

Figure 11.10 a) $\Delta\varepsilon'_{App}$ *and b)* ε''_{App} *vs. frequency for Sample 1 at 25 °C and different voltages.*
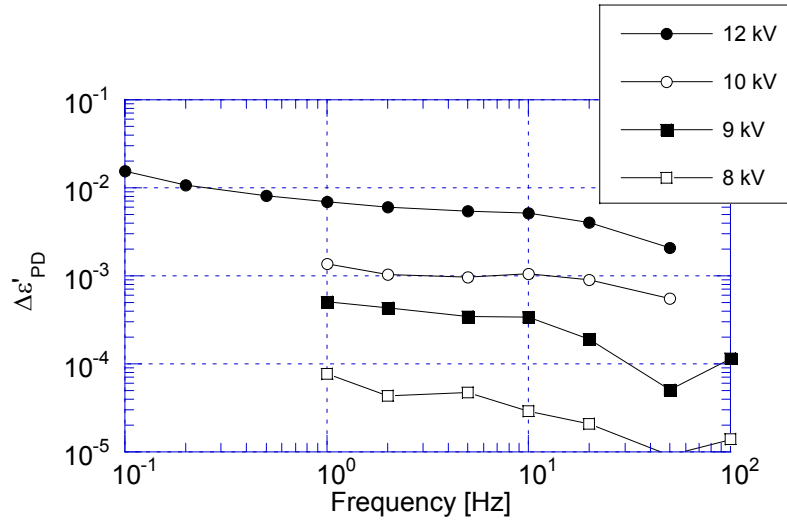
a)
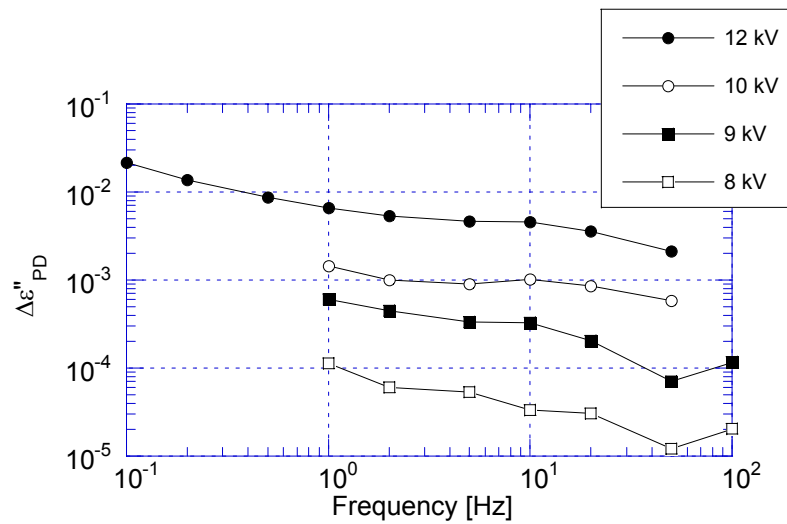
b)

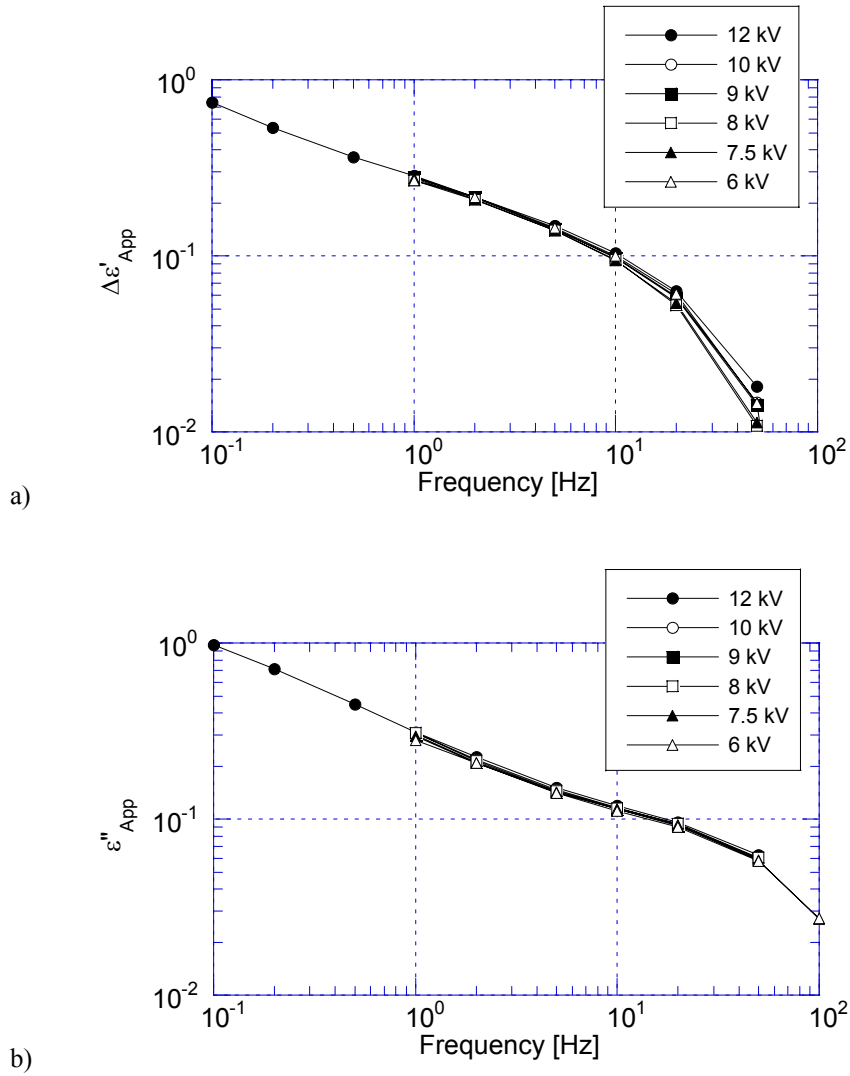*Figure 11.11 a)* $\Delta\varepsilon'_{PD}$ *and b)* $\Delta\varepsilon''_{PD}$ *calculated from the PRPDA patterns measured simultaneously as* $\Delta\varepsilon'_{App}$ *and* ε''_{App} *in Figure 11.10.*

The frequency dependence of PD activity, measured as $\Delta\varepsilon'_{PD}$ and $\Delta\varepsilon''_{PD}$, is similar to what is already shown in Q_{Tot}, Figure 11.5. The contribution of PD to $\Delta\varepsilon'_{App}$ and ε''_{App}, Figure 11.10 is not visible, due to the strong background loss and dispersion of the bulk material. The maximum voltage possible to apply for frequencies around 50 and 100 Hz with the simultaneous system was 12 kV, limited by the capacitive load in the filter, the test object and the coupling capacitor.

Dielectric spectroscopy measurements had been performed in advance with the IDA-system [27], for which $\Delta\varepsilon'_{App}$ and ε''_{App} are shown in Figure 11.12.

a)

b)
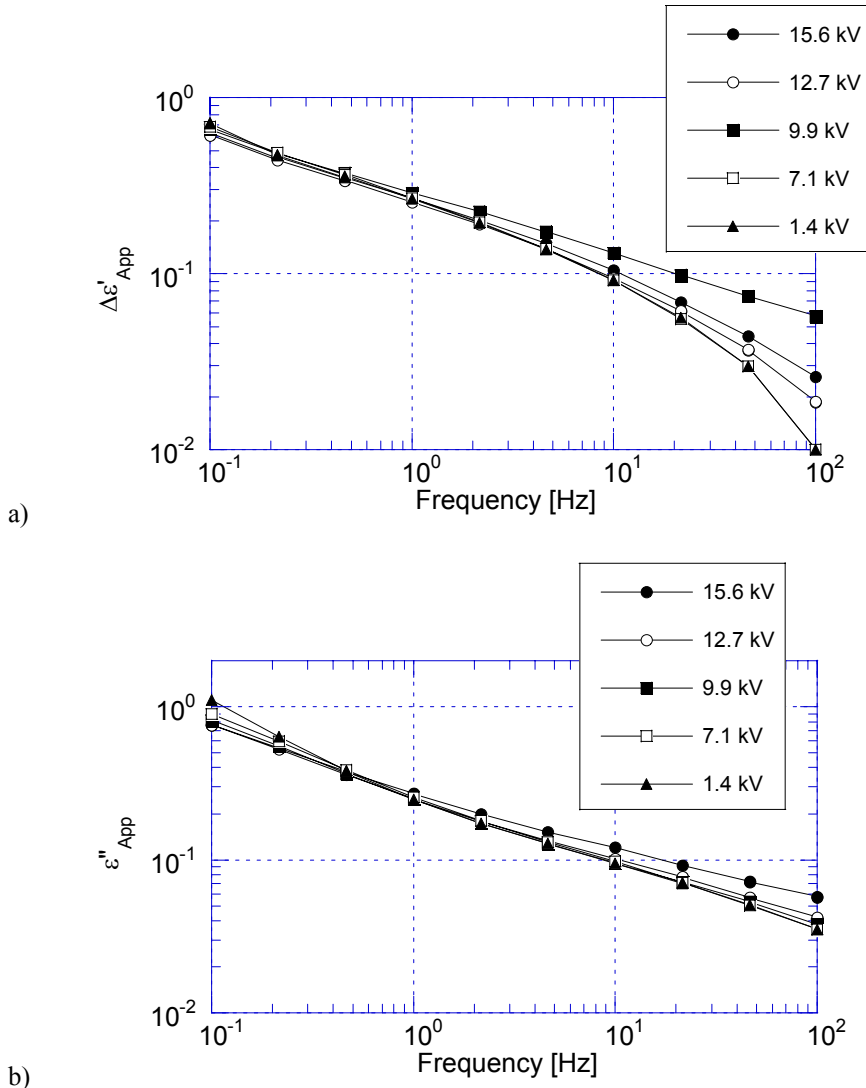
Figure 11.12 a) $\Delta\varepsilon'_{App}$ and b) ε''_{App} measured with the IDA system. The temperature was 19 °C.

Under the conditions measured with the IDA system, a voltage up to 15.6 kV was possible to apply even at 100 Hz, and several interesting features appear. At high frequencies one notice an increase in $\Delta\varepsilon'$ as well as ε'' with increasing voltage, this increase is certainly caused by PD. For frequencies below around 0.5 Hz a decrease in ε'' with increasing

voltage is noticed. This phenomenon is related to the Garton effect [106]. In short terms, the decrease in loss is caused by a depletion of mobile ions in the oil. This depletion occurs at high local fields, short gaps and low enough frequencies when the ions have ample time to become swept over to the paper where they will become stuck until the polarity of the field is reversed. The unability to move for the ions will simply cause the (conductive) loss in the oil to disappear, with the consequence that the total losses will decrease.

The PD-current is polarity independent, Figure 11.6. This polarity independence is consistent with a dominating odd harmonic content, HC_n in the dielectric response current measured with dielectric spectroscopy, see Figure 11.13.
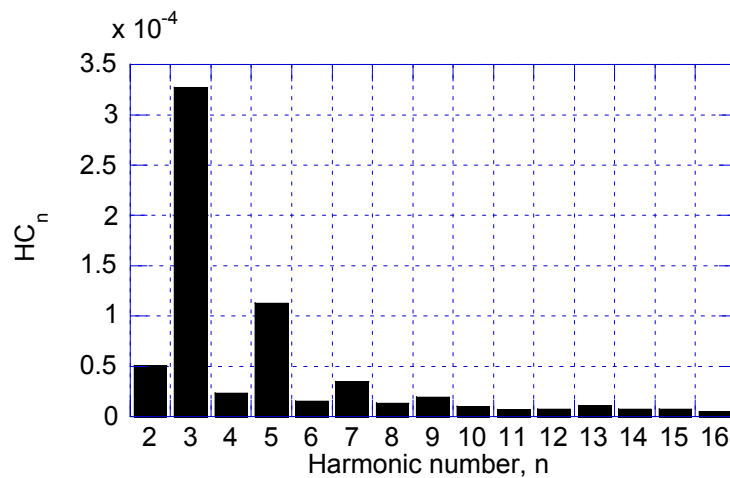
Figure 11.13 Harmonic content in the integrated PD current. Data obtained at 12 kV, 2 Hz and 25 °C.

11.3.3 Temperature dependence of Sample 1

Many parameters critical for the development, progress, voltage- and frequency-dependence of PD are affected by the temperature of the PILC. For example different thermal expansion of insulation and lead sheath, gas-pressure in voids, bulk-conductivity, surface conductivities, oil-viscosity, moisture distribution, etc. Therefore, an examination of the temperature dependence of the PD-activity in Sample 1 was performed.

Sample 1 was mounted for thermal cycling within a heat-tube, thermally insulated from outside, Figure 11.14. Water of a controlled temperature was circulated between the walls of the tube, which heated or cooled the cable to the desired temperature.

Figure 11.14 Sample 1 mounted for variation of temperature.

The tests were performed at 12 kV and for frequencies in the range 0.1 Hz - 50 Hz. A temperature cycle was performed, with the following temperatures: 25 - 40 - 60 - 50 - 40 - 30 - 25 - 20 °C. The time between different temperatures is at least 24 hours, but sometimes longer; thus, there is ample time to reach an equilibrium temperature at each temperature level.

The symmetry between positive and negative discharges remains at temperatures above 25 °C, and only discharges of a positive magnitude will be considered here.

The total amount of positive charge per cycle at 25, 40 and 60 °C, measured at increasing order, is shown in Figure 11.15. The effect of an increased temperature is a decreased PD-activity at higher frequencies, but an increasing activity at lower frequencies. This effect is not visible when the temperature is decreased in 10 °C steps from 60 °C to 20 °C, Figure 11.16, where the activity decrease monotonously with temperature over the whole frequency range. $\bar{q}(\varphi)$ is shown in Figure 11.17, indicating voids and the same discharge mechanism in this range of temperature.
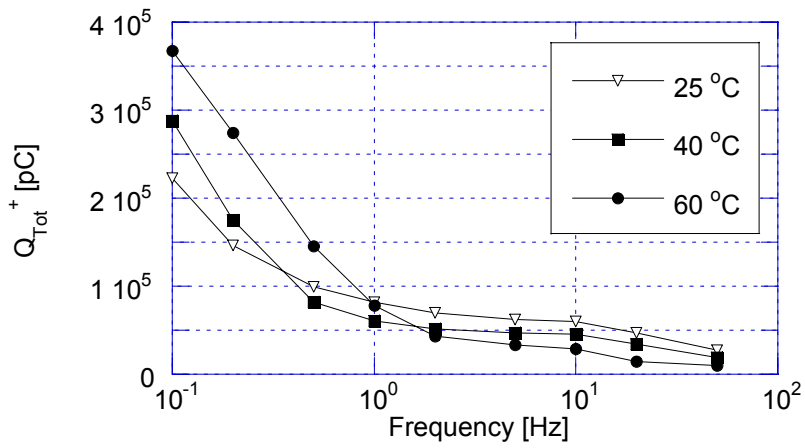
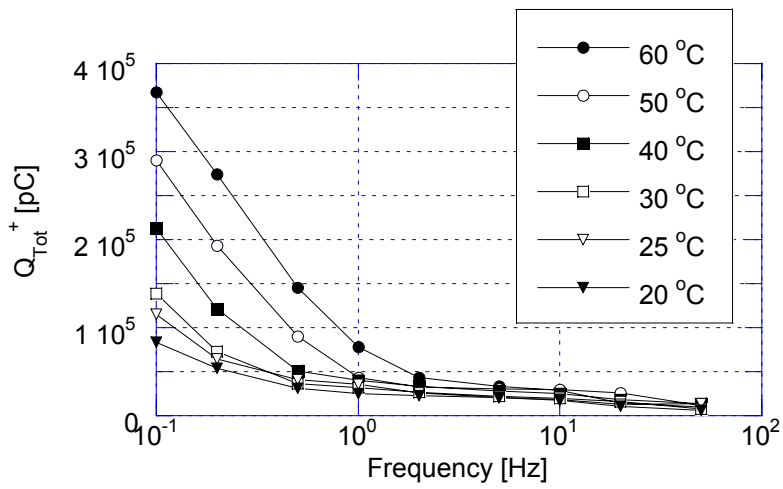Figure 11.15 Q_{Tot}^+ vs. frequency at 12 kV. Increasing temperature sequence.

Figure 11.16 Q_{Tot}^+ vs. frequency at 12 kV. Decreasing temperature sequence.
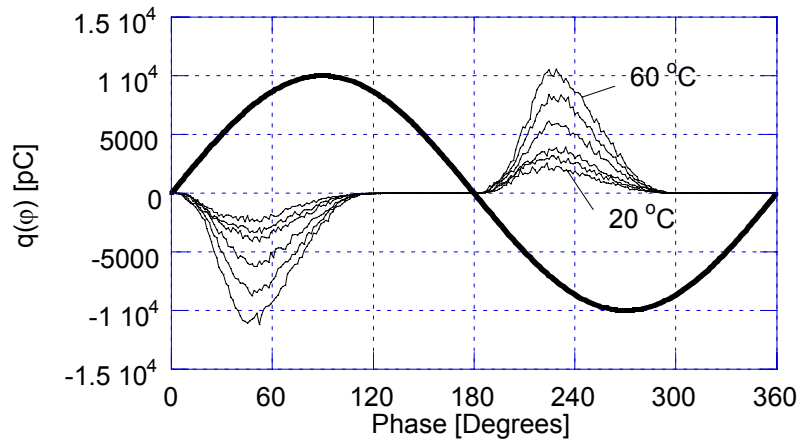
Figure 11.17 $\bar{q}(\varphi)$ for Sample 1 at 12 kV and the following temperatures 20, 25, 30, 40 ,50 and 60 °C, obtained under decreasing temperature.

The vulnerable phase of PD-activity in a mass-impregnated cable is the cooling phase [104], which in practice occur when the current decrease due to less loading. During cooling, the insulation shrinks faster than the lead, leaving cavities that will be filled with gas, but will also cause a redistribution of oil, and moisture if present.

At DC-voltage, there are two competing mechanisms with decreasing temperature that influence the PD-activity. First, the cooling enhance the formation of voids, which will lead to more PD. Next, the time-constant, τ_{rec} for recharging the cavity will increase, since the conductivity of the bulk will decrease with decreasing temperature [104], and consequently less PD per time unit.

The heating and cooling phase applied here is longer and slower compared to cycling-tests for DC-cables [105]. Anyway, during heating of Sample 1 it was observed that the activity decreased for frequencies in the range 1 - 50 Hz, but increased for frequencies below 1 Hz (0.1 - 1 Hz). This indicates that at higher frequencies the increased pressure in the cable will close some cavities, but this process can not compete with the stronger influence of the bulk conductivity at lower frequencies, which impose an increased PD-activity with increasing temperature. At decreasing temperatures, the monotonically decreasing PD-activity indicates that it is the increased time-constant τ_{rec} that controls the PD-activity, rather than an increased void-formation rate due to the insulation shrinkage. This invisible effect of the insulation shrinkage during cooling is explained by the fact that time between consecutive temperatures are long enough for the lead to shrink to the insulation.

11.4 Sample 2

11.4.1 Influence of termination

Sample 2 was not equipped by a commercial termination, instead a simpler termination was performed, by a field-grading tape wrapped around the terminations and then lowering the ends in transformer oil. The contribution from discharges in the termination area is shown in Figure 11.18. The PD-activity is high due to surface discharges if no termination at all is used, or if only the field-grading tape is applied. Immersing the ends in oil eliminates the surface discharges and the remaining discharge activity has its origin in discharges within the cable.
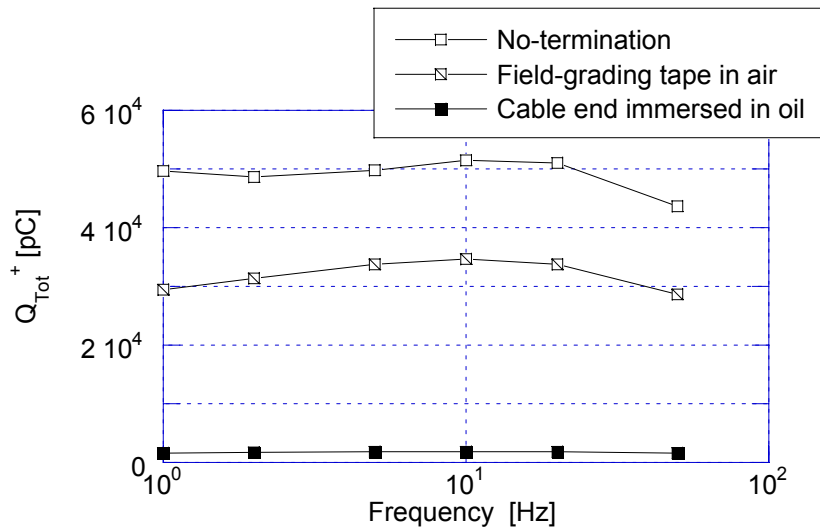
Figure 11.18 Q_{Tot}^+ obtained for Sample 2 at 12 kV with different ways to terminate the cable.

11.4.2 Voltage and frequency dependence

The total amount of apparent charge from Sample 2 is much less than for Sample 1, as can be seen by comparing Figure 11.19 and Figure 11.5. The phase distributions for Sample 2 is similar to Sample 1, but with the difference that the total charge is much less. The PD inception is somewhere between 8 and 10 kV, Figure 11.19. Q_{Tot}^+ for 10 and 11 kV seems to decrease at lower frequencies, whereas 12 kV are fairly frequency independent and eventually tends to increase at 0.1 Hz. A decrease with decreasing frequency is expected if the void surface conductivity is high enough [107]. However, this effect could not explain both the decay for 10 and 11 kV and at the same time explain the flat frequency dependence at 12 kV.
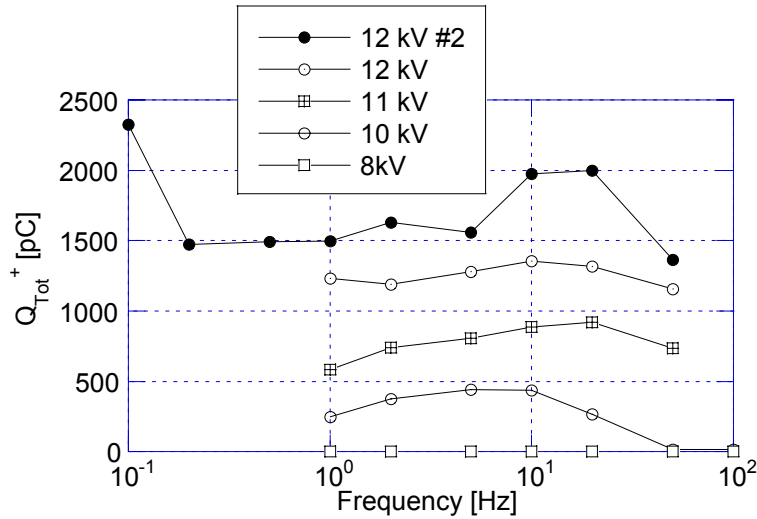
Figure 11.19 Q_{Tot}^+ for Sample 2 at 25 °C and different voltages. Cable ends immersed in oil.

A comparison of $\Delta\varepsilon'_{App}(f)$ and $\varepsilon''_{App}(f)$ with different voltages for Sample 2 without terminations are shown in Figure 11.20. The contribution from PD is small, or rather, the loss in the bulk material is high. $\Delta\varepsilon'_{App}(f)$ and $\varepsilon''_{App}(f)$ both increase with increasing magnitude at higher frequencies (10 - 100 Hz). This increase is related to the PD-current, which makes a contribution around $3 \cdot 10^{-3}$ to both $\Delta\varepsilon'_{App}(f)$ and $\varepsilon''_{App}(f)$, almost independent of frequency in the range 1 - 100 Hz. The almost frequency independent PD-contribution together with the strong dispersion in $\Delta\varepsilon'_{Bulk}(f)$ and $\varepsilon''_{Bulk}(f)$ makes the PD contribution relatively smaller, and harder to observe at lower frequencies. The decrease with voltage of $\Delta\varepsilon'_{App}(f)$ and $\varepsilon''_{App}(f)$ for the lowest frequencies is related to the previously mentioned Garton effect.
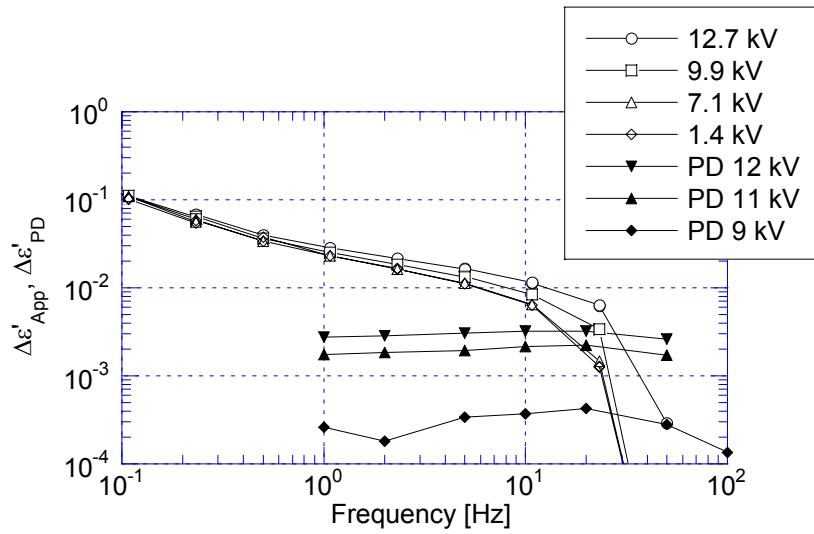
a)
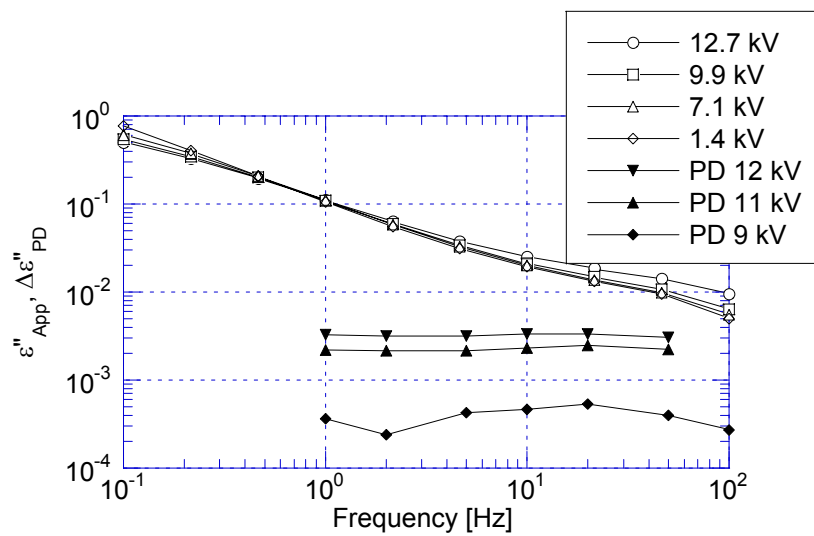
b)

Figure 11.20 Comparison between a) $\Delta\varepsilon'$ *and b)* ε'' *of Sample 2 for different voltages. Cable ends immersed in oil. Open symbols: measured with the IDA system. Filled symbols: computed from the PRPDA measurements.*

11.5 Conclusions

Two samples of an old paper insulated cable have been investigated, both with the VF-PRPDA technique and by simultaneous measurements with dielectric spectroscopy.

Sample 1 is taken from the cable end and has a higher dielectric loss than Sample 2, which is taken next to Sample 1. The higher loss in Sample 1 may be due to water that has penetrated from the cable end.

The partial discharge activity in Sample 1 is much higher than in Sample 2. In both samples the PD activity increases with voltage, an increase that is caused by an increasing number of discharges and not by higher individual discharge magnitudes.

The total amount of charge per cycle for Sample 1 increases with decreasing frequency, an observation related to a faster recharging of the void due to the high conductivity of the bulk material.

A temperature cycling has been performed on Sample 1. With decreasing temperature the total charge per cycle decrease monotonously and is particularly pronounced at low frequencies. This tendency supports the hypothesis that the recharging of the voids is controlled by the thermally activated bulk conductivity.

The partial discharge activity is hard to resolve with dielectric spectroscopy due to the high dielectric loss in the PILC, in particular at low frequencies. However, the influence of the partial discharges is visible as a tip-up in the permittivity and loss for frequencies above 20 Hz. The size of the tip-up is in the same order of magnitude as computed from the simultaneously acquired PRPDA data.

The dominating odd harmonic content of the dielectric response current is consistent with the polarity independent discharge mechanism.

12 Conclusions

This thesis has explored the frequency dependence of partial discharges in the applied voltage frequency range 1 mHz - 400 Hz. A measurement system has been developed that allows simultaneous measurements of VF-PRPDA and dielectric spectroscopy over the frequency range 1 mHz - 400 Hz of the applied voltage.

An algorithm has been developed that from the PRPDA pattern calculates the non-linear current contribution of partial discharges to the dielectric spectroscopy current. The algorithm has been experimentally verified on well-defined objects.

It has been demonstrated that phase- and polarity-symmetries of the partial discharge current can be investigated by a Fourier series expansion of the partial discharge current. The Fourier coefficients can be calculated either from the acquired PRPDA pattern or from the dielectric spectroscopy current. For example, the existence of only odd harmonics is a manifestation of a polarity independent discharge mechanism, like the situation for a void embedded in electrical insulation.

The frequency dependence of partial discharges has been investigated on well-defined objects like artificial voids and point-plane gaps, but has also been examined on practical insulation as machine insulation and oil paper insulated cable.

A cable-model with deliberately introduced cavities and an asphalt with mica insulated stator-bar infested by PD in delaminations have been investigated. For both objects it is demonstrated that the random supply of initial electrons may cause an increased probability for discharges with a decreasing applied voltage frequency. However, at frequencies below 1 Hz it is shown that the discharge activity decrease with decreasing frequency due to the increasing influence of the surface conductivity of the cavities and the delaminations.

It has been shown that the frequency dependence of surface discharges is dependent on the surface conductivity. The surface conductivity was altered by the adsorption of moisture from an ambient atmosphere with a controlled relative humidity. An increased surface conductivity grades the electrical field in such a way that it yields a higher inception voltage of surface streamers with an increased surface conductivity. The increased surface conductivity cause a reduction of the tangential field at decreasing frequency, which have been shown to yield a cessation of discharges at a low enough frequency.

PD in an oil paper insulated cable have been studied and it shows that the number of PDs increase with decreasing frequency and with increasing temperature. The increased number of discharges with increasing temperature is an effect of the faster recharging of the cavity, and is merely a consequence of the temperature dependence of the bulk-conductivity.

13 Future work

This thesis has considered the development of the VF-PRPDA technique and the combination with dielectric spectroscopy. The future work required in order to achieve a method that is applicable and reliable for condition assessment of the quality of practical insulation systems is outlined below.

The measurement system for simultaneous measurements of VF-PRPDA and dielectric spectroscopy can be improved and adapted to a flexible instrument that can work under field conditions as well as for studies of basic phenomena in laboratory environment.

Theoretical models needs to be developed that relates the frequency dependence of PD to the physical mechanisms behind.

The ageing of insulation with known defects ought to be studied. In that case it is believed that the progressive deterioration by PD yields an increased surface conductivity, which is a measure of ageing. The increased surface conductivity would then alter the frequency dependence of the partial discharge activity, which could be used as a diagnostic tool.

The VF-PRPDA technique should be applied on real insulation systems that commonly are infested by PD, e.g. machine insulation and oil paper insulated cables.

Dielectric spectroscopy with harmonic analysis has to be continued on practical insulating systems to investigate the influence of other non-linear sources than PD, e.g. terminations and field-grading enamels, but also on other defects that have a non-linear response like water-tree infested XLPE cables.

The possibility to use the Fourier-series expansion of the PD-current, as a tool to recognise the source of the PD needs to be further investigated.

Bibliography

[1] E. Kuffel, W. S. Zaengl and J. Kuffel, *High Voltage Engineering: Fundamentals*, 2nd. ed. Newnes, Butterworth-Heinemann, 2000.

[2] B. Holmgren, *Dielectric response, breakdown strength and water-tree content of medium voltage XLPE cables*, Licentiate thesis, KTH 1997, TRITA-EEA-9705, ISSN 1100-1593.

[3] P. Thärning, *Watertree Dielectric Spectroscopy*, Licentiate thesis, KTH 1997, TRITA-EEA-9703, ISSN 1100-1593.

[4] P. Werelius and U. Gäfvert, "High voltage dielectric response analyser for cable diagnostics in field condition.", 9th Int. Symp. On High Voltage Engineering, Graz, Austria, 1995, Paper 5662, pp. 1 - 4.

[5] A. K. Jonscher, *Universal Relaxation Law*, Chelsea Dielectrics Press, London, 1996.

[6] U. Gäfvert, "Condition Assessment of Insulation Systems: Analysis of Dielectric Response Methods", Nordic Insulation Symposium (Nord-IS), Bergen, Norway, 1996, pp. 1 - 20.

[7] R. Neimanis, *On Estimation of Moisture Content in Mass Impregnated Distribution Cables*, PhD thesis, KTH 2001, TRITA-EEK-0101, ISSN 1100-1593.

[8] H. Edin, *Comparison between Time Domain and Frequency Domain Methods for Dielectric Measurements on Oil Impregnated Cellulose*, Diploma Work, KTH and ABB Corporate Research 1995. Report number: SECRC/KH/TR-95/178E.

[9] L. G. Virsberg and A. Kelen, "Some Observations on the Very-Low-Frequency Testing of High-Voltage Machine Insulation", Proceedings of the 20th Int. Conf. on Large Electric Systems (Cigré), June 1964, Vol. 2, Paper 108, pp. 1-19.

[10] E. Ildstad, "Status and Trends in Diagnostics of Polymeric High Voltage Cables", Stockholm Power Tech, International Symposium on Electric Power Engineering, June 1995, SPT IS 05-5, pp. 124 - 129.

[11] P. Morshuis, "Assessment of Dielectric Degradation by Ultrawide-band PD Detection", IEEE Trans. on Diel. and El. Insul., Vol. 2 No. 5, Oct. 1995, pp. 744 - 760.

[12] C. Hudon, R. Bartnikas and M. R. Wertheimer, "Spark-to-glow Discharge Transition due to Increased Surface Conductivity on Epoxy Resin Specimens", IEEE Trans. on El. Insul., Vol. 28 No. 1, Feb. 1993, pp. 1 - 8.

[13] Power Diagnostix Systems GmbH, Bruesseler Ring 95a, 52074 Aachen, Germany. http://www.pd-systems.com

[14] A. Kelen, "Critical Examination of the Dissipation Factor Tip-Up as a Measure of Partial Discharge Intensity", IEEE Trans. on El. Insul., Vol. 13 No. 1, Feb. 1978, pp. 14 - 24.

[15] B. V. Bhimani, "Very-Low-Frequency High-Potential Testing", AIEE Trans. Pt. III, Vol. 80, June 1961, pp. 148 - 155 and 163 - 166.

[16] K. Haga and M. Yoneyama, "Breakdown Strength and Dielectric Characteristics of Oil-Impregnated Paper Cable Insulation at Very Low Frequencies", Electrical Engineering in Japan, Vol. 88, No. 6, 1968, pp. 39 - 48.

[17] D. A. Hilder, V. N. Gray and I. A. Black, "The Application of Ramp and Low Frequency A.C. Voltages to Discharge Detection", IEE Conf. Publ. 94, March 1973, pp. 14 - 19.

[18] R. Miller and I. A. Black, "Partial Discharge Measurements Over The Frequency Range 0.1 Hz To 50 Hz", IEEE Trans. El. Insul., Vol. 12 No. 3, June 1977, pp. 224 - 233.

[19] R. Miller and I. A. Black, "Partial Discharge Energy Measurements on Electrical Machine Insulation when Energized at Frequencies Between 0.1 Hz and Power Frequency", IEEE Trans. El. Insul., Vol. 14 No. 3, June 1979, pp. 127 - 135.

[20] K. G. Burnley, D. H. Ellison and J. L. T. Exon, "A system for the measurement of the loss tangent and capacitance of high-voltage insulation over a wide range of frequency and voltage", J. Phys. E: Sci. Instrum., Vol. 16, 1983, pp. 1039 - 45.

[21] K. G. Burnley and J. L. T. Exon, "Diagnostic Measurement based on Bridge Out-of-balance Signals", IEEE Trans. on El. Insul., Vol. 28 No. 2, April 1991, pp. 200 - 209.

[22] K. Haga, Y. Fujiwara, Y. Ebinuma, N. Sasaki, M. Ogishima and M. Aihara, "Development of 22 kV Very Low-Frequency, High-Voltage Generator and the Characteristics of Partial Discharge in XLPE Cables", Proc. of the 21th Symposium on Electrical Insulating Materials, IEEJ, 1988, pp. 175 - 178.

[23] H. Emanuel, M. Kuschel, C. Steineke, D. Pepper, R. Plath and W. Kalkner, "A New High Voltage Dielectric Test System for Insulation Diagnosis and Partial Discharge Measurement", Nordic Insulation Symposium (Nord-IS), Bergen, Norway, 1996, pp. 283 - 290.

[24] D. Pepper and W. Kalkner, "PD-measurements on typical defects on XLPE-insulated cables at variable frequencies", 10th Int. Symp. on High Voltage Engineering, Montreal, Canada, 1997, Vol. 4, pp. 389 - 392.

[25] P. Werelius, P. Thärning, R. Eriksson, B. Holmgren and U. Gäfvert, "Dielectric Spectroscopy for Diagnosis of Water Tree Deterioration in XLPE Cables", IEEE Trans. on Diel. and El. Insul., Vol. 8 No. 1, Feb. 2001, pp. 27 - 42.

[26] U. Gäfvert and B. Nettelblad, "Measurement techniques for dielectric response characterisation at low frequencies", Nordic Insulation Symposium (Nord-IS), Lyngby, Denmark, Paper No. 7.1, 1990.

[27] IDA system, Programma Electric AB, Eldarv. 4, SE-187 75 Täby, Sweden. http://www.programma.se

[28] T. W. Dakin, "The Relation of Capacitance Increase with High Voltage to Internal Electric Discharges and Discharging Void Volume", AIEE Trans. Pt. IIIA, Vol. 78, Oct. 1959, pp. 790 - 95.

[29] R. Bartnikas, "Pulsed Corona Loss Measurements in Artificial Voids and Cables", Int. Conf. on Large Electric Systems (Cigré), 21st meeting, 1966, Vol. 2, Report 202, pp. 1 - 37.

[30] R. Bartnikas, "Discharge Rate and Energy Loss in Helium at Low Frequencies", Archiv für Elektrotechnik, Vol. 52 No. 6, 1969, pp. 348 - 359.

[31] K. G. Burnley and J. L. T. Exon, "Relationship between various measurement techniques for void discharges", Proceedings of the IEE., Vol. 129, Pt. A, No. 8, Nov. 1982, pp. 593 - 606.

[32] M. Lundmark, D. Ribbing and U. Gäfvert, "Studies of loss tangent and harmonic content with low frequency HV dielectric response measurements in order to evaluate degradation in machine insulation", ABB Corporate Research Report TR KJD 93-018, 1993 (Unpublished).

[33] R. Goffeaux, M. Krecke, B. Comte, M. Cottet and B. Fruth, "Dielectric Test Methods for Rotating Machine Stator Insulation Inspection", Conf. on El. Insul. and Diel. Phen. (CEIDP), Atlanta, USA, 1998, pp. 528 - 533.

[34] T. Hücker and H.-G. Kranz, "Requirements of Automated PD Diagnosis Systems for Fault Identification in Noisy Conditions", IEEE Trans. on Diel. and El. Insul., Vol. 2 No. 4, Aug. 1995, pp. 544 - 556.

[35] F. H. Kreuger, *Partial Discharge Detection in High-Voltage Equipment*, Butterworths, 1989.

157

[36] R. Bartnikas and E. J. McMahon (eds.), *Engineering Dielectrics Volume 1: Corona Measurement and Interpretation*, ASTM STP 669, 1979.

[37] E. Nasser, *Fundamentals of Gaseous Ionization and Plasma Electronics*, John Wiley & Sons, 1971.

[38] K. Wu, Y. Suzuoki, T. Mizutani and H. Xie, "Model for partial discharges associated with treeing breakdown: I. PDs in tree channels", J. Phys. D: Appl. Phys., Vol. 33, 2000, pp. 1197 - 1201.

[39] F. H. Kreuger, E. Gulski and A. Krivda, "Classification of Partial Discharges", IEEE Trans. on El. Insul., Vol. 28 No. 6, Dec. 1993, pp. 917 - 931.

[40] H. Edin, S. Jayaram and U. Gäfvert, "Influence of Relative Humidity on Surface Discharges Over the Frequency Range 0.1 Hz to 100 Hz", Submitted to IEEE Transaction on Dielectrics and Electrical Insulation.

[41] L. Niemeyer, "A Generalized Approach to Partial Discharge Modeling", IEEE Trans. on Diel. and El. Insul., Vol. 2 No. 4, Aug. 1995, pp. 510 - 528.

[42] H. Edin, "The Influence of Dielectric Polarisation on the Measured PD Charge in a Two-Layer Dielectric System", Nordic Insulation Symposium (Nord-IS), Lyngby, Denmark, 1999, pp. 433 - 441.

[43] M. Hoof and R. Patsch, "Pulse-Sequence Analysis: a new method for investigating the physics of PD-induced ageing", IEE Proc.-Sci. Meas. Technol., Vol. 142, No. 1, Jan. 1995, pp. 95 - 101.

[44] G. C. Crichton, P. W. Karlsson and A. Pedersen, "Partial Discharges in Ellipsoidal and Spheroidal Voids", IEEE Trans. on El. Insul., Vol. 24 No. 2, April 1989, pp. 335 - 342.

[45] I. W. McAllister, "Decay of Charge Deposited on the Wall of a Gaseous Void", IEEE Trans. on El. Insul., Vol. 27 No. 6, Dec. 1992, pp. 1202 - 1207.

[46] A. K. Jonscher, *Dielectric Relaxation in Solids*, Chelsea Dielectrics Press, London, 1983.

[47] R. Bartnikas and R. M. Eichhorn (eds.), *Engineering Dielectrics Vol. II A. Electrical Properties of Solid Insulating Materials: Molecular Structure and Electrical Behaviour*, ASTM Special Technical Publication 783, 1983.

[48] P. Hedvig, *Dielectric Spectroscopy of Polymers*, John Wiley & Sons, New York, 1977.

[49] U. Gäfvert, G. Frimpong and J. Fuhr, "Modelling of Dielectric Measurements on Power Transformers", Int. Conf. on Large HV Electric Systems (Cigré), 1998, Report 15-103, pp. 1 - 8.

[50] L. Råde and B. Westergren, *Beta Mathematics Handbook*, 2nd. ed., Studentlitteratur, Lund, 1990.

[51] A. Bulinski, S. Bamji, E. So, G. C. Montanari, A. Motori and S. Gubanski, "Diagnostic Measurements of High Voltage Polymeric Cable Insulation", International Symposium on Electrical Insulating Materials, Tokyo, Japan, 1995, pp. 19 - 26.

[52] H. Edin and U. Gäfvert, "Simultaneous Measurement of Phase Resolved Partial Discharges and Dielectric Spectroscopy", Submitted to IEEE Transaction on Dielectrics and Electrical Insulation.

[53] J. T. Holbøll and H. Edin, "PD-Detection vs. Loss Measurements at High Voltages with Variable Frequencies", 10th International Symposium on High-Voltage Engineering (ISH), Montreal, Canada, 1997, pp. 4.421 - 4.425.

[54] J. T. Holbøll, U. Gäfvert and H. Edin, "Time-Domain PD-detection vs. Dielectric Spectroscopy", Conference on Electrical Insulation and Dielectric Phenomena (CEIDP), Minneapolis, USA, 1997, pp. 498 - 503.

[55] H. Edin and U. Gäfvert, "Harmonic Content in the Partial Discharge Current Measured with Dielectric Spectroscopy", Conference on Electrical Insulation and Dielectric Phenomena (CEIDP), Atlanta, USA, 1998, pp. 394 - 98.

[56] L. B. Loeb, *Electrical Coronas: Their Basic Physical Mechanisms*, University of California Press, 1965.

[57] E. Gulski, *Computed-Aided Recognition of Partial Discharges using Statistical Tools*, Delft University Press, 1991.

[58] J. Giddens, Statistical Analysis of Partial Discharges for the Frequency Range 1 mHz to 100 Hz, Diploma thesis, KTH, 1999.

[59] J. Giddens, H. Edin and U. Gäfvert, "Statistical Analysis of Partial Discharges for The Frequency Range 1 mHz to 400 Hz", Nordic Insulation Symposium (Nord- IS), Lyngby, Denmark, 1999, pp. 141 - 148.

[60] J. Giddens, H. Edin and U. Gäfvert, "Measuring System for Phase-Resolved Partial Discharge Detection at Low Frequencies", 11th International Symposium on High-Voltage Engineering (ISH), London, United Kingdom, 1999, pp. 5.228 - 5.231.

[61] T. Okamoto and T. Tanaka, "Novel Partial Discharge Measurement, Computer-Aided Measurement Systems", IEEE Trans. on El. Insul., Vol. 21 No. 6, Dec. 1986, pp. 1015 - 1019.

[62] H. Cramér, *Mathematical Methods of Statistics*, Almqvist & Wiksells, Uppsala, Sweden, 1945.

[63] J. A. Shohat and J. D. Tamarkin, *The Problems of Moments*, American Mathematical Society, 1943.

[64] P. Thärning, P. Werelius, B. Holmgren and U. Gäfvert, "High Voltage Dielectric Response Analyser for Cable Diagnostics", Conf. on El. Insul. and Diel. Phen. (CEIDP), Pocono Manor, USA, 1993, pp. 745 - 750.

[65] A. Helgeson, *Dielectric Properties of Machine Insulation studied with Dielectric Response*, Licentiate Thesis, KTH 1997, TRITA-EEA-9704, ISSN 1100-1593.

[66] Trek Inc., "Operator's Manual, Trek model 20/20 A, High-Voltage Amplifier", 11601 Maple Ridge Road, Medina NY 14103, USA. http://www.trekinc.com.

[67] Cigré Working Group 21.03, "Recognition of Discharges", CIGRÉ, Electra, No. 11 Dec. 1969, pp. 61-98.

[68] K. Matikainen, "Some Observations Upon Distributions of Partial Discharge Pulses Measured with a Multi-Channel Analyser", 22nd. Int. Conf. On Large Electric Systems At High Tension (CIGRÉ), 1968, Paper 21-06, pp. 1 - 9.

[69] R. Bartnikas, "Use of multichannel analyzers for corona pulse height distribution measurements in cables and other electrical apparatus", IEEE Trans. on Instrumentation and Measurement, Vol. 22 No. 4, Dec. 1973, pp. 403 - 407.

[70] M. Hikita, K. Yamada, A. Nakamura, T. Mizutani, A. Oohasi and M. Ieda, "Measurements of Partial Discharges by Computer and Analysis of Partial Discharge Distribution by the Monte Carlo Method", IEEE Trans. on El. Insul., Vol. 25 No. 3, June 1990, pp. 453 - 468.

[71] E. Gulski and F. H. Kreuger, "Computer-aided recognition of Discharge Sources", IEEE Trans. on El. Insul., Vol. 27 No. 1, Feb. 1992, pp. 82 - 92.

[72] B. Fruth, L. Niemeyer, M. Hässig, J. Fuhr and Th. Dunz, "Phase Resolved Partial Discharge Measurements and Computer Aided Partial Discharge Analysis Performed on Different High Voltage Apparatus.", 6th Int. Symp. on High Voltage Engineering, New Orleans, LA, USA, 1989, Paper 15.03.

[73] T. Tanaka, "Internal Partial Discharge and Material Degradation", IEEE Trans. on El. Insul., Vol. 21 No. 6, Dec. 1986, pp. 899 - 905.

[74] M. G. Danikas, "Small Partial Discharges and their Role in Insulation Deterioration", IEEE Trans. on Diel. and El. Insul., Vol. 4 No. 6, Dec. 1997, pp. 863 - 867.

[75] R. Patsch and F. Berton, "Pulse-Sequence-Analysis - Chances to Characterize Defects", Conf. on El. Insul. and Diel. Phen. (CEIDP), Austin, USA, 1999, pp. 243 - 248.

[76] Borland Software Corporation, 100 Enterprise Way, Scotts Valley, CA 95066-3249, USA. http://www.borland.com

[77] IEC Standard 60270, "High-voltage test techniques: Partial-discharge measurements", 3rd ed., International Electrotechnical Commission (IEC), Geneva, Switzerland, 1999.

[78] Keithley Instruments, Inc., *Model 617 Programmable Electrometer - Instruction Manual*, 1988, 28775 Aurora Road, Cleveland, Ohio 44139, USA. http://www.keithley.com.

[79] MATLAB, The MathWorks, Inc., 3 Apple Hill Drive, Natick, MA 01760-2098, USA, http://www.mathworks.com.

[80] MATLAB, "Building GUIs with MATLAB Version 5", The MathWorks, Inc., 3 Apple Hill Drive, Natick, MA 01760-2098, USA, http://www.mathworks.com.

[81] J. Sköldin, *Simultan mätning av fasupplöst PD och dielektrisk spektroskopi på pappers-olja kabel vid olika temperatur och med variabel frekvens på matande spänning*, Diploma thesis, 23030/2 EEK, KTH 2000.

[82] Alpha Wire, http://www.alphawire.com

[83] B. Fruth and L. Niemeyer, "The Importance of Statistical Characteristics of Partial Discharge Data", IEEE Trans. on El. Insul., Vol. 27 No. 1, Feb. 1992, pp. 60 - 69.

[84] G. C. Stone, "Partial Discharge Measurements To Assess Rotating Machine Insulation Condition: A Survey", Proc. of the IEEE Int. Symp. on El. Insul., Montreal, Quebec, Canada, June 1996, pp. 19 - 23.

[85] W. McDermid, "Insulation Systems and Monitoring for Stator Windings of Large Rotating Machines", IEEE El. Insul. Mag., Vol. 9, No. 4, 1993, pp. 7 - 15.

[86] G. C. Stone, "Aging and Testing of Stator Winding Insulations Systems", Seminar held in Copenhagen, Denmark, June 20, 1990.

[87] R. Miller, "The Influence of Frequency on Permittivity and Partial Discharge Measurements on Electrical Machine Insulation", Proc. of the 6th BEAMA Int. El. Insul. Conf., Brighton, United Kingdom, 1990, pp. 238 - 242.

[88] Y. Awakuni, J. H. Calderwood, "Water vapour adsorption and surface conductivity in solids", J. Phys. D.: Appl. Phys., Vol. 5, 1972, pp. 1038 - 1045.

[89] IEC International Standard 343, "Recommended test methods for determining the relative resistance of insulating materials to breakdown by surface discharges", 1991.

[90] D. T. Clark and W. J. Feast (eds.), *Polymer Surfaces*, John Wiley & Sons, 1978.

[91] H. T. M. Haenen, "The Characteristic Decay with Time of Surface Charges on Dielectrics", Journal of Electrostatics, Vol. 1 1975, pp. 173 - 185.

[92] A. Crisci, B. Gosse, J-P. Gosse and V. Ollier-Duréault, "Surface-potential decay due to surface conduction", Eur. Phys. J., Applied Physics, Vol. 4, 1998, pp. 107 - 116.

[93] A. K. Jonscher and T. Ramdeen, "Transient Dielectric Response of Conduction On Humid Mica", IEEE Trans. on El. Insul., Vol. 22 No. 1, Feb. 1987, pp. 35 - 39.

[94] P. A. Heimann and J. E. Olsen, "A sensitive method for measuring surface conductivity of insulators", J. Appl. Phys., Vol. 53(1), Jan. 1982, pp. 546 - 549.

[95] J. Hu, X.-D. Xiao, D. F. Ogletree, M. Salmeron, "Imaging the Condensation and Evaporation of Molecular Thin Films of Water with Nanonmeter Resolution", Science, Vol. 268, Apr. 14 1995, pp. 267 - 269.

[96] L. Centurioni, G. Coletti, F. Guastavino and E. Torello, "About the Degradation of Polymer Films Due to Surface Partial Discharges at Different Humidity Levels", IEEE Int. Symp. on Electrical Insulation, Arlington, Virginia, USA, June 1998, pp. 190 - 193.

[97] R. Bozzo, C. Gemme, F. Guastavino and P. Tiemblo, "Lifetime Dependence on Relative Humidity of Polymers Subjected to PD Aging", Conf. on El. Insul. and Diel. Phenomena, San Francisco, Oct. 1996, pp. 838 - 841.

[98] S. Yasufuku and M. Todoki, "Dielectric and Thermoanalytical Behaviour of Moisture and Water in Aromatic Polyamide and Polyimide Films", IEEE Int. Symp. on El. Insul., Pittsburg, PA, USA, June, 1994, pp. 197 - 200.

[99] F. Garbassi, M. Morra and E. Occhiello, *Polymer Surfaces - From Physics to Technology*, John Wiley & Sons, 1994.

[100] Y. Zhu, T. Takada, Y. Inoue and D. Tu, "Dynamic Observation of Needle-plane Surface Discharge using the Electro-optical Pockels Effect, IEEE Trans. on Diel. and El. Insul., Vol. 3 No. 3, June, 1996, pp. 460 - 468.

[101] R. Ross, "Pressure Effects and Moisture Penetration in Mass-Impregnated Cable", 5th Int. Conf. on Prop. and Appl. of Diel. Materials, May 1997, pp. 439 - 442.

[102] L. Olsson and G. Bengtsson, "PD-Mapping of Paper-Insulated MV Cables in Gothenburg", Cired 97, paper 3.12, IEE Conf. Publ. No. 438, 1997.

[103] R. R. MacKinlay, "Partial Discharge Location in High Voltage Cables", Published by EA Technology. See also http:// www.eatl.co.uk.

[104] M. J. P. Jeroense and F. H. Kreuger, "Partial Discharge Measurements on a High Voltage Direct Current Mass Impregnated Paper Cable", IEEE Int. Symp. on El. Insul., Montreal, 1996, pp. 134 - 137.

[105] M. J. P. Jeroense, M. Bergkvist and P. Nordberg, "Partial Discharges in High Voltage Direct Current Mass-Impregnated Cables", 11th Int. Symp. on High Voltage Engineering, London, 1999, Paper 5.53 - 5.57.

[106] C. G. Garton, "Dielectric Loss in Thin Films of Insulating Liquids", Journal of IEE (London), Vol. 88 Pt. 3, 1941, pp. 23 - 40.

[107] M. K. Domun, R. R. MacKinlay and R. Miller, "The Effects of Voltage and Frequency on the Partial Discharge Characteristics of HV Paper Cables", 6th Int. Symp. on High Voltage Engineering, New Orleans, 1989, Paper 27.36, pp. 1 - 4.